Simultaneous Estimation of State of Charge and State of Health of a Large Format Li-ion Cell based on an Equivalent Circuit Model

by

Saurabh Gairola

A thesis submitted to the Graduate Faculty of
Auburn University
in partial fulfillment of the
requirements for the Degree of
Master of Science

Auburn, Alabama
Aug 3, 2019

Keywords: Equivalent circuit model, Adaptive filter, Decoupled estimator, Power fade, Capacity fade, State of Charge

Approved by

Song-Yul Choe, Chair, Professor in Dept. of Mechanical Engineering
Scott Martin, Assistant Research Professor in Dept. of Mechanical Engineering
John Y. Hung, Chair, Professor & Graduate Program Officer in Dept. of Electrical and Computer Engineering

Abstract

Accurate estimations of the state of charge (SOC), capacity fade (SOH_Q) and power fade (SOH_P) are critical for ensuring safe and reliable operations of Lithium-ion batteries. Traditional estimation methods using complex models and look-up tables do not satisfy either the required accuracy or computational time necessary for real time applications. In this paper, we propose a method that simultaneously estimates both SOC and SOH over different temperature ranges under aging conditions. The battery is modeled with a second order equivalent circuit (ECM) and then its states and parameters are estimated by implementing a combination of a Variable model framework (VM) based Adaptive Extended Kalman Filter along with a forgetting factor based Recursive Least Square (RLS) filter algorithm in a closed-loop framework.

The VM-AEKF is employed to efficiently estimate the fast varying SOC and model parameters where the VM framework is designed specifically to improve the stability and accuracy of the estimator under conditions when the system is not sufficiently excited by the input signal. Simultaneously, the RLS estimates the slowly varying maximum capacity and updates the value based on a delayed approach. The parameters estimated by the proposed estimator are then used to calculate the SOH_P and SOH_Q.

The proposed algorithms are validated with a large format NMC/Carbon pouch type power cell with a nominal capacity of 58.4 Ah at multiple charge-discharge cycles considering aging and temperature effects. The experimental results have shown less than 5% SOC estimation error and less than 3% capacity estimation error for the typical SOC range of 10% to 90%.

Acknowledgments

I would like to take this opportunity to express my deep gratitude to my advisor, Dr. Song-Yul Choe, for this research opportunity. His valuable suggestions and constant help steered me towards the fulfillment of my study. Without his detailed corrections to my papers and thesis, I would hardly finish my research program. I would also like to thank Dr. John Y. Hung and Dr. Scott martin for serving on my committee and providing me with valuable comments and suggestions.

Sincere thanks to my colleagues Yalan Bi and Yilin Yin for their help and guidance throughout my thesis. Additional thanks to Yalan Bi for discussion in estimation algorithms and Yang Hu who helped gather the experimental data for this research.

Last but not the least, my heartfelt thanks to all my friends and family members who supported and encouraged me in my academic endeavor.

Table of Contents

List of Tables

List of Figures

Nomenclature

Q_{max}	Maximum charge capacity at full charge, [Ah]
$Q_{releasable}$	Dischargeable charge capacity, [Ah]
$Q_{nominal}$	Maximum charge capacity at full charge and nominal conditions, [Ah]
$P_{available}$	Maximum available power at full charge and any instant state, [W]
$P_{nominal}$	Maximum available power at full charge and nominal conditions, [W]
I	Current of the battery, [A]
V_t	Terminal voltage, [V]
R_{EOL}	Resistance of the cell at the End-of-Life, [Ω]
R_{BOL}	Resistance of the cell at the Beginning-of-Life, [Ω]
R_{bat}	Resistance of the cell at any given instance, [Ω]
R_{int}, R_0	Ohmic resistance, [Ω]
R_1	Equivalent resistance of the first R-C circuit of ECM, [Ω]
R_2	Equivalent resistance of the second R-C circuit of ECM, [Ω]
C_1	Equivalent capacitor of the first R-C circuit of ECM, [F]
C_2	Equivalent capacitor of the second R-C circuit of ECM, [F]
V_{C_1}	Voltage drop across the first R-C circuit of ECM, [V]
V_{C_2}	Voltage drop across the second R-C circuit of ECM, [V]
OCV	Ideal voltage or Open circuit voltage, [V]
η	Cell overpotential, [V]
τ_1, τ_2	Time constants of the ECM, [sec]

T_s	Sample time, [sec]
η	Coulombic efficiency
x	State vector
y	Measurement vector
A	State matrix
B	Input matrix
H	Measurement matrix
w	Process noise
v	Measurement noise
Q	State noise covariance
R	Measurement noise covariance
$\hat{x}_k^+$	Posteriori estimate of the state at step k
$\hat{x}_k^-$	Priori estimate of the state at step k
P_k^+	Posteriori error covariance at step k
P_k^-	Priori Error covariance at step k
K_k	Kalman gain at step k
$\hat{C}_v$	Sample variance estimate for adaptive noise update
m	Size of the moving window for adaptive noise update
$\mathcal{S}$	Variable to monitor change in input current
$\mathcal{G}$	Window size for the varying model framework
θ	State vector for RLS

φ_{RLS}	State matrix for RLS
y_{RLS}	Measurement vector for RLS
λ	Forgetting factor

1. Introduction

1.1 Background

The recent shift towards battery technology in the sectors of transport, buildings and power grid, has pushed for development of more sophisticated and accurate battery management systems (BMSs). A major cause for this recent shift can be attributed to the improvements in the performance of Lithium-ion batteries. These improved Lithium-ion batteries, with high energy and power densities, are viable for electric vehicles (EVs) and as energy storage systems (ESSs) for smart grids.

BMSs are a vital component of battery packs, with two major roles: (1) To ensure the safe operating area of the battery, defined by manufacturing and architecture related specifications, such as the overcharge and under discharge, maximum depth of discharge, upper and lower cut off voltage of the individual cells, and (2) To continuously measure battery parameters, to determine or predict its status, health, and performance figures generally referred to as battery monitoring. This is accomplished by continuously monitoring the current, voltage and temperature of the battery while accurately estimating essential battery states like the State of Charge (SOC), State of Health (SOH).

1.1.1 NMC Lithium-ion cell

Lithium-ion cells using a combination of nickel-manganese-cobalt (NMC) as the cathode chemistry and carbon graphite as the anode chemistry are currently one of the most successful Li-ion batteries [1]. These cells are designed to work as either energy or power cells. In addition, , adding nickel to the cathode provides a higher energy density, lower cost, and longer cycle life than only the cobalt-based cells, which leads to NMC base Li-ion systems as the preferred choice

for energy storage systems (ESSs) and automotive systems like electric vehicles (EVs), hybrid electric vehicles (HEVs) and plug-in hybrid electric vehicles (PHEVs).

A typical Li-ion cell consists of three primary components; a positive electrode made of a lithium metal oxide, $LiMO_2$, where M is a metal alloy of Ni, Mn, and Co in case of NMC; a negative electrode made of carbon and graphite is preferred for most commercial purposes; an electrolyte made of a lithium salt in an organic solvent. The metal oxide determines the cell performances [1], [2], where Cobalt is the main active material but has a relatively short life span, low thermal stability and limited load capabilities like specific power. Nickel provides high specific energy but has poor stability, while Manganese has the benefit of forming a spinel structure to achieve low internal resistance but offers low specific energy. The metals are combined such that to enhance each other's strengths.

The negative and the positive electrodes are the reactants in the electrochemical reactions while the electrolyte provides a conductive medium for lithium ions to move freely between the electrodes. Lithium ions are free to move in and out of both the electrodes through the process of insertion (intercalation) or extraction (deintercalation) respectively. The schematic of a common Li-ion cell along with the direction of the flow of electrons and the positively charged lithium ions (Li^+) during discharging and charging is depicted in Figure 1.

During discharging, the Li-ions de-intercalate from the negative electrode and are transported, and intercalate into the positive electrode [3]. The process is reversed when charged. The half-reaction at the negative electrode:

$$Li_xC_6 \rightleftharpoons C_6 + xLi^+ + xe^- \qquad (1)$$

The half-reaction at the positive electrode is:

$$Li_{(1-x)}MO_2 + xLi^+ + xe^- \rightleftharpoons LiMO_2 \qquad (2)$$

Combining Eq. (1) and (2), the full cell reaction is described as:

$$Li_xC_6 + Li_{(1-x)}MO_2 \rightleftharpoons C_6 + LiMO_2 \qquad (3)$$

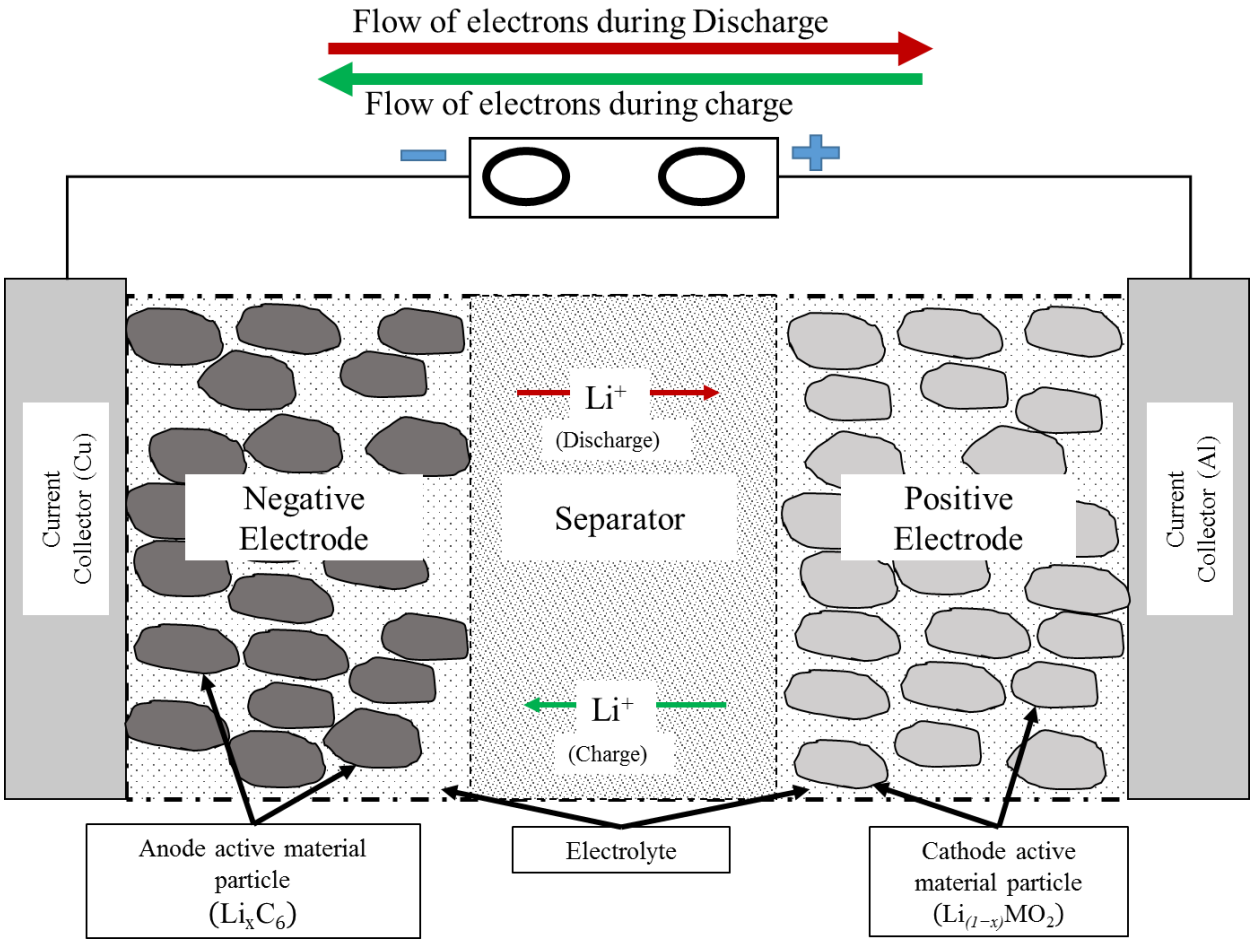

Figure 1 Schematic of a Li-ion cell

1.1.2 Definition of states

Various metrics have been defined to continuously monitor and evaluate the performance of a cell [4]–[7]. These metrics are identified as the states of the cell. The most common cell states are:

1. *State of charge (SOC):* SOC is defined as the percentage ratio between the amounts of releasable charge relative to the maximum charge stored at most recent fully charged state. It is given as:

$$SOC(\%) = \frac{Q_{\text{releasable}}}{Q_{\max}} \times 100 \qquad (4)$$

, where Q_{max} is the maximum capacity in a fully charged state at any given operating condition and $Q_{releasable}$ is the maximum capacity that can be extracted from the cell at any given instant.

SOC is a key indicator of the instant status, equivalent of a fuel gauge, for battery systems. A simple method to find the SOC in real-time is using the Coulomb (Ah) counting method:

$$SOC_t(\%) = \int_0^t \frac{Id\tau}{Q_{\max}} \times 100 \qquad (5)$$

2. *State of health (SOH):* Description of the instantaneous state by SOC is not sufficient alone to represent the degradation of the cell due to the irreversible processes referred to as aging. A new metric, SOH, is defined as a measure of this long-term wear and tear. A common measure of SOH, based on the impedance increase, have been described in [8], [9] and defined in [5] as:

$$SOH(\%) = \frac{R_{\text{EOL}} - R_{\text{bat}}}{R_{\text{EOL}} - R_{\text{BOL}}} \times 100 \qquad (6)$$

, where $R_{EOL,}$ $R_{bat,}$ and R_{BOL} is the resistance at the End-of-Life (EOL), at the instance of observation and, at the Beginning-of-Life (BOL), respectively. This definition has been interchangeably used to describe both the power fade (SOH_P) and the general SOH of the cell. SOH can be divided into *Capacity Fade (SOH_Q)* and *Power Fade (SOH_P)*, respectively.

   i. SOH_Q indicates the percentage decrease in capacity over the cycle life:

$$SOH_Q(\%) = \frac{Q_{\max}}{Q_{\text{nominal}}} \times 100 \qquad (7)$$

ii. SOH_P indicates the percentage decrease in power capability over the cycle life:

$$SOH_P(\%) = \frac{P_{\text{available}}}{P_{\text{nominal}}} \times 100 \qquad (8)$$

1.1.3 Literature Review

SOC is an important indicator of the instantaneous state of the battery and a wide variety of methods is proposed in the literature for its estimation [3]–[5], [7], [10]–[18]. The Coulomb counting method, is the most commonly implemented method due to its simplicity and low computational time. However, its accuracy is affected by errors accumulated during current integration, initial values and operating conditions [7]. Open Circuit Voltage (OCV) methods, based on the relationship between the OCV and SOC, have also been extensively used [19]. These methods are not suitable for real time applications as batteries require a long resting period before the OCV can be measured accurately. Data-driven methods based on Neural Network (NN), Support vector machine (SVM) and Fuzzy-Logic [14], [15], [20] have high estimation accuracy but require extended training times and large amounts of reliable data. Model-based methods using Bayesian filters are prominently used for real time applications due to their high robustness and estimation accuracy. Least Squares (LS) methods, like moving window LS filter [21], estimate SOC using an equivalent circuit model. Other variations of LS methods include UD (U represent the upper triangle matrix and D is the Diagonal matrix) factorization-based Recursive LS (RLS) [22], combined RLS and Kalman Filter (KF) [23] and Instrumental Variable RLS (IV-RLS) [24]. Extended KF (EKF) can estimate the battery SOC based on ECM with less than 5% error for different driving cycles [17]. Advanced KFs like Adaptive EKF (AEKF) [10], Sigma point KF (SPKF) [25], Ln normalized Unscented KF (Ln-UKF) [26] and Dual EKF (D-EKF) [16] have

also been proposed. These methods are suitable for real-time applications and provide low estimation errors but have certain drawbacks. Their accuracy decreases due to accumulation of numerical errors over extended operational periods while they also fail to meet 'Identifiability', due to a large number of states being estimated, which is explained in detail in chapter 3.

Several methods for estimation of the SOH¸ summarized in Figure 2, have been discussed in the literature [11], [27], [28] and can be categorized into two ways: (1) Experimental methods, or (2) Model-based methods.

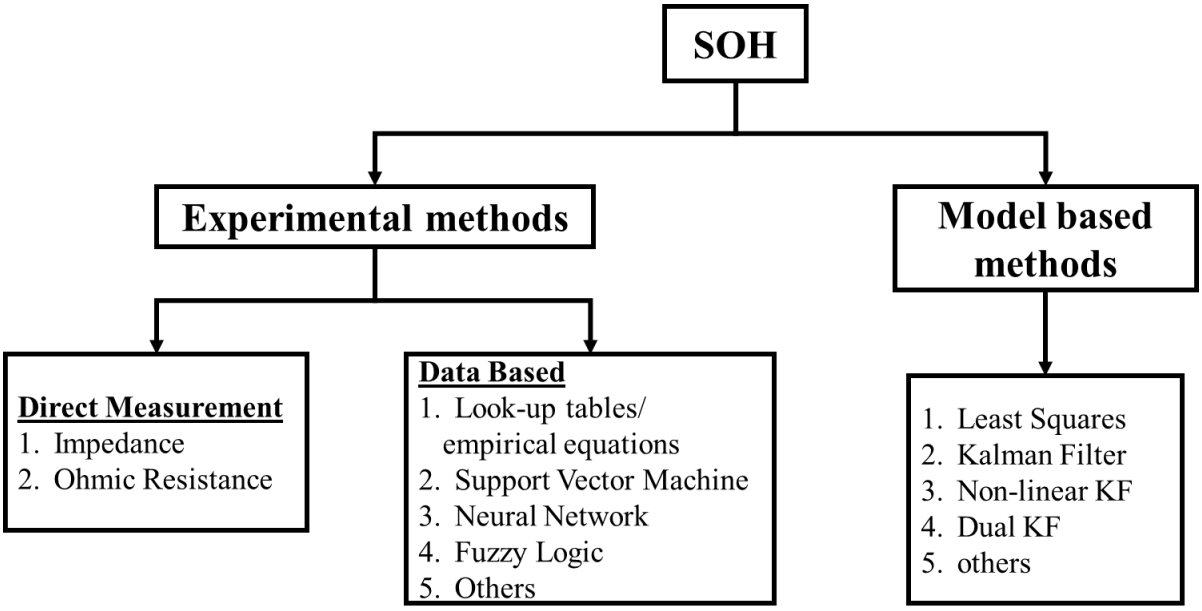

Figure 2. Summary of SOH estimation methods

Experimental methods use testing data and previous knowledge of cell performance to predict their states. These methods are specific to a cell and cannot be used for other cells. Impedance measurement is one of the most popular experimental methods, where impedances over a wide range of AC frequencies at different charge and discharge currents are measured using Electrochemical Impedance Spectroscopy (EIS) [12], [29]. Another method [6] measures the Ohmic resistance of a cell using Hybrid Pulse Power Characterization (HPPC) test according to guidelines provided by Department of Energy (DOE), which is used to measure available power

and has been extensively used to measure SOH [8], [9], [30]. However, these methods, though usually used for offline identification, can be implemented for online estimation using data obtained to build empirical functions, probabilistic relation or look-up tables (LUTs) [13], [31].

Recent developments have shifted the focus of research towards implementing machine learning based methods [14], [20], [32]–[34] that include SVM [34], Fuzzy logic algorithms [14] and NN [32]. These methods are easy to implement and can provide accurate results but are not suitable for online estimation due to high computational effort and large sets of training data required before being implemented. Furthermore, they are non-adaptive and highly sensitive to changes of cell parameters.

On the other hand, model-based methods estimate parameters based on models that are sensitive to the states of the cell, which can be applied for batteries with different chemistries with minimum tuning efforts. The estimated parameters are either directly related to SOH or include the dependent variables [6], [9]. These parameters have been estimated by employing various state observers [10], [21], [22], [25], [35]–[40], with KF being the most implemented. Linear KF (LKF) has been used for parameter and state estimation [23] but since most models are nonlinear, the EKF [35], [36], [38] and UKF [25] are preferred. Non-linear Dual KF (D-KF) has also been proposed [15], [16], [41], where one filter estimates the parameters and the other estimates SOH. Despite showing favorable results, these methods are highly complex, requiring matrix differentiation of the large error covariance matrix shared between the two estimators. The order of EKF can be different, like a second order EKF used for fast varying SOC and voltage, while a fourth order for slowing varying SOH if the voltage error exceeds a threshold [37]. A Lyapunov based adaptive observer can also be used to estimate SOH based on a simple first-order ECM [5], however it's long-term performance needs to be verified as it is dependent on offline identified

parameters. Model-based approaches are widely preferred over experimental methods due to accuracy and relatively reduced experimental time.

1.2 Experimental Setup

The testing is performed in an in-house designed testing station consisting of a thermal chamber, a power supply for charging and an electronic load for discharging that is controlled by a host computer to control and store data. The test station facilitates charging and discharging a battery with any desired current profile and ambient temperature, including the EIS measurement of the Li-ion battery. All the experiments are conducted on large format NMC/C power cells, which specifications are as summarized in Table 1.

Table 1. Specifications of the NMC cell

Item	Specification
Chemistry	Active Material: $Li[Ni_{0.6}Mn_{0.2}Co_{0.2}]O_2$
Cell dimensions	Size: 99.7 mm × 301.5 mm × 13.17 mm, Weight: 835 gm
Nominal Capacity	58.9 Ah @discharge C/3
Nominal Voltage	3.633 V
Cutoff Voltage	2.5 V, 4.2 V
Energy Density	528 Wh/L

Block diagram for the test station is depicted in Figure 3. The capability and specifications of the test station are shown in Table 2. National Instruments LabVIEW software is used to control the test station. Testing profiles can be constant current (C.C.), constant voltage (C.V.), or the combined charging and discharging.

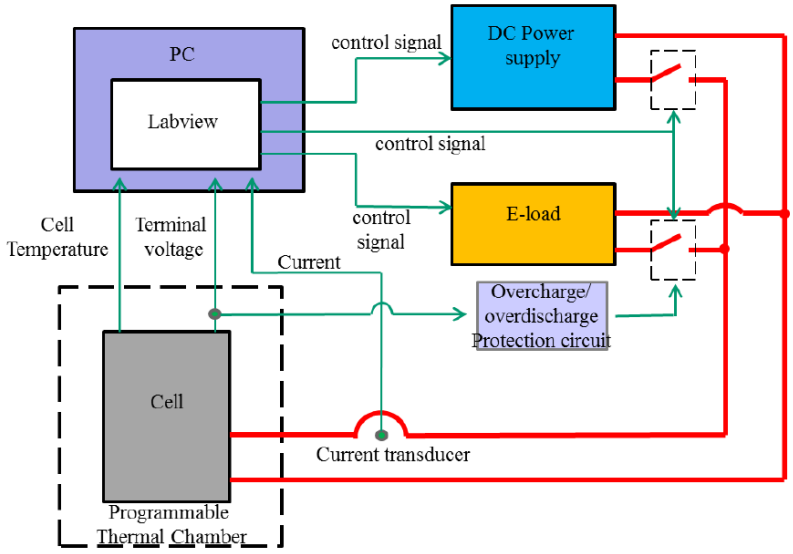

Figure 3. Test station block diagram

Table 2. Performance of the test station

Term		**Values**
Max. charge current		50A
Max. discharge current		125A
A range of the ambient temperature		-20~60 ºC
Data acquisition channels	Channel	16 Analog input channels 24 Digital input/output channels Analog output channels
	Frequency	625 kS/s
	Resolution	1 mA (current) 0.01mV (voltage)
Frequency range of EIS		1mHz~1kHz

1.3 Motivations and objectives

Battery states and parameters cannot be measured directly while the system is in operation and thus need to be estimated. To continuously estimate these states for accurate BMS operation, advanced algorithms have been researched extensively. Majority of this research focuses on estimating individual states like SOC or SOH instead of providing a comprehensive approach to estimate them simultaneously, which is necessary. Implementing separate algorithms for each state

require high computational effort which is undesirable for a BMS. Furthermore, battery states are inter-dependent and should be estimated simultaneously to improve the accuracy of BMS.

Further review of current literature has shown that a majority of the methods that estimate the states simultaneously, focus on estimating SOH_Q along with SOC [4], [27], [37], [42], while SOH_p is overlooked. BMSs used in HEVs require a precise real-time estimate of the power available. The peak power estimate provides the necessary information required to optimally balance the relationship between power performance of the battery pack and the HEV, to meet the acceleration and gradient climbing power requirements and to maximize regenerative braking [30]. In addition, to avoid over-charging or over-discharging and extend its lifespan [43]. Degradation of this power availability or peak power is described by the SOH_P which is why it is necessary to estimate it along with the other states.

Monitoring of batteries is a challenging task, because their states are dependent on internal parameters that have a nonlinear relation to a variety of external operating conditions like temperature and load profiles. In addition, these parameters change significantly as the cell ages, which makes it rather difficult to predict its behavior. Thus, advanced battery algorithms are needed for BMS that are capable of estimating these parameters throughout the cell life along with considering external operating conditions.

There are certain limitations that must be considered while developing algorithms for BMS. Firstly, these algorithms are commonly implemented using microcontrollers, which has limited computational power and thus a simple model, such as equivalent circuit model (ECM) is preferred. Secondly, there is limited memory space in a microcontroller and as such, recursive methods are preferred because they do not need to store a large amount of information as it gets updated with each sample time. Lastly, the estimation results should have high accuracy and

reliability. Thus, advanced estimation techniques should be applied to achieve the required performance.

Based on the above analysis, an approach that enables simultaneous estimation of SOC and SOH, including SOH_P and SOH_Q, of lithium-ion cells is proposed. This thesis focuses on three major topics as listed below:

- Analysis of cell behavior with respect to aging and temperature
- Long-term SOC and parameter estimation under different temperature and aging conditions
- SOH_P and SOH_Q calculation

1.4 Thesis outline

The basic structure of the thesis is shown as follows:

1. Introduction

This chapter discusses the research background, experimental setup and the motivations and objectives of this thesis. The research background briefly introduces the basics of NMC/C lithium ion cell along with a definition of cell states and a thorough literature review of SOC and SOH estimation methods.

2. Modeling

First, the different types of cell models are introduced in this chapter. After reviewing the various modeling methods, ECM is selected for this research. The different types of ECM are then described and their performances are compared. Based on this, the second order ECM is chosen and then its parameters are identified using an offline identification method. An analysis of these parameters, with respect to temperature and aging, is provided along with the testing schedules employed.

3. SOC and SOH estimation

This chapter is the main focus of the thesis and describes methods for online SOC and SOH estimation. First, an overview of the various online parameter estimation approaches along with the proposed approach is provided. Then the performance of a traditional EKF for SOC and ECM parameter estimation is analyzed and an improved estimator algorithm is proposed. Thereafter, an approach for Q_{max} estimation is described along with a simple, low computation framework to implement the two algorithms together. The combined estimator is then validated at different temperature and aging conditions using various test profiles. Finally, the cell parameters are used to estimate SOH and the results are validated using offline data.

4. Conclusion and future work

Concluding remarks and future works are provided in this chapter.

2. Modeling

2.1 Overview

Battery modeling is an important task within BMS development. Various modeling techniques have been suggested in the literature [7], [44]–[46] and can be categorized into three groups:

1. Electrochemical model,
2. Empirical models, and
3. Semi-empirical model.

Electrochemical models are *physics-based models* that describe the electrochemical processes occurring inside the cell governed by physical laws that include electrochemical kinetics, mass, charge, and energy balance along with potential theory, which forms a set of coupled nonlinear partial differential equations (PDEs). The models can provide an explanation of key behaviors of battery at the microscopic scale. In addition, all the internal states are fully observable and unique, allowing 'virtual measurements' of quantities that could not otherwise be measured, which allows for analysis and research purposes [3], [17], [47], [48]. However, a large number of parameters, sometimes as high as 50, is needed along with a high configuration effort to establish these models, which increases complexity and requirements for needed memory size and computation time and are unsuitable for practical real-time applications.

Empirical models are *data-driven models* that are based on empirical parameters that do not include any physical significance. The approaches are easy to configure, and able to deliver quick responses and predictions. However, their accuracy is dependent on the complexity of the model. Recently, more advanced models based on fuzzy logic and/or neural networks have been developed and can estimate states with high accuracy but require extensive testing data for training them [12], [15], [20], [29], [31], [33], [49].

Conversely, semi-empirical models provide a relatively effective way to characterize battery dynamics with low complexity and high accuracy. These models use simple equations by utilizing an understanding of the cell behavior, where the parameters are loosely based on the physical processes of the cell that can be easily obtained using adaptive data-driven techniques. The low complexity and high adaptability of such models make them the perfect choice for most practical applications. Equivalent circuit models (ECMs) are the most popular one that allows for a simple electrical circuit to replace the complex electrochemical process. ECMs are constructed by putting resistors, capacitors and voltage sources in a circuit [5], [10], [13], [15], [16], [21], [36]–[38] and a comparative study of different ECMs is shown in [44]. The correlation with battery dynamics is preserved by adding capacitors into the circuit. A summary of the different models is provided in Table 3.

Table 3. Summary of battery models

Method	Description	Summary	References
Electrochemical model	Use complex equations to describe cell internal ion transport and reactions	☑ High accuracy. ☑ Quick convergence. ☒ Extensive testing data required for training. ☒ High storage requirement. ☒ High computational cost.	[3], [17], [47], [48]
Empirical models	Use data-based empirical relation to describe cell behavior	☑ High accuracy. ☑ Update based on the dependent variable. ☒ Slow convergence. ☒ Extensive testing data required for training. ☒ Low stability.	[12], [15], [20], [29], [31], [33], [49]
Equivalent circuit models (ECM)	Use simplified circuit diagrams to represent cell dynamics	☑ No stored data required. ☑ No extensive test data required for training. ☒ Slow convergence. ☒ Low stability. ☒ Difficult to distinguish the effects of the different estimated states. ☒ Extensive reference work not available.	[5], [10], [13], [15], [16], [21], [36]–[38]

2.2 Equivalent circuit model

The cell terminal voltage, V_t under load is described by the open circuit voltage OCV , the voltage drop caused by internal Ohmic resistance, R_{int}, and the overpotentials caused by various electrochemical phenomenon like diffusion η_{diff}, charge transfer polarization $\eta_{ch,tr}$, concentration polarization η_{conc} , etc. [13], [19], [50]:

$$V_t = OCV - IR_{\text{int}} - \eta_{\text{diff}} - \eta_{\text{ch,tr}} - \eta_{\text{conc}} - \cdots \qquad (9)$$

, where I is the cell current and is defined as positive for discharging and negative for charging. The internal Ohmic resistance encompasses the resistivity of the components in a battery that include current collectors, the active material of the anode and cathode, and the electrolyte [50].

Typically, ECMs consist of an ideal voltage source, a series resistors and one or several resistor-capacitor groups connected in series with the resistance where the ideal voltage source represents the OCV of the battery. The ECM can be categorized into four groups dependent on the order of the circuit.

1. *Zero Order ECM:* Also called the R_{int} model, shown in Figure 4, consists of an ideal voltage source (*OCV)* and an internal resistor R_0, which are a function of SOC, SOH and temperature. The model is described by Eq. (10), and the terminal voltage is:

$$V_t = OCV - IR_0 \qquad (10)$$

As the model does not represent transient behavior, it is not suitable for accurate estimation of battery states during any dynamic operation (non-constant load).

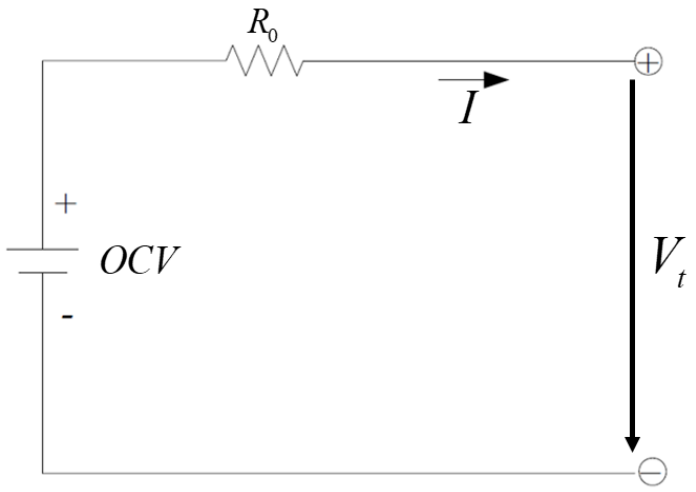

Figure 4. Zero Order ECM

2. *First Order ECM:* Also called the *Thevenin Model*, consists of a parallel RC circuit added in series to the R_{int} model. As shown in Figure 5, the model is composed of a voltage source, internal resistors and capacitors. The internal resistors include the ohmic resistor R_0 and polarization resistor R_1. The capacitor, C_1 ,is used to describe the transient response during charging and discharging. V_{C_1} is the voltage drop across the *RC* pair. The electrical behavior of the model can be expressed as follows;

$$\frac{dV_{C_1}}{dt} = -\frac{V_{C_1}}{R_1 C_1} + \frac{I}{C_1} \qquad (11)$$

$$V_t = OCV - V_{C_1} - IR_0 \qquad (12)$$

Eq. (11)-(12) can be expressed in discrete form with a small sampling time $T_s (< 1\ sec)$ as:

$$V_{C_1,k+1} = \mathrm{V}_{C_1,k} \mathrm{e}^{-\frac{T_s}{R_1 C_1}} + \mathrm{I}_k \mathrm{R}_1 \left(1 - \mathrm{e}^{-\frac{T_s}{R_1 C_1}}\right) \qquad (13)$$

$$V_{t,k+1} = OCV_{k+1} - V_{C_1,k+1} - I_{k+1} R_0 \qquad (14)$$

The terms R_1 and C_1 are arbitrary coefficients that can have any combination of values as long as the term $^1/_{R_1C_1}$ is satisfied with the system. To ensure a system with unique parameters, the term R_1C_1 is replaced by the time constant τ_1, which is related to the eigenvalue of the system. The equations can then be updated to:

$$V_{C_1,k+1} = V_{C_1,k}e^{-\frac{T_s}{\tau_1}} + I_k R_1\left(1 - e^{-\frac{T_s}{\tau_1}}\right) \qquad (15)$$

$$V_{t,k+1} = OCV_{k+1} - V_{C_1,k+1} - I_{k+1}R_0 \qquad (16)$$

, where T_s denotes the sampling time.

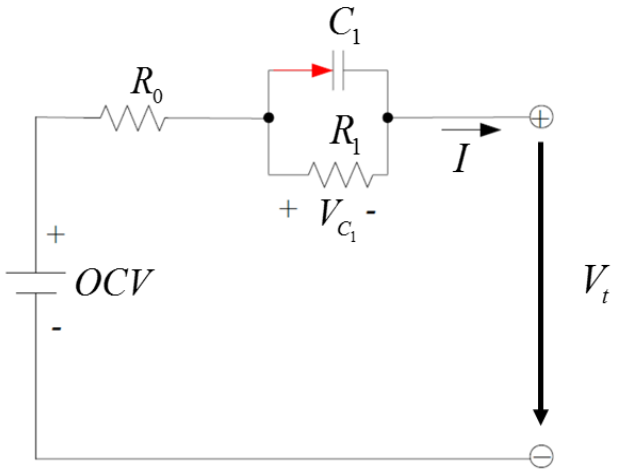

Figure 5. First Order ECM

3. *Second Order ECM:* The First-Order model can simulate voltage behavior to a certain extent. However, the various slow and fast acting processes lead to an inaccurate representation for extended charge or discharge periods. To improve the performance of the model an extra RC network is added in series, which becomes a second order model, also called the *Dual Polarization Model*.

It is composed of three parts, as shown in Figure 6; (1) OCV, (2) internal resistors such as the ohmic resistor R_0 and the polarization resistors that include R_1 and R_2, and (3) the capacitors with C_1 and C_2, which are used to mimic the dynamic response during charging and discharging. V_{C_1} and V_{C_2} are the overpotentials across R_1C_1 and R_2C_2 respectively. The electrical behavior of the circuit can be expressed as:

$$\frac{dV_{C_1}}{dt} = -\frac{V_{C_1}}{R_1C_1} + \frac{I}{C_1} \qquad (17)$$

$$\frac{dV_{C_2}}{dt} = -\frac{V_{C_2}}{R_2C_2} + \frac{I}{C_2} \qquad (18)$$

$$V_t = OCV - V_{C_1} - V_{C_2} - IR_0 \qquad (19)$$

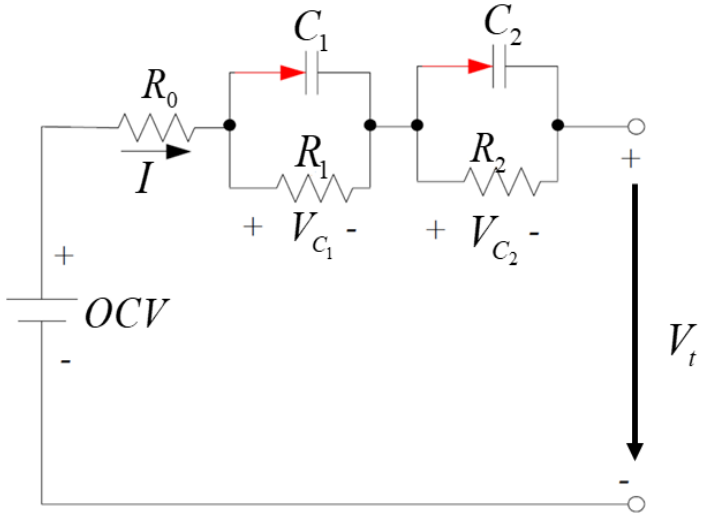

Figure 6. Second Order ECM

Substituting again with time constants, the description in discrete time domain is given by:

$$V_{C_1,k+1} = V_{C_1,k} e^{-\frac{T_s}{\tau_1}} + I_k R_1 \left(1 - e^{-\frac{T_s}{\tau_1}} \right) \quad (20)$$

$$V_{C_2,k+1} = V_{C_2,k} e^{-\frac{T_s}{\tau_2}} + I_k R_2 \left(1 - e^{-\frac{T_s}{\tau_2}} \right) \quad (21)$$

$$V_{t,k+1} = OCV_{k+1} - V_{C_1,k+1} - V_{C_2,k+1} - I_{k+1} R_0 \quad (22)$$

4. *Higher Order Models:* Models consisting of three or more *R-C* circuits can be used to increase accurate dynamic responses but increase complexity and computational time. Similar to first and second order ECMs, the output equation is described as:

$$V_{t,k+1} = OCV_{k+1} - I_{k+1} R_0 - V_{C_1,k+1} - V_{C_2,k+1} \cdots - \mathrm{V}_{C_n,k+1} \quad (23)$$

, where, the overpotential V_{C_n} is defined as:

$$V_{C_n,k+1} = V_{C_n,k} e^{-\frac{T_s}{\tau_n}} + I_k R_n \left(1 - e^{-\frac{T_s}{\tau_n}} \right) \quad (24)$$

Higher order models are rarely used for online application due to the high number of parameters and states. In addition, OCV is a function of SOC, $OCV = f\left(SOC\right)$, where SOC in discrete form is defined as:

$$SOC_{k+1} = SOC_k - \frac{1}{3600 Q_{\max}} I_k T_s \quad (25)$$

, where η is the coulombic efficiency (CE). CE is defined as the ration of discharge capacity and charge capacity of the cell in a cycle and reaches almost 1 or 100% for most commercial lithium-ion batteries [51]

The first and second order model provide the best balance between accuracy and complexity for most practical applications [24], [44]. Thus, the performance of both models is compared in order to select one for application of SOH_P prediction.

2.3 Measurement and analysis of cell parameters

Parameters of a cell are known to be strongly affected by operating conditions like temperature [18], [52] and aging [53]. Generally, the cell parameters are identified offline and provide a reference value to analyze effects of aging and temperature on these parameters. This also helps in studying the relationship between these parameters and states of the cell.

Special offline testing routines, shown in Figure 7, are designed to extract the parameters and study the effects of aging and temperature using several cells. The offline testing schedule in Figure 7 (a) consists of a static capacity test, Hybrid pulse power characterization (HPPC) test, and Dynamic stress test (DST) as defined by DOE [6], followed by thirty cycles that consists of constant current (CC) discharging and constant current - constant voltage (CC-CV) charging profile to age the cell. This profile is repeated until EOL and all these tests were performed at 25^o C.

Temperature effects are studied by applying the temperature based testing schedule in Figure 7 (b) at 10^o C, 15^o C, 25^o C, and 45^o C. Temperature testing was done using a thermal chamber where the cell was allowed to rest for 24 hours to ensure the cell is at thermal equilibrium. Static capacity test and HPPC test were selected for this schedule as all the cell parameters can be evaluated from these two tests. Four cells are used for the offline testing schedule at 25^o C and for the test at 10^o C, 15^o C and 45^o C, respectively. The current profile and description for all the test implemented is provided in Appendix 1: Testing profiles.

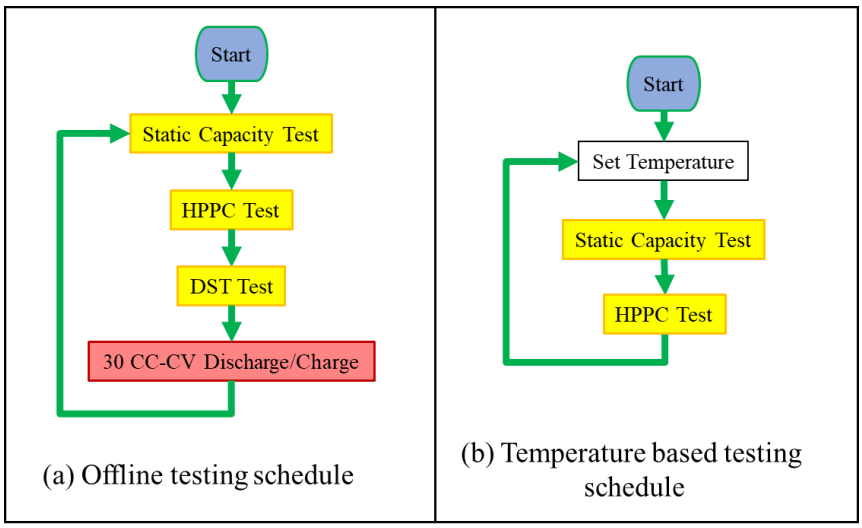

Figure 7. Testing schedules.

2.3.1 Q_{max}

Q_{max} is measured using the static capacity test at every 30 cycles and at a temperature range from 10^{o} C to 45^{o} C while the nominal capacity, Q_{nominal}, for a fresh cell is provided by the manufacturer. The Static capacity test measures the capacity in ampere-hours at a C/3 CC discharge rate corresponding to the rated capacity [6]. Firstly, the cell is fully charged by a CC-CV charging profile, followed by a rest period that takes 2 hours to ensure the cell is at thermal equilibrium. Finally, the cell is discharged until it reaches the lower cut-off voltage.

The measurements from Figure 8 show that Q_{max} decays as the number of cycle's increases but is randomly affected by temperature, with decreased capacity at 10^{o} C and 45^{o} C and increased capacity at 15^{o} C and 25^{o} C.

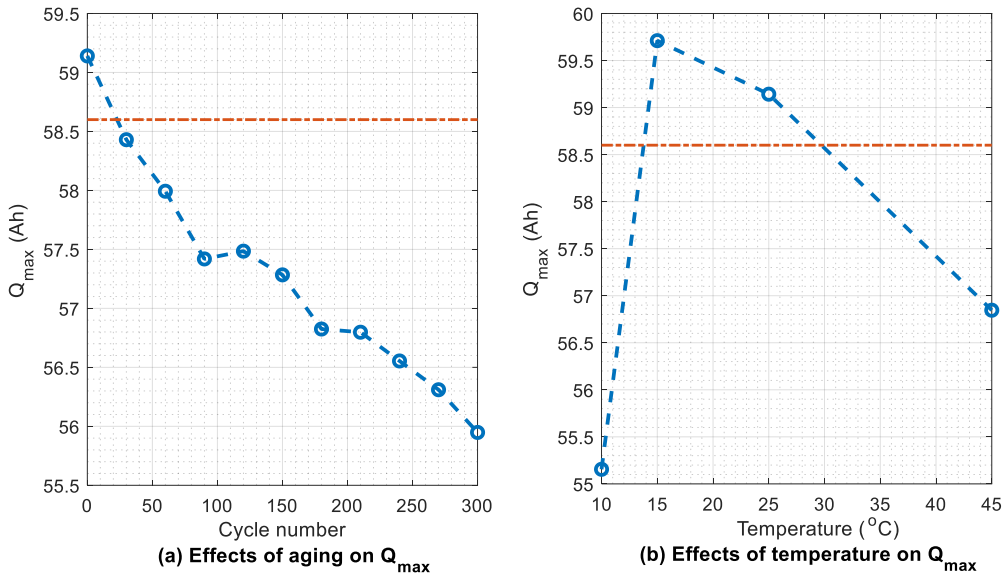

Figure 8. Variation of Q_{max} with (a) aging, (b) temperature.

2.3.2 *OCV*

As OCV is a function of SOC, the *SOC-OCV* relationship is measured using a special pulse discharge test, shown in Figure 9. The pulse current profile consists of a 0.5 C discharge pulse with a duration that discharges the cell capacity by 10%, followed by a one-hour rest period which is repeated till 0% SOC. When no load is connected, the cell reaches an equilibrium state after an extended period of relaxation and there is no change in terminal voltage. Then, the terminal voltage is the same as the OCV and overpotentials can be considered zero.

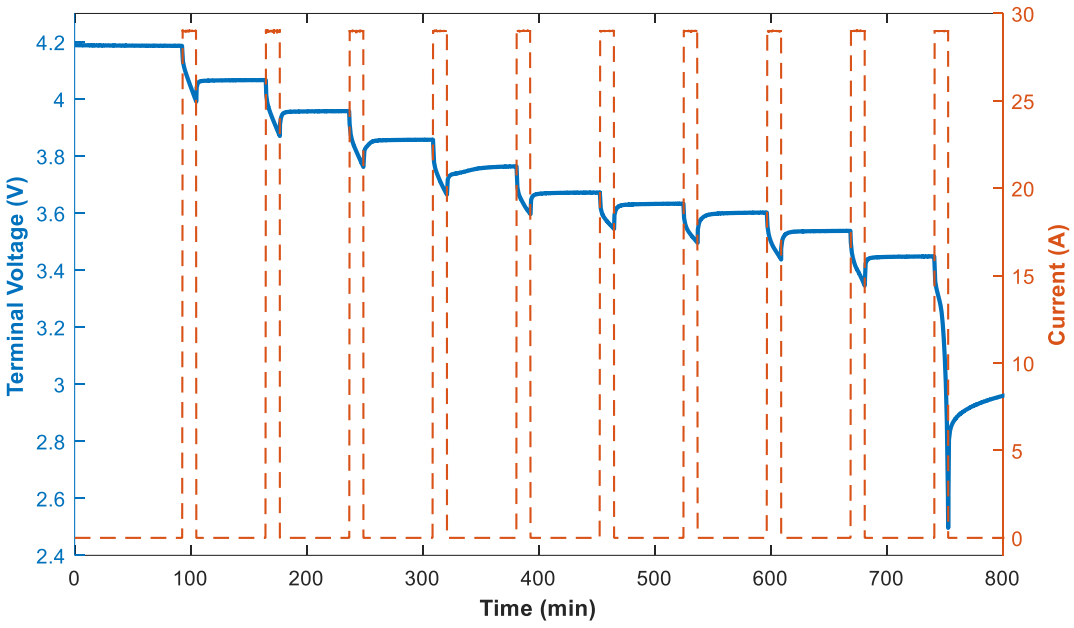

Figure 9. Pulse discharge profile

SOC-OCV curve, measured at 25° C, is shown in Figure 10. The curve, fitted by a ninth order polynomial, is as follows:

$$OCV(x) = p_1x^9 + p_2x^8 + p_3x^7 + p_4x^6 + p_5x^5 + p_6x^4 + p_7x^3 + p_8x^2 + p_9x + p_{10} \quad (26)$$

, where x is the SOC that is normalized about a mean of zero and a standard deviation of 0.3317. A ninth order polynomial was chosen because of the accuracy, where the root mean square error (RMSE) is 0.0049 as compared to those of other lower order polynomials ranging from 0.009 to 0.15. The fitted coefficients results in:

$$p_1 = 0.0568, p_2 = -0.0725, p_3 = -0.2238, p_4 = 0.2792, p_5 = 0.3037$$

$$p_6 = -0.3957, p_7 = -0.1219, p_8 = 0.2649, p_9 = 0.2256, p_{10} = 3.675$$

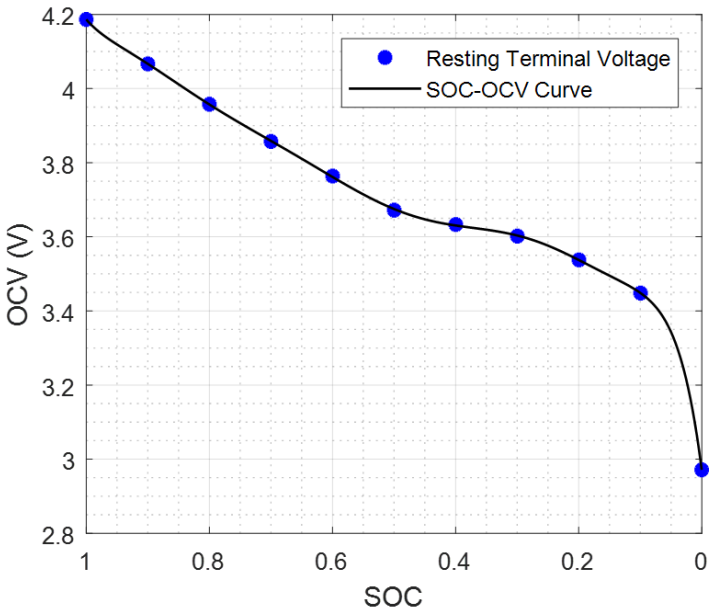

Figure 10. SOC-OCV curve.

The measured *SOC-OCV* curves for different temperatures and number of cycles are shown in Figure 11. In Figure 11 (a) and (c), the value of Q_{nominal} is fixed, equal to Q_{max} at 25^{o} C, while in Figure 11 (b) and (d), the value of Q_{nominal} is varying, equal to the value of Q_{max} at respective temperatures and number of cycles. The SOC-OCV curve varies with temperature and aging, as shown in Figure 11 (a) and (c), when the value of Q_{nominal} is fixed. These variations are noticeable at the end temperatures, 10^{o} C and 45^{o} C, while they vary slowly as the cell is aged. Thus, the SOC-OCV function can be assumed as constant for all aging conditions. These variations are adjusted by updating the value of Q_{nominal} as shown in Figure 11 (b) and (d). Hence, the SOC-OCV curve can be fixed as depicted in Eq. (26) over the entire operation range if the value of Q_{nominal} is updated.

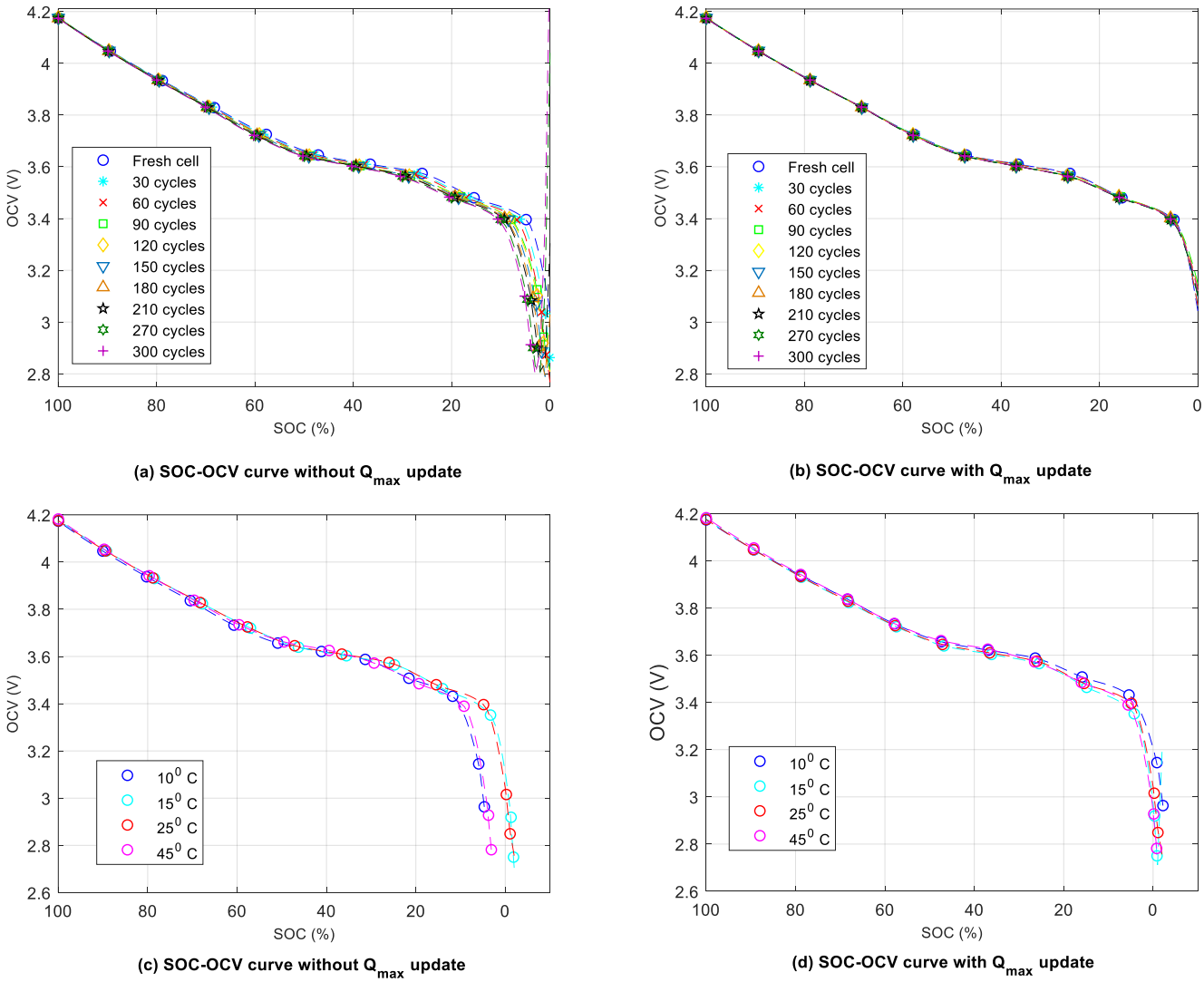

Figure 11. SOC-OCV curve under different aging (a, b) and temperature (c, d) conditions.

2.3.3 Impedance parameters

Parameters $R_0, R_1, \tau_1, \mathrm{R}_2$ and τ_2 were estimated using Non-Linear Least Square (NLLS) from the voltage response at pulse discharge currents. A single pulse current and voltage response, depicted in Figure 12, was analyzed to identify the individual parameters as:

- *Subinterval* S_0 $(t < t_0)$*:* the battery output current is zero and the *SOC* is constant. In addition, the terminal voltage is constant and has reached the $OCV(SOC_1)$.

- *Subinterval* S_1 $(t_0 \leq t < t_1)$*:* the battery is discharged with a constant current $I_{discharge} > 0$. Initially, a steep decrease of the output voltage can be seen due to the internal resistanceR_0, and then continues to exponentially decrease given by the *OCV* (as the SOC is decreasing) and the *RC* circuits.
- *Subinterval* S_2 $(t_1 \leq t < t_2)$*:* the battery current is zero so the output voltage, at first, will have a steep increase due to R_0, and then there is an exponential increase until it reaches $OCV(SOC_2)$.

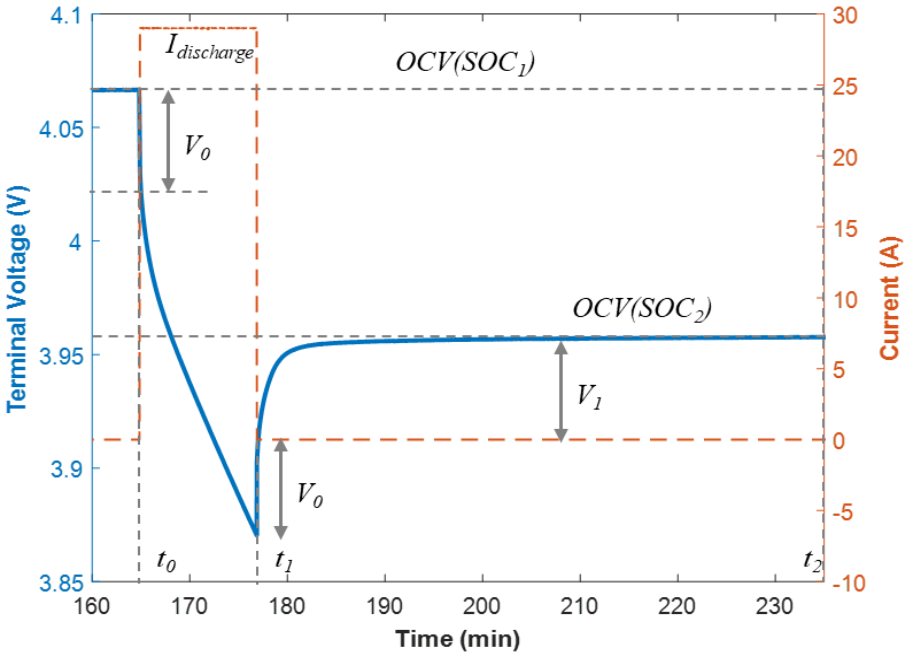

Figure 12. Single pulse profile

From the above analysis, interval S_1 or S_2 can be used to determine the *RC* parameters. Interval S_2 is preferred because (1) *OCV* is constant throughout the interval, (2) current *I* is zero and thus voltage drop due to internal resistance is zero and (3) *SOC* is constant, thus value of the parameters can be estimated at a fixed *SOC*.

$$R_0 = \frac{V_0}{I_{\text{discharge}}} \qquad (27)$$

1. *Internal Resistance* (R_0)*:* R_0 was calculated from the instantaneous voltage drop that takes places when a battery is charged or discharged from a resting state [6], [54]:

$$R_0 = \frac{V_0}{I_{\text{discharge}}} \qquad (28)$$

2. *First Order Model:* To find the first order parameters, two cases are analyzed: (1) Discharging/Charging and (2) Resting. For the first case, subinterval S_1, the value of input current *I* is constant, and Eq. (15) can be modified as:

$$V_{C_1,t_1} = V_{C_1,t_0} e^{-\frac{t_{current}}{\tau_1}} + IR_1\left(1 - e^{-\frac{t_{current}}{\tau_1}}\right) = IR_1\left(1 - e^{-\frac{t_{current}}{\tau_1}}\right) \qquad (29)$$

, where $t_{current}$ denotes the duration $(t_1 - t_0)$ for when the battery is charged or discharged and $V_{C_1,t_0} = 0$. For resting case, subinterval S_2, input current *I* is zero, and Eq. (15) is modified as:

$$V_{C_1,t_1} = V_{C_1,t_1} e^{-\frac{t_{rest}}{\tau_1}} \qquad (30)$$

, where t_{rest} denotes the duration $(t_2 - t_1)$ for when the battery is at rest. The value of $V_{C_1}(t_1)$ is required to more accurately define the dynamics at the beginning of the resting phase. From Eq. (29) and (30), the overpotential V_{C_1} can be defined as:

$$V_{C_1} = \left[IR_1\left(1 - e^{-\frac{t_{\text{current}}}{\tau_1}}\right)\right] e^{-\frac{t_{\text{rest}}}{\tau_1}} \qquad (31)$$

, The output voltage, from equation (16), is:

$$V_t = OCV(SOC) - V_{C_1} \quad (32)$$

Using Eq. (31) and (32), the parameters can be evaluated by methods of non-linear regression. The regression equation is:

$$y = OCV(SOC) - V_t = \left[IR_1 \left(1 - e^{-\frac{t_{\text{current}}}{\tau_1}} \right) \right] e^{-\frac{t_{rest}}{\tau_1}} \quad (33)$$

3. *Second Order Model:* Parameter estimation results for a second order ECM can be obtained using a similar approach as above. Using Eq. (20)-(22), that is simplified for the resting phase, the equation for a second-order ECM is given as:

$$V_{C_1} = \left[IR_1 \left(1 - e^{-\frac{t_{\text{current}}}{\tau_1}} \right) \right] e^{-\frac{t_{\text{rest}}}{\tau_1}} \quad (34), \; V_{C_2} = \left[IR_2 \left(1 - e^{-\frac{t_{\text{current}}}{\tau_2}} \right) \right] e^{-\frac{t_{\text{rest}}}{\tau_2}} \quad (35)$$

$$V_t = OCV(SOC) - V_{C_1} - V_{C_2} \quad (36)$$

The equation in regression form is

$$y = OCV(SOC) - V_t = \left[IR_1 \left(1 - e^{-\frac{t_{\text{current}}}{\tau_1}} \right) \right] e^{-\frac{t_{\text{current}}}{\tau_1}} + \left[IR_2 \left(1 - e^{-\frac{t_{\text{current}}}{\tau_2}} \right) \right] e^{-\frac{t_{\text{rest}}}{\tau_2}} \quad (37)$$

To validate the above method, voltage-current data is simulated using known parameter values. The output voltage response is generated using SIMULINK models. The first and second order SIMULINK based ECMs are shown in Figure 13. The pulse discharge profile is used, and white noise is added to the system to simulate the effects of sensor noises. The standard deviation is assumed as 0.05 A and 0.002 V for the current and voltage sensor respectively. The estimated voltage and parameter identification results for the first order ECM is shown in Figure 14 and

Figure 15 respectively. Similarly, Figure 16 and Figure 17 show the estimated voltage and parameter identification results for the second order ECM.

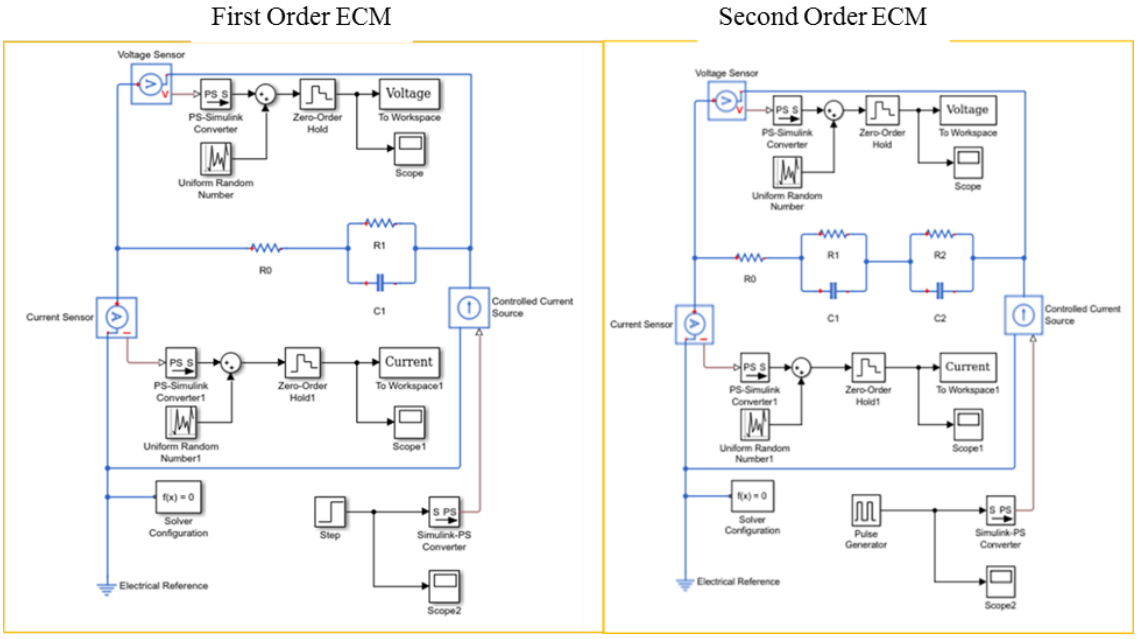

Figure 13. SIMULINK base ECM

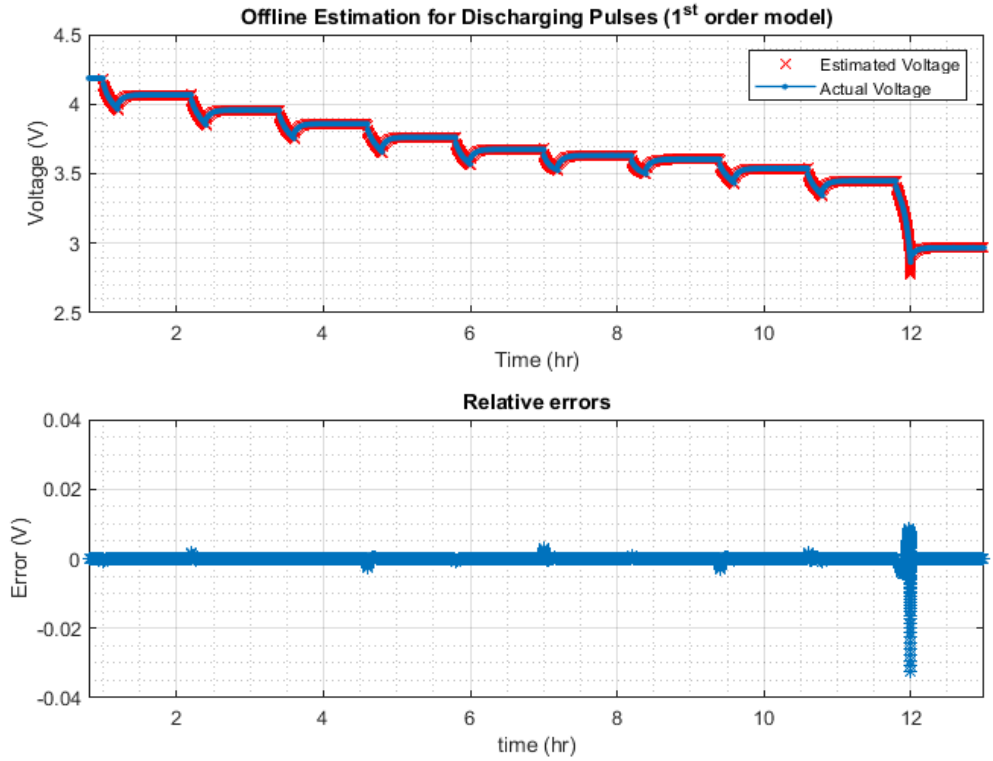

Figure 14. Voltage estimation using offline identified parameters – First Order ECM

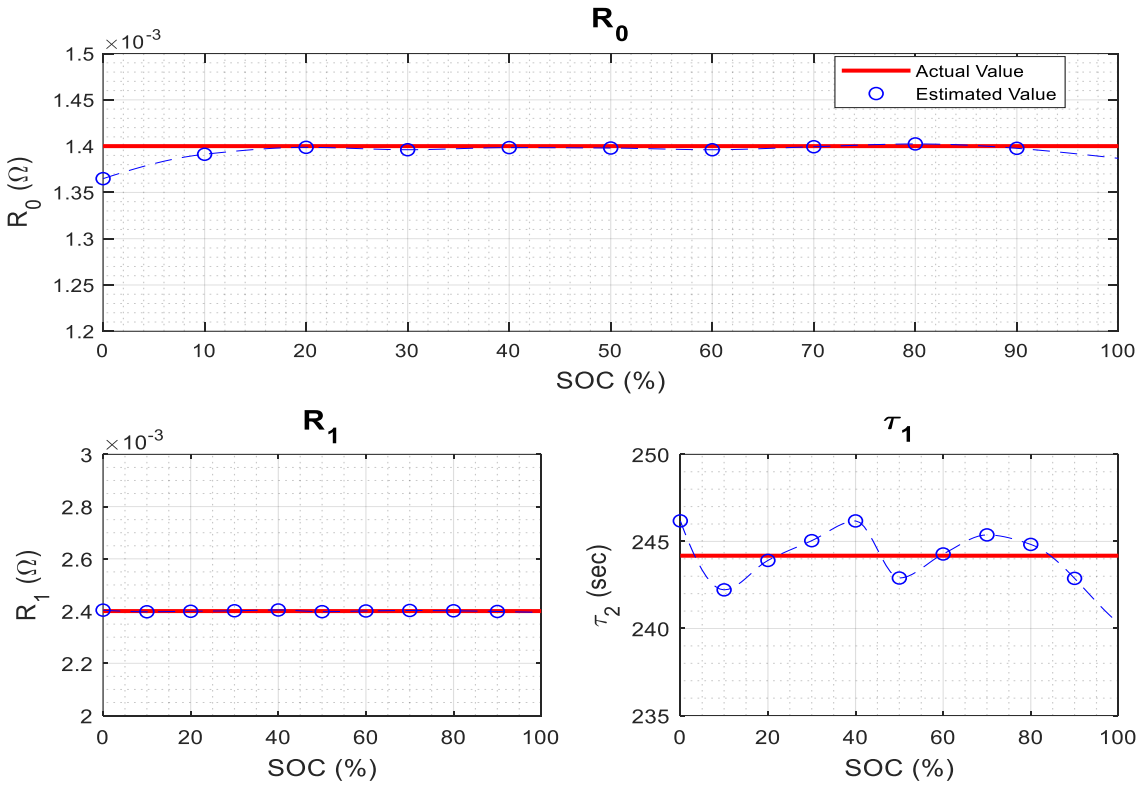

Figure 15. Parameter identification results – First Order ECM

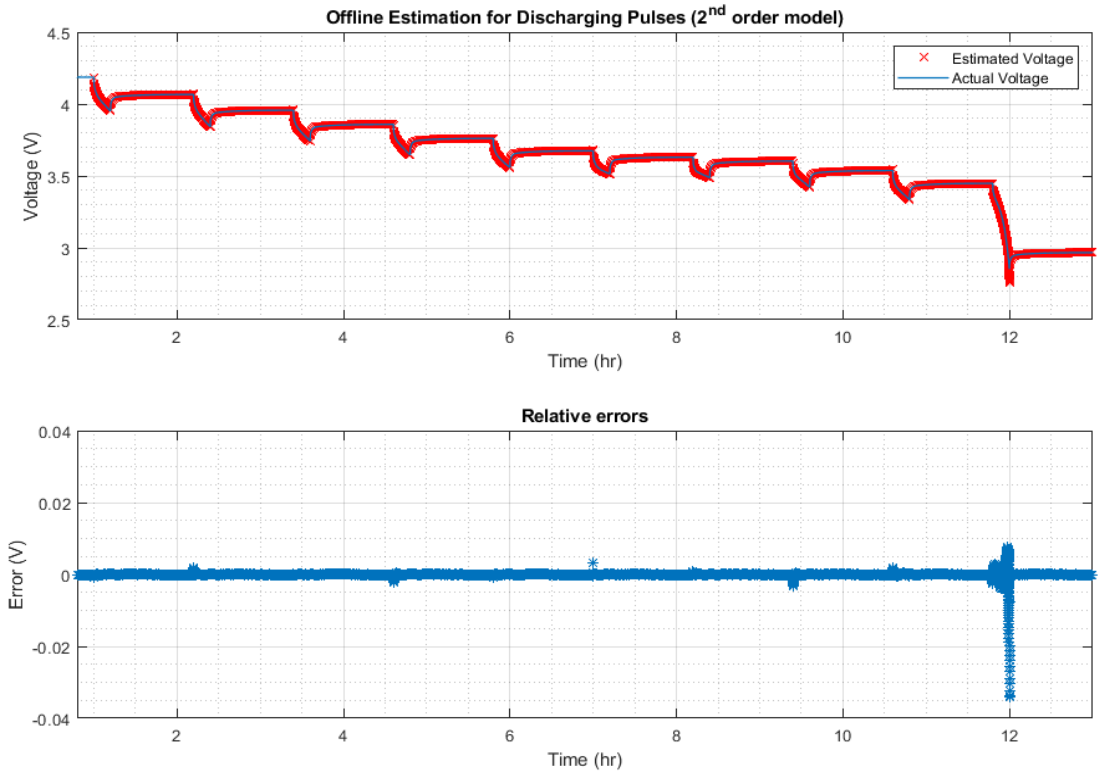

Figure 16. Voltage estimation using offline identified parameters – Second Order ECM

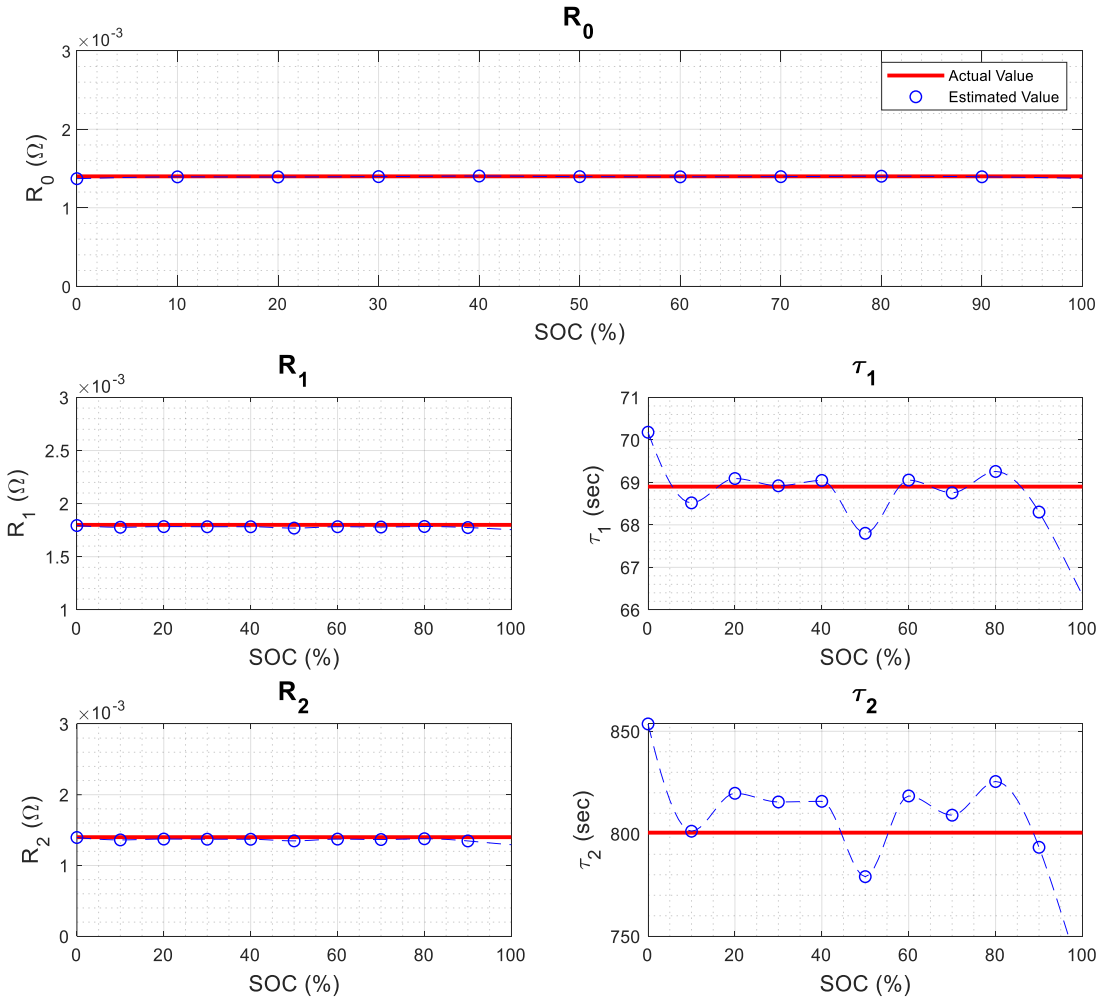

Figure 17. Parameter identification results – Second Order ECM

The offline identification method provides consistently accurate results with an average voltage estimation error that is less than $\pm 2\ mV$ and a maximum value of $-34\ mV$ at very low SOC (<5%) for both first and second order ECM. The relatively higher errors at low SOC is observed due to the rapid change in OCV. Furthermore, the identified parameters are very close to the actual values.

After validating the offline identification method, it was implemented for experimental data and the fitting results are shown in Figure 18. The second order ECM is better able to track the output response of the system for both discharging and resting phase. This is due to the multiple

time constants, which are able to simulate the dynamic response better than first order ECM. Voltage estimation error for the first and second order ECM is shown in Figure 19. The results show high error at very low SOC, similar to the results from simulation data, and is due to the rapid change in OCV. For the higher SOC (100% - 5%) range, voltage errors are less than 26 mV for both the ECMs, where the second order ECM has much lower errors compared to the first order. The second order ECM does show slightly higher errors at certain instances, but these errors reduce significantly at the very next step where it is much lower than those for the first order. For these reasons, the second order ECM is preferred over first order. The parameter identification results for the second order ECM at BOL is shown in Figure 20.

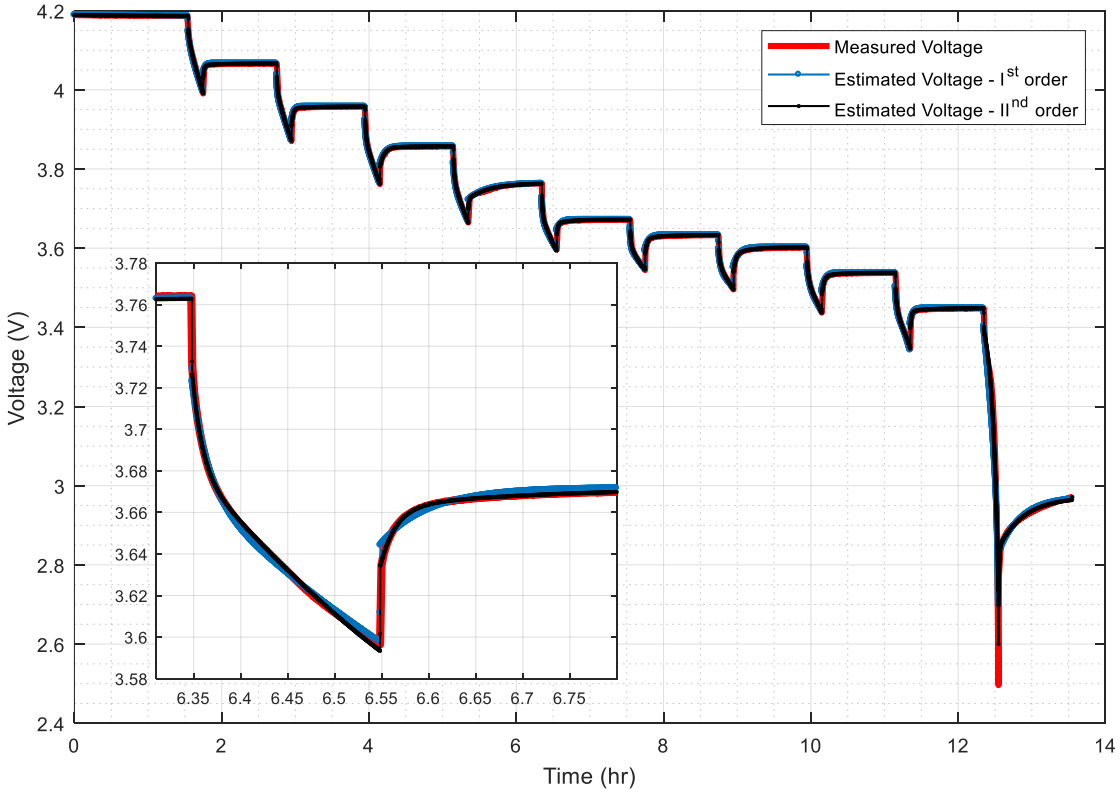

Figure 18. Offline fitting results

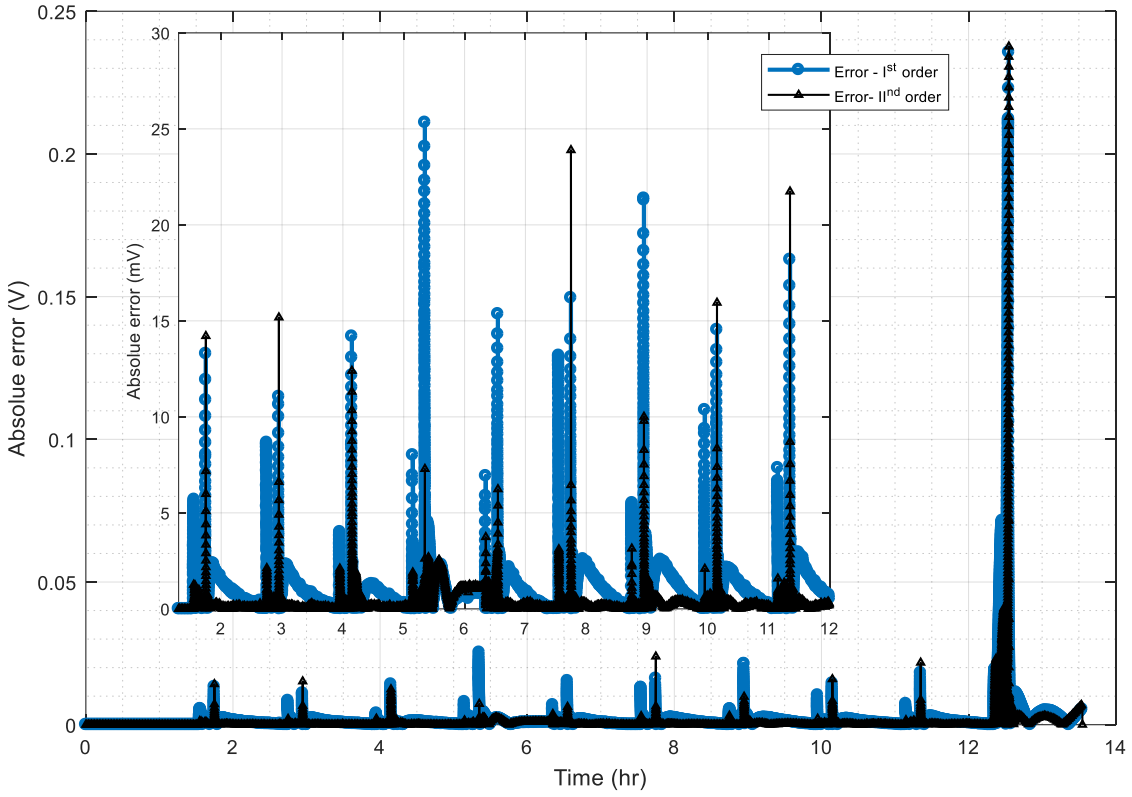

Figure 19. Voltage estimation error for first and second Order ECM

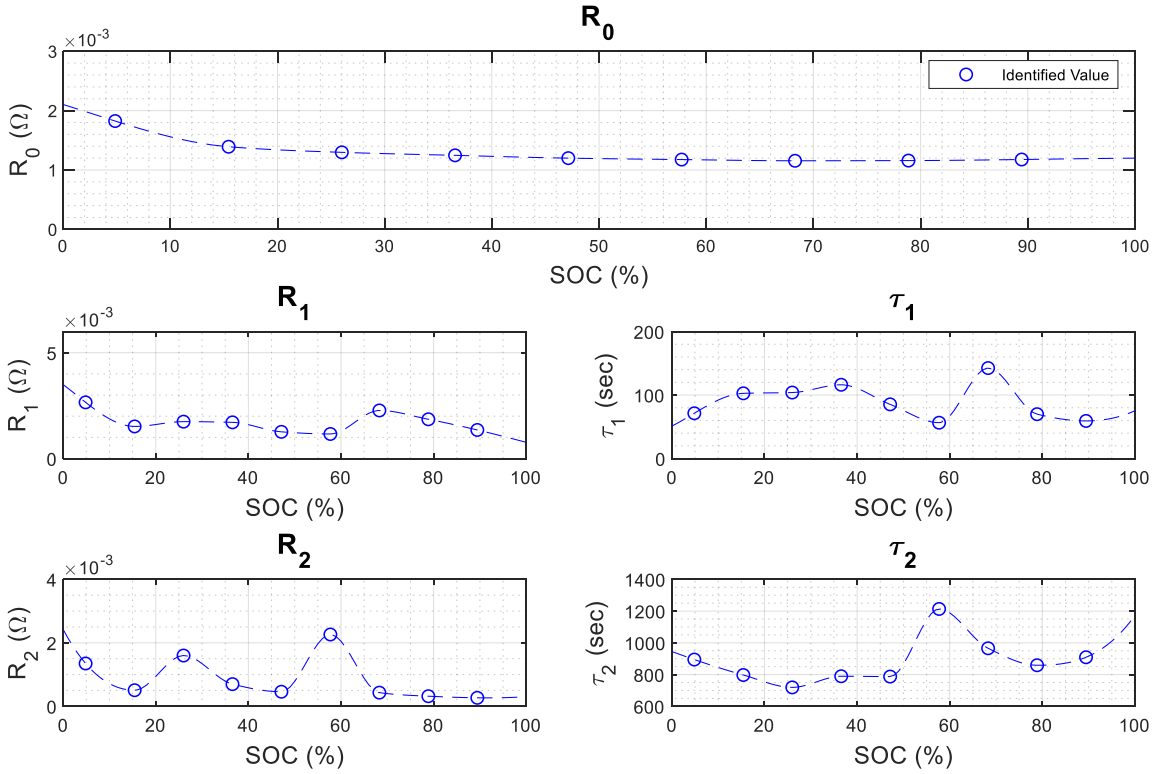

Figure 20. Parameter identification results for second Order ECM

The effects of temperature on the ECM parameters are shown in Figure 21 and Figure 22, where the parameters were obtained using an offline identification method. Resistances generally increase with a decrease in temperature, as observed in Figure 22. Particularly, the internal resistance increases by almost 50% from 45° C to 10° C, but similar to $Q_{\max}$, the ECM parameters also show a nonlinear characteristic with respect to temperature changes. The increase in resistance by cycling is dominantly caused by growth of the SEI layer and low conductivity of the electrolyte [31], which can be identified in Figure 23 and Figure 24, where cell resistances increases linearly as the number of cycles increase.

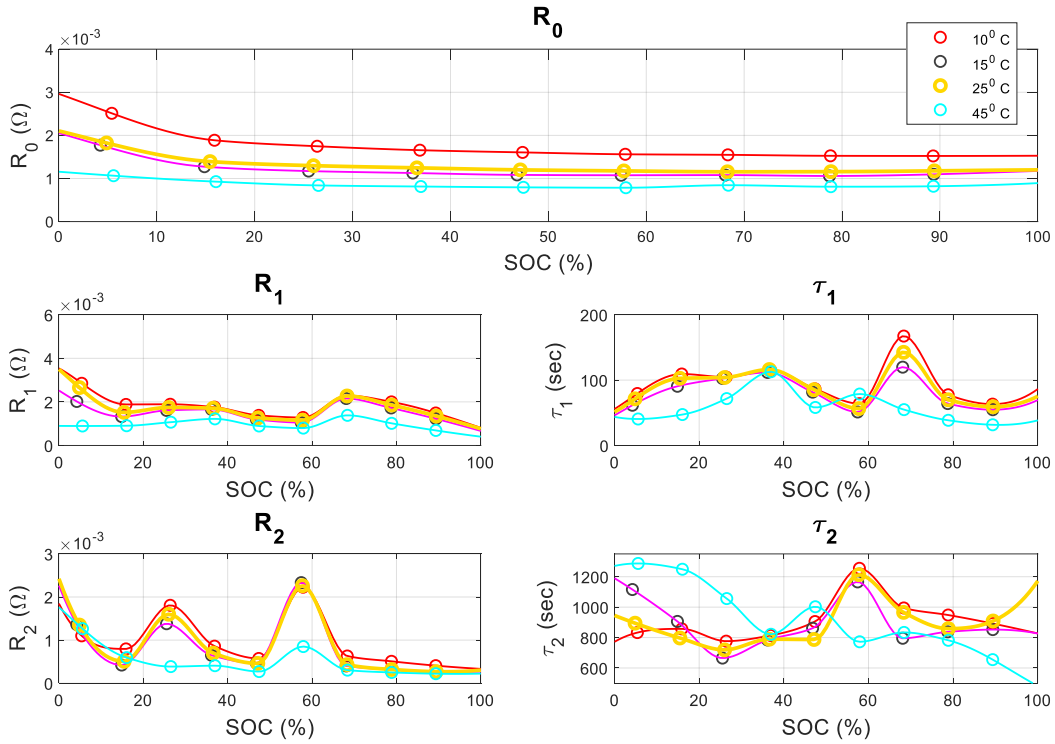

Figure 21. Parameters of the ECM of a fresh cell at different temperatures.

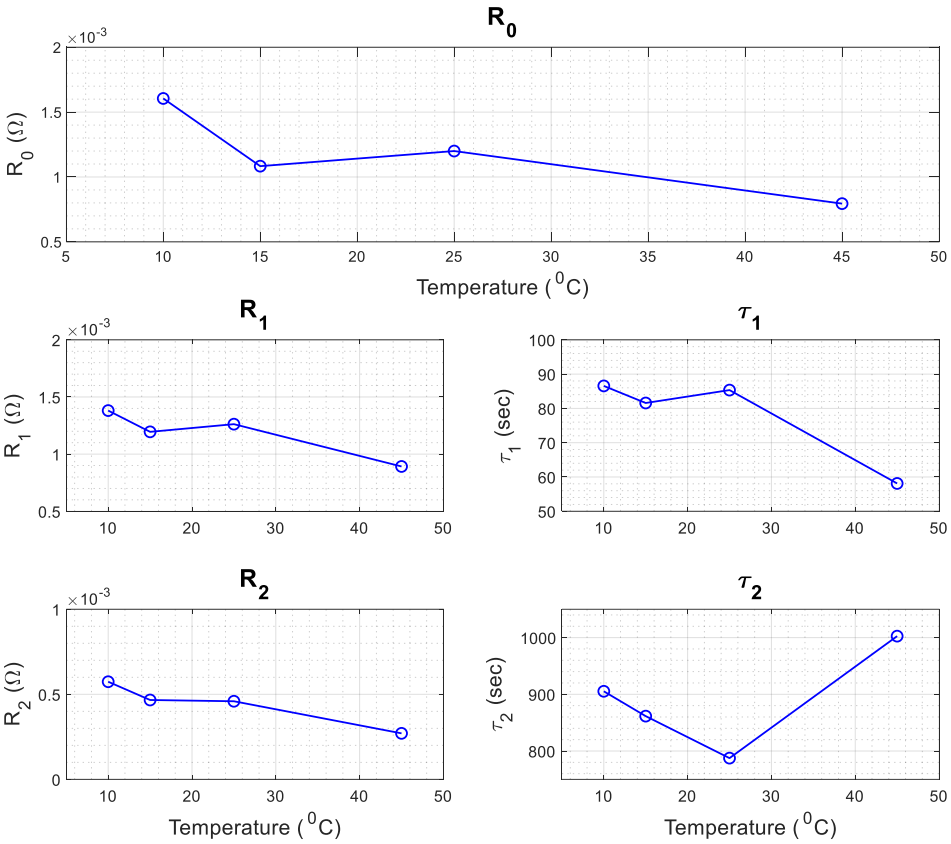

Figure 22. Parameters of the ECM of a fresh cell at 50 % SOC at different temperatures.

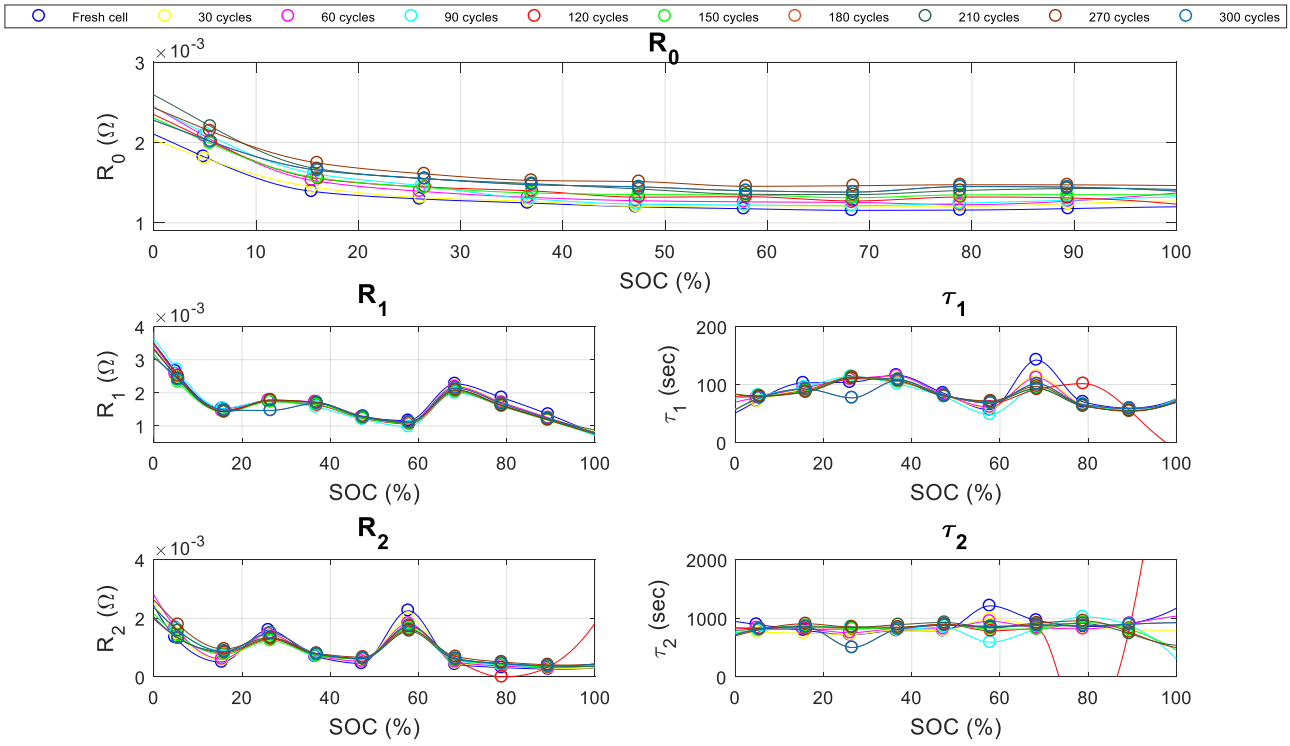

Figure 23. Variation of parameters with aging at 25º C.

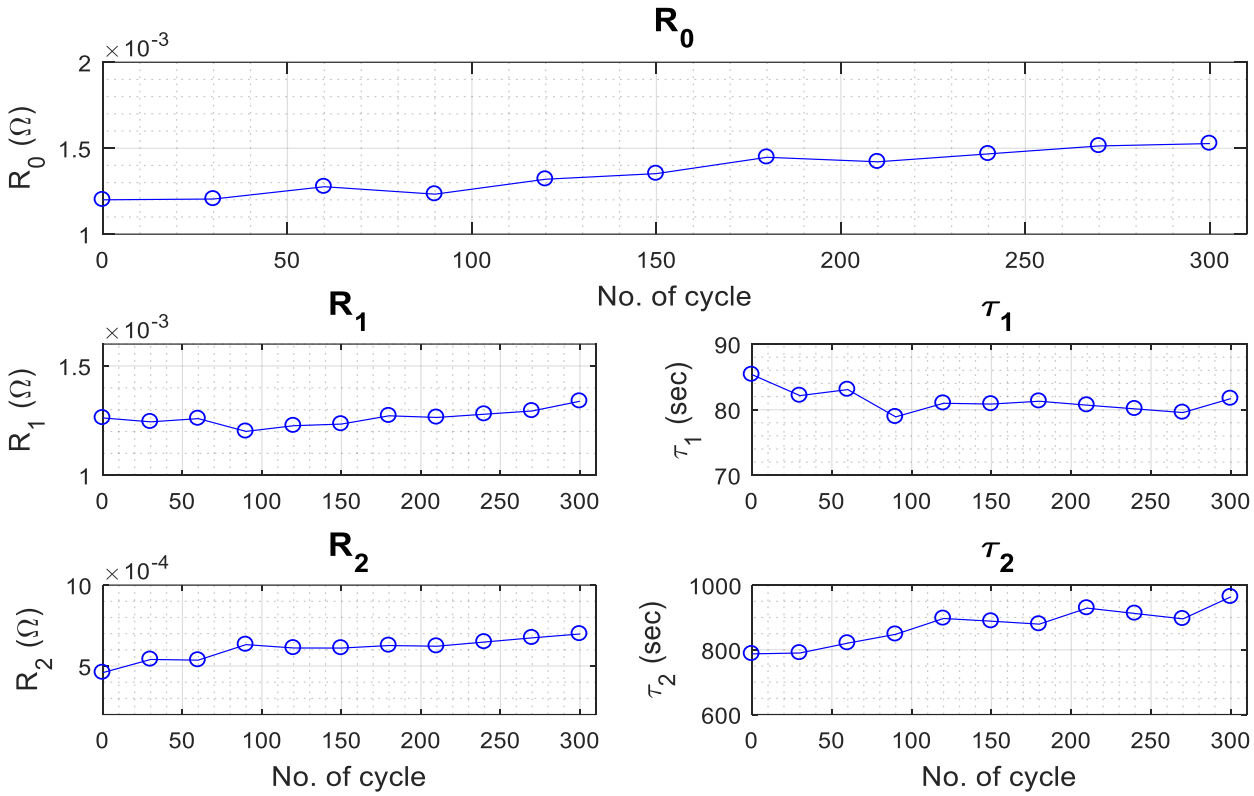

Figure 24. Variation of parameters with aging at 25º C and 50% SOC.

3. SOC and SOH estimation

3.1 Overview

Parameters identified in the previous section are essential for any BMS to monitor the various states of the cell. The parameter values, identified offline, can be used for estimation of states in real time by incorporating look-up tables or empirical functions [18], [53] but require high on-board storage and lack adaptability to characterize the varying dynamics of the cell. Furthermore, extensive experimentation and data collection are required to build the LUTs which need to be repeated if the cell design recipe is changed. For BMSs, online estimation methods that are based on a model-based recursive approach, are preferred due to their adaptability and low memory requirements.

Analysis of cell parameters verifies their dependency on temperature and aging and as such must be estimated simultaneously with the states, SOC and SOH, to ensure accuracy of the estimator. The approach for online estimation is shown in Figure 25. Applied current and terminal voltage are measured and used for the model-based estimator. Then, the estimated parameters are used to calculate the states of the cell. Of all the cell parameters analyzed, Q_{max} is slow varying, with slight change in value over long periods, while the others are fast varying. Since $Q_{\max}$ is slow varying, and does not need to be updated frequently, it is estimated separately using a multiscale approach [16] that reduces computational effort and improves stability of the estimator.

Firstly, the traditional method for online estimation of the fast-varying ECM parameters that include the OCV and Impedance parameters, is analyzed. Once an optimal estimation method is determined, an additional estimator is employed for the slow-varying $Q_{\max}$. The two estimators work in a closed loop framework where the states of the first estimator are used as measurements for the second, while the second estimator provides input states for the first one.

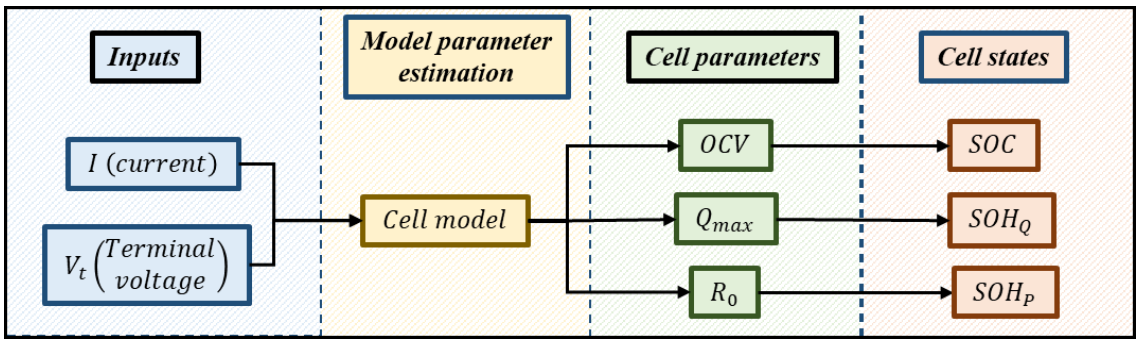

Figure 25. Overview of cell state estimation

3.2 SOC and ECM parameter estimation

Simple Online estimation methods, based on either linear Bayesian estimators like Kalman Filters (KF) [39] and Least Squares (LS) [21], [37] or a Lyapunov based observer [5], are easy to implement and have low computational requirements, but suffer from stability issues [24] and require extensive tuning depending on model and input characteristics which make them more suitable for offline applications. In addition, due to the non-linear relationship of the second-order ECM between the parameters and the states defined by Eq. (20)-(22), advanced nonlinear estimators like Non-linear LS, EKF, UKF, PF, etc. [10], [17], [25], [36], [41], [55], [56], are frequently preferred.

3.2.1 Extended Kalman Filter (EKF)

According to the comprehensive review of methods for online estimation, EKF is the most frequently used estimator and is further investigated for ECM parameter estimation. The EKF is based on the first order Taylor linearization of the nonlinear function. The second order ECM combined with an EKF is proposed in [15]. The internal resistance of battery (R_0) is the only one estimated online because it is the major cause for voltage drop. AEKF based on an improved Thevenin' model, as shown in Figure 6, is proposed in [40] where the parameters of the model are estimated based on state variables. Discrete Extended Kalman Filter (DEKF) is also used to

estimate the parameters and states [23] using separate filters. The nonlinear relation is defined through a parameter dependent error covariance.

Application of EKF for parameter and state estimation has been proposed [39], where an extensive review of the methods verify its ability to estimate the cell states along with the states and parameters of the ECM.

In general, EKF assumes the process has a state vector $x \in R^n$. The process is governed by the non-linear equation,

$$x_{k+1} = f\left(x_k, u_k\right) + Ww_k \qquad (38)$$

, with a measurement $y \in R^m$ that is,

$$y_{k+1} = h\left(x_{k+1}\right) + Vv_{k+1} \qquad (39)$$

, where the random variables, w_k and v_k represent the process and measurement noise vectors and W and V are the associated noise matrices. The process noise w is drawn from a distribution $N(0, Q)$, with covariance matrix Q and measurement noise v is drawn from $N(0, R)$, with covariance matrix R, while w, v, and x are uncorrelated for all possible values of k.

The nonlinear equations $f(.)$ and $h(.)$ can be linearized about a nominal reference trajectory x_k^R and control u_k^R, and nominal noise values w_k^R and v_k^R using Taylor series as:

$$\begin{aligned} x_{k+1} &\approx f\left(x_k^R, u_k^R\right) + \left.\frac{\partial f}{\partial x}\right|_{x=x_k^R}\left(x_k - x_k^R\right) + \left.\frac{\partial f}{\partial u}\right|_{u=u_k^R}\left(u_k - u_k^R\right) + Ww_k \\ &= f\left(x_k^R, u_k^R\right) + A_k\left(x_k - x_k^R\right) + B_k\left(u_k - u_k^R\right) + Ww_k \end{aligned} \qquad (40)$$

$$\begin{aligned} y_k &\approx h\left(x_k^R\right) + \left.\frac{\partial h}{\partial x}\right|_{x=x_k^R}\left(x_k - x_k^R\right) + Vv_k \\ &= h\left(x_k^R\right) + H_k\left(x_k - x_k^R\right) + Vv_k \end{aligned} \qquad (41)$$

, where A_k is an $n \times n$ matrix and H_k is an $m \times n$ matrix defined as:

$$A_k = \left.\frac{\partial f}{\partial x}\right|_{x=x_k^R} = \left[\begin{matrix} \frac{\partial f_1}{\partial x_1}(x) & \cdots & \frac{\partial f_1}{\partial x_n}(x) \\ \vdots & \ddots & \vdots \\ \frac{\partial f_n}{\partial x_1}(x) & \cdots & \frac{\partial f_n}{\partial x_n}(x) \end{matrix}\right]\Bigg|_{x=x_k^R} \quad , \quad H_k = \left.\frac{\partial h}{\partial x}\right|_{x=x_k^R} = \left[\begin{matrix} \frac{\partial h_1}{\partial x_1}(x) & \cdots & \frac{\partial h_1}{\partial x_n}(x) \\ \vdots & \ddots & \vdots \\ \frac{\partial h_n}{\partial x_1}(x) & \cdots & \frac{\partial h_n}{\partial x_n}(x) \end{matrix}\right]\Bigg|_{x=x_k^R}$$

Let us assume that the control input function, u_k is perfectly known, which means $u_k^R = u_k$ and $u_k - u_k^R = 0$. In general, this is a reasonable assumption as u_k is determined by our control system, so there should not be any uncertainty. The error between x_{k+1} and x_{k+1}^R can be defined as:

$$\delta_{k+1} = x_{k+1} - x_{k+1}^R \qquad (42)$$

$$\delta_{(k+1)} = f(x_k^R, u_k) + A_k(x_k - x_k^R) + Ww_k - f(x_k^R, u_k)$$

$$\delta_{k+1} = A_k\delta_k + Ww_k \qquad (43)$$

Similarly, the error between y_k and $h(x_k^R)$ is:

$$\Delta_k = H_k\delta_k + Vv_k \qquad (44)$$

Eq. (43) and (44) result in linear equations and can be used to compute the priori error and error covariance, $\hat{\delta}_{k+1|k}$, and $P_{k+1|k}$ and the posteriori error and error covariance, $\hat{\delta}_{k+1|k+1}$, and $P_{k+1|k+1}$. Using Eq. (42), reasonable estimates of x_{k+1} are:

$$\hat{x}_{k+1|k} = x_{k+1}^R + \hat{\delta}_{k+1|k} \qquad (45)$$

$$\hat{x}_{k+1|k+1} = x_{k+1}^R + \hat{\delta}_{k+1|k+1} \qquad (46)$$

The choice for the reference trajectory is important here. A reasonable value of x_0^R would be $\bar{x}_0$, the mean of the initial state. Based on this:

$$\hat{\delta}_{0|0} = E\left[x_0 - \bar{x}_0\right] = 0 \quad \text{and} \quad \mathrm{P}_{0|0} = P_{x_0}$$

Thus, $\widehat{\boldsymbol{\delta}}_{\mathbf{1|0}} = A_0\widehat{\boldsymbol{\delta}}_{\mathbf{0|0}} = 0$, and the error covariance, based on KF equations, can be defined as:

$$P_{1|0} = A_0 P_{0|0} A_0^T + WQW^T$$

Now, the priori state estimate $\widehat{\boldsymbol{x}}_{\mathbf{1|0}}$ using Eq. (45) is:

$$\hat{x}_{1|0} = x_1^R + \hat{\delta}_{1|0} = f(\bar{x}_0, u_0)$$

Using the equation of Kalman gain at step *k=1*:

$$K_1 = P_{1|0}H_1^T(H_1 P_{1|0} H_1^T + VRV^T)^{-1} \quad \text{and} \quad \hat{\delta}_{1|1} = \hat{\delta}_{1|0} + K_1(\Delta_1 - H_1\hat{\delta}_{(1|0)}) = K_1\Delta_1$$

The posteriori state estimate $\hat{x}_{1|1}$ using Eq. (46) is:

$$\hat{x}_{1|1} = x_1^R + \hat{\delta}_{1|1} = x_1^R + K_1\Delta_1$$

, where $\Delta_1 = H_k\delta_1 + Vv_k = y_1 - h(\hat{x}_{1|0})$ from Eq. (44). Now, to propagate the state to *k=2*, the reference trajectory can be updated to the posteriori estimate obtained at step *k=1*. This new posteriori estimate is, theoretically, a better approximation compared to the priori value. For simplicity, let the priori state and error covariance be denoted as $\hat{x}_k^-$ and P_k^- respectively. Similarly, the posteriori state and error covariance can be denoted as $\hat{x}_k^+$ and P_k^+. Based on this, the EKF algorithm is summarized in Table 4 and a detailed description is shown in Figure 26.

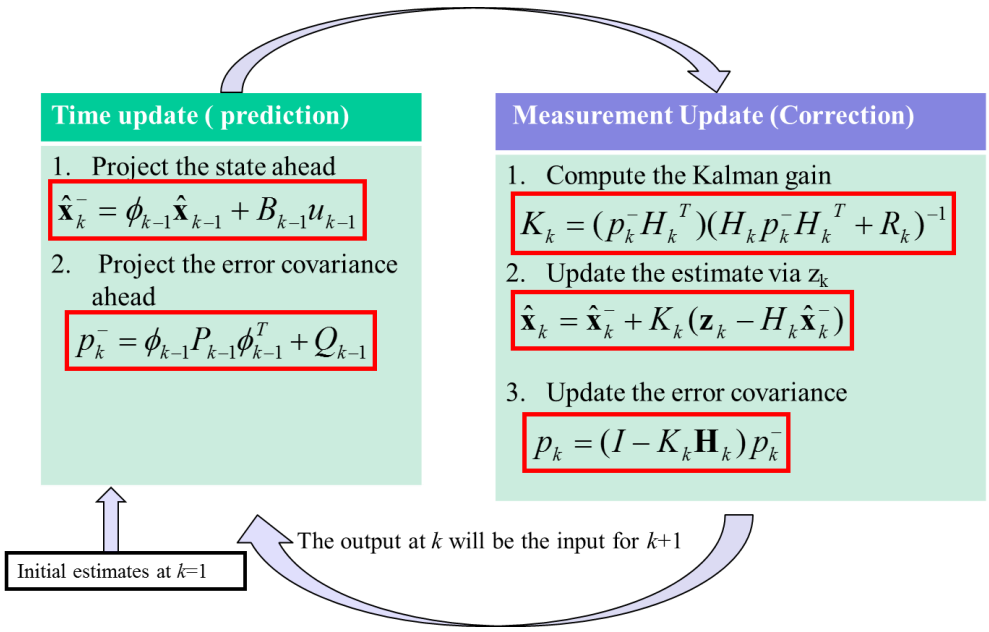

Figure 26. Description of the EKF

Table 4. Algorithm 1 – EKF

Step 1: Initialization –

Initialize $\hat{\boldsymbol{x}}_{\boldsymbol{0}}^{+}, P_0^+, Q \; and \; R$

$\boldsymbol{for\ k = 0, 1, 2, \ldots\ldots, m}$

Step 2: Time update (Prediction) –

$$\hat{\boldsymbol{x}}_{\boldsymbol{k+1}}^{-} = f(\hat{\boldsymbol{x}}_{\boldsymbol{k}}^{+}, \boldsymbol{u_k})$$

$$P_{k+1}^{-} = A_k P_k^+ A_k^T + WQW^T$$

$$A_k = \left.\frac{\partial f}{\partial \boldsymbol{x}}\right|_{\boldsymbol{x=\hat{x}_{k+1}^{-}}}, \qquad H_k = \left.\frac{\partial h}{\partial \boldsymbol{x}}\right|_{\boldsymbol{x=\hat{x}_{k+1}^{-}}}$$

Step 3: Measurement update (Correction) –

$$K_{k+1} = P_{k+1}^{-} H_{k+1}^T (H_{k+1} P_{k+1}^{-} H_{k+1}^T + VRV^T)^{-1}$$

$$\hat{\boldsymbol{x}}_{\boldsymbol{k+1}}^{+} = \hat{\boldsymbol{x}}_{\boldsymbol{k+1}}^{-} + K_{k+1}[\boldsymbol{y_{k+1}} - h(\hat{\boldsymbol{x}}_{\boldsymbol{k+1}}^{-})]$$

$$P_{k+1}^{+} = (I - K_{k+1} H_{k+1}) P_{k+1}^{-}$$

end

3.2.1.1 Design of estimator

State vector *x*, needed for estimation, is $\begin{bmatrix} OCV & V_{C_1} & V_{C_2} & R_0 & R_1 & \tau_1 & R_2 & \tau_2 \end{bmatrix}^T$, from Eq. (20)-(22). Since *OCV* is a function of *SOC*, OCV can be replaced with SOC. Furthermore, SOC is an observable state that can be easily defined using the Coulomb's counting equation given by Eq. (25). The updated state vector is now defined as $\begin{bmatrix} SOC & V_{C_1} & V_{C_2} & R_0 & R_1 & \tau_1 & R_2 & \tau_2 \end{bmatrix}^T$. The state and measurement equation are given as:

$$\begin{bmatrix} SOC_{k+1} \\ V_{C_1,k+1} \\ V_{C_2,k+1} \\ R_{0,k+1} \\ R_{1,k+1} \\ \tau_{1,k+1} \\ R_{2,k+1} \\ \tau_{2,k+1} \end{bmatrix} = \begin{bmatrix} SOC_k - \dfrac{I_k T_s}{3600 Q_{\max}} \\ V_{C_1,k} e^{-\frac{T_s}{\tau_1}} + I_k R_1 \left(1 - e^{-\frac{T_s}{\tau_1}}\right) \\ V_{C_2,k} e^{-\frac{T_s}{\tau_2}} + I_k R_2 \left(1 - e^{-\frac{T_s}{\tau_2}}\right) \\ R_{0,k} \\ R_{1,k} \\ \tau_{1,k} \\ R_{2,k} \\ \tau_{2,k} \end{bmatrix} \qquad (47)$$

$$V_{t,k+1} = OCV\left(SOC_{k+1}\right) - I_{k+1} R_0 - V_{C_1,k+1} - V_{C_2,k+1} \qquad (48)$$

In the above equations Q_{max} is assumed to be a known value and Eq. (47)-(48) needs to be linearized, using a first order Taylor linearization, before the EKF could be implemented. The state space form is:

$$x_{k+1} = A_k x_k + B_k u_k \qquad (49)$$

$$y_{k+1} = H_{k+1} x_{k+1} \qquad (50)$$

Where $\boldsymbol{u}$ is the input current I, $\boldsymbol{y}$ is the measured terminal voltage V_t and the state and measurement matrices are:

$$A_k = \begin{bmatrix} 1 & 0 & 0 & 0 & 0 & 0 & 0 & 0 \\ 0 & e^{-\frac{T_s}{\tau_1}} & 0 & 0 & \left(1 - e^{-\frac{T_s}{\tau_1}}\right) I & \dfrac{V_{C_1} T_s e^{-\frac{T_s}{\tau_1}} - I R_1 T_s e^{-\frac{T_s}{\tau_1}}}{\tau_1^2} & 0 & 0 \\ 0 & 0 & e^{-\frac{T_s}{\tau_2}} & 0 & 0 & 0 & \left(1 - e^{-\frac{T_s}{\tau_2}}\right) I & \dfrac{V_{C_2} T_s e^{-\frac{T_s}{\tau_2}} - I R_2 T_s e^{-\frac{T_s}{\tau_2}}}{\tau_2^2} \\ 0 & 0 & 0 & 1 & 0 & 0 & 0 & 0 \\ 0 & 0 & 0 & 0 & 0 & 0 & 0 & 0 \\ 0 & 0 & 0 & 0 & 1 & 1 & 0 & 0 \\ 0 & 0 & 0 & 0 & 0 & 0 & 1 & 0 \\ 0 & 0 & 0 & 0 & 0 & 0 & 0 & 1 \end{bmatrix} \qquad (51)$$

$$H_k = \left[\frac{\partial OCV\left(SOC_k\right)}{\partial SOC_k} \quad -1 \quad -1 \quad -I \quad 0 \quad 0 \quad 0 \quad 0 \right] \tag{52}$$

$$B_k = \left[-\frac{T_s}{Q_{\max}} \quad 0 \quad 0 \quad 0 \quad 0 \quad 0 \quad 0 \quad 0 \right]^T \tag{53}$$

The matrix A_k, B_k, and H_k are called the Jacobian matrix and needs to be computed at every sample time. To compute H, the differential of the *OCV-SOC* function is required. Using Eq. (26), the $\frac{\partial OCV(SOC)}{\partial SOC}$ can be calculated as shown in Figure 27. After setting up the Jacobian matrices and the differential function, the EKF can be implemented for estimation.

One of the main reasons for implementing an online estimation method is to correct any initialization errors, due to unknown states of the ECM, based on the voltage error between the cell and the ECM. To test the performance of the ECM based EKF, the initial states of the model is set as $\hat{\boldsymbol{x}}_{\boldsymbol{0}}^{+} = \begin{bmatrix} 0.5 & 0.0001 & 0.0001 & 0.002 & 0.003 & 30 & 0.001 & 500 \end{bmatrix}^T$. The true SOC, measured using Eq. (25), is then compared with the estimated SOC along with a comparison of true and estimated voltage and parameters. The values of $\hat{P}_0^+$, Q and R needs to be initialized before EKF algorithmm can be implemented. Using the theoretical definition of the error covariance $\hat{P}$, initial posteriori covariance $\hat{P}_0^+$ is $\hat{P}_0^+ = E\left[\left(\boldsymbol{x_0} - \hat{\boldsymbol{x}}_{\boldsymbol{0}}^{+} \right) \left(\boldsymbol{x_0} - \hat{\boldsymbol{x}}_{\boldsymbol{0}}^{+} \right)^T \right]$ where, true state $\boldsymbol{x_0} = \begin{bmatrix} SOC & 0 & 0 & R_0 & R_1 & \tau_1 & R_2 & \tau_2 \end{bmatrix}^T$ with offline identified values at BOL.

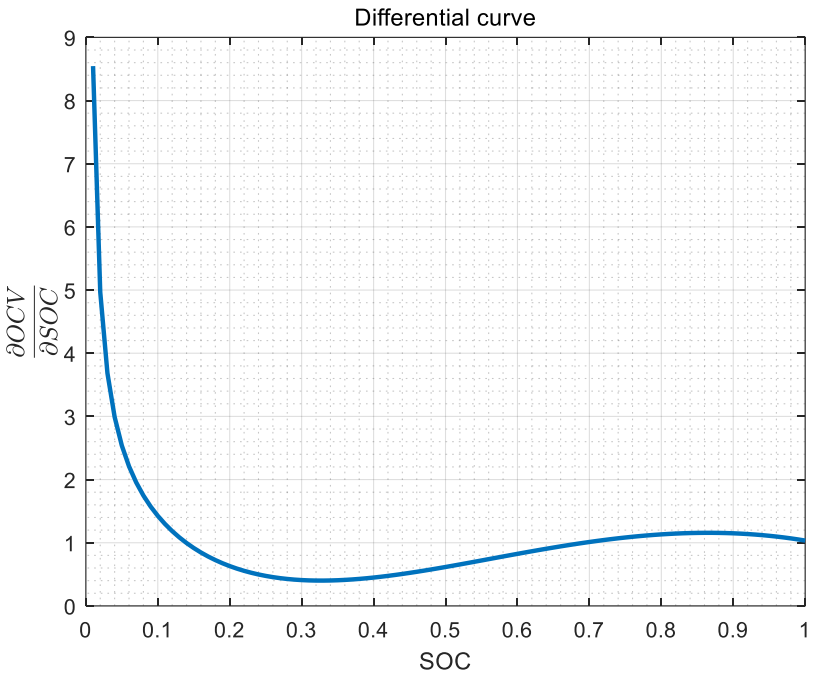

Figure 27. $\frac{\partial OCV(SOC)}{\partial SOC} - SOC$ curve

For practical applications, the true initial value of SOC is unknown, so it is assumed as 0.5 to test the self-correcting capability of the estimator. The algorithm for a discrete time EKF, provided in Table 4, includes two tuning parameters, measurement noise covariance '*R*' and model noise covariance '*Q*', which directly affect the performance of the EKF [57]. *R* can be set as a constant value that can be approximated beforehand by measuring sensor noises as shown in Figure 28, whereas, *Q* is used to improve model errors generally caused by order reduction, approximation, noisy inputs and other factors. Particularly for this case, these model errors are present due to the inability of a second order ECM to accurately represent the complex dynamics of the cell. These errors vary with operating conditions which makes it difficult to approximate *Q*. Thus, the value of *Q* is approximated by trial and error method using multiple testing profiles.

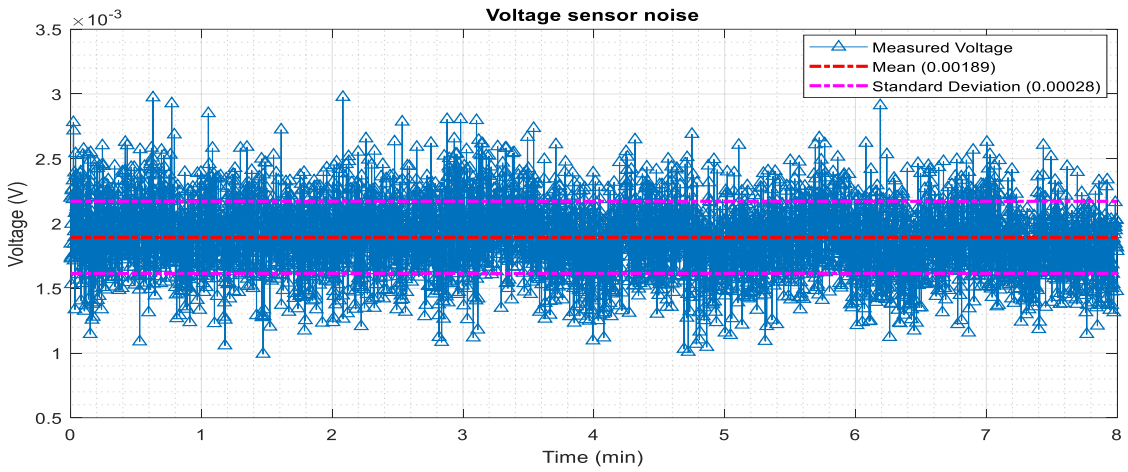

Figure 28. Analysis of voltage sensor noise (measurement noise)

3.2.1.2 Validation and analysis

The performance of EKF is analyzed using a series of testing profiles, including single and multiple cycles where both cases are further subdivided into high excitation and low excitation inputs. Single cycle profiles include HPPC that consists of repeated pulse discharges followed by extended periods of resting that represents a low excitation input, and DST, which is a series of constant power discharge and charge steps that represents high excitation input. Multiple cycles are implemented to analyze long term stability and viability of the algorithm. The cycles consists of a CC-CV profile of ten 0.5 C CC discharge and CC-CV charge cycles, and a driving profile, specially developed to simulate the actual driving characteristics of the cell and test the real-time performance, are implemented. The testing profiles are provided in Appendix 1: Testing profiles.

Estimation results for the HPPC and DST profiles are shown in Figure 29 and Figure 30 respectively, where the SOC value is measured using Coulomb counting and the identified values are obtained from offline experiments. The EKF performs better for the DST profile, due to the high excitation input, compared to the HPPC, with low SOC and voltage estimation errors and good parameter tracking. There is an overall increase in error at the lower SOC range (< 1%) due

to (a) rapid variation of cell parameters, especially OCV, and (b) the offline parameter identification results are poor for low SOC range and cannot be trusted completely.

The EKF is able to track the impedance parameters with better accuracy and quicker convergence rate, as in the case of R_1, for the DST profile due to higher input excitations compared to the HPPC. The parameters identified offline are for the resting case, while the estimation is for a varying current profile. These parameters are known to vary with current profile which leads to the slight error in estimating R_1.

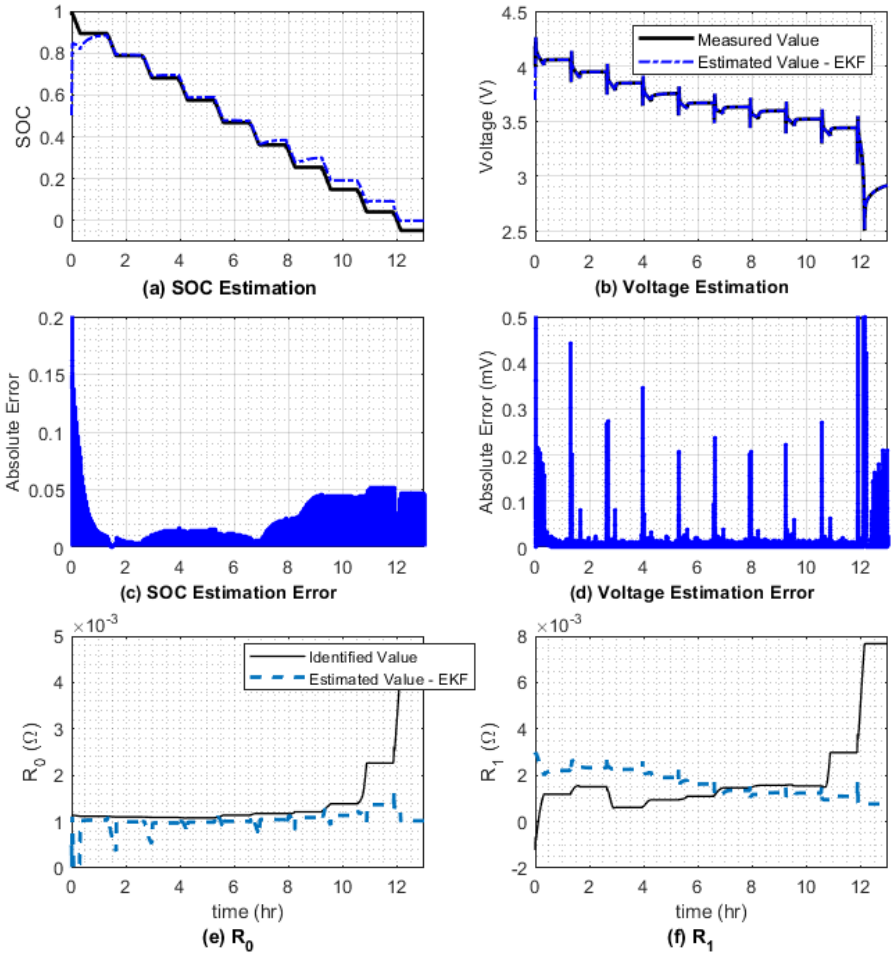

Figure 29. Estimation results using EKF for HPPC test

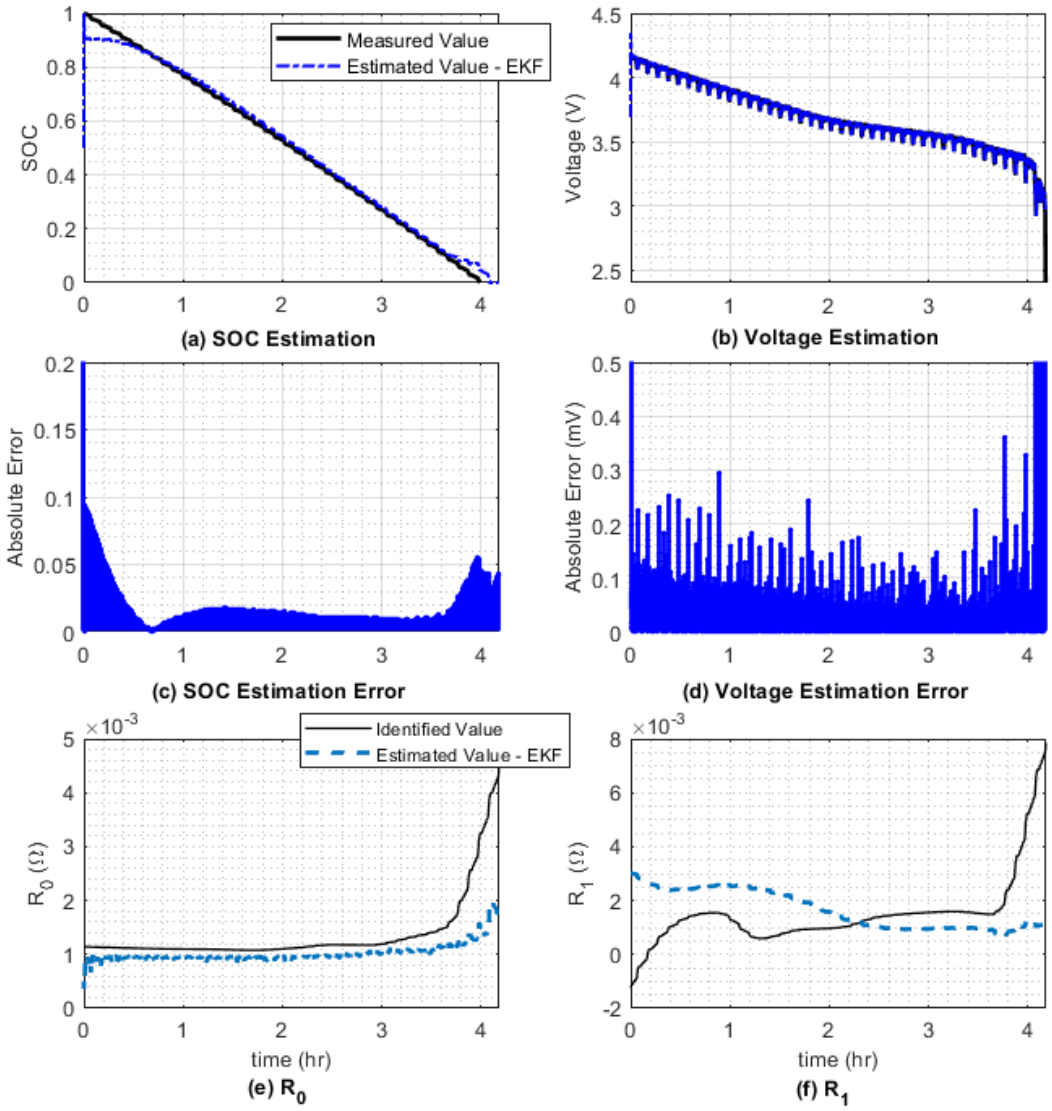

Figure 30. Estimation results using EKF for DST

SOC and voltage estimation results for the first three cycles of CC-CV profile is shown in Figure 31 and for driving profile is shown in Figure 32. The EKF is unable to continuously estimate the SOC and terminal voltage for the CC-CV profile, with high errors at the beginning of the second charging cycle, while the results for the driving profile are highly accurate. This is due to the absence of a sufficiently exciting signal, which causes the state estimator to deviate. In addition, the estimator tends to accumulate state estimation error until it is unable to correct the output value, which leads to the estimator becoming unstable. This behavior is more prominent in parameter

estimation where the results becomes incorrect during the low excitation phase, even for the driving profile, and the estimator is unable to recover back to the correct value. This behavior is known as “bursting phenomenon” [58] and is described in detail in the next chapter.

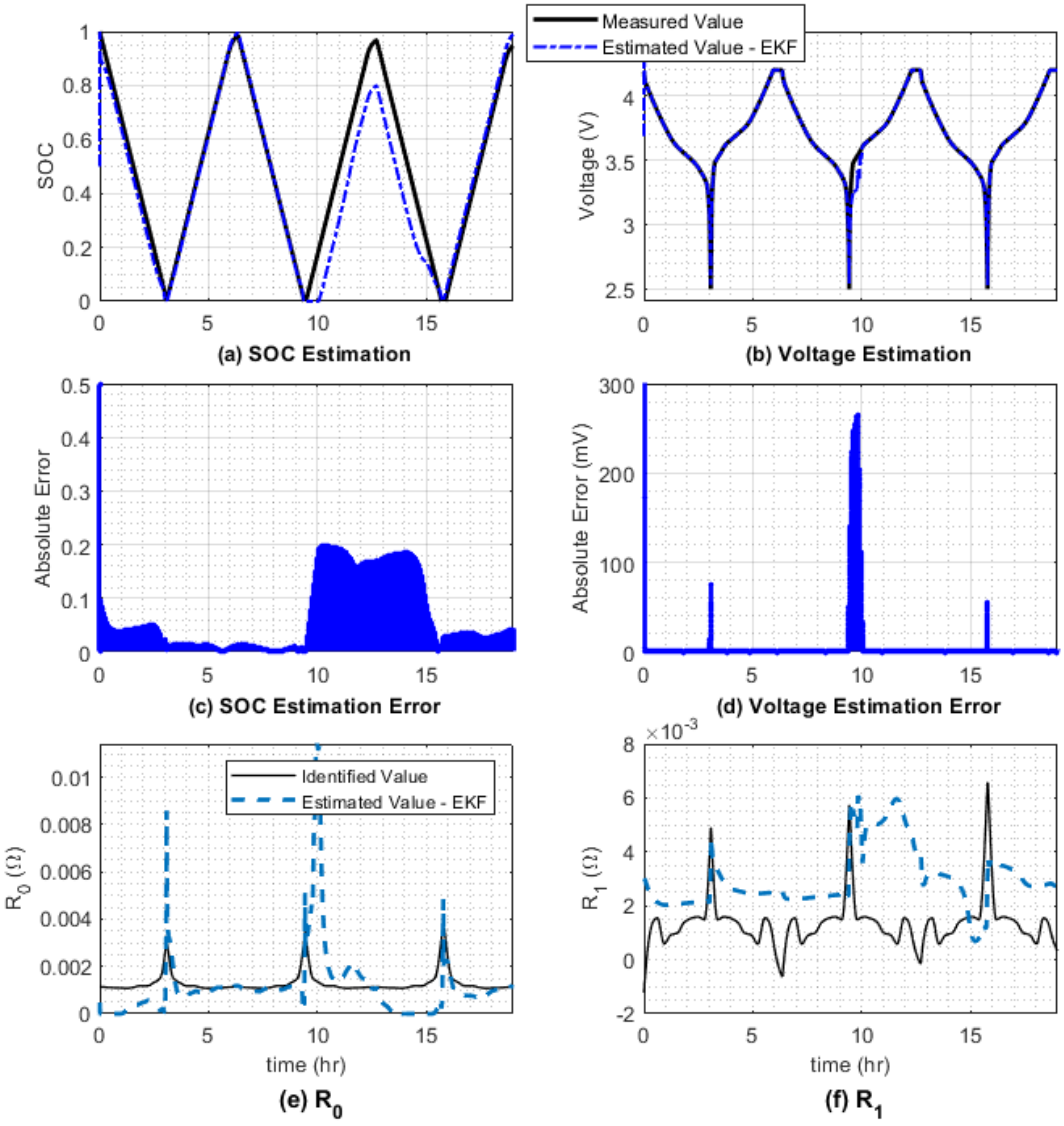

Figure 31. SOC and voltage estimation – CC-CV profile

The EKF is suitable for single cycle estimation, with SOC and voltage estimation error less than 5% and 0.5 mV for the entire operable range (SOC > 0.1%). The accuracy of estimation is known to depend upon several factors, primarily the values of noise covariance’s *Q* and the input signal. This problem associated with tuning the *Q* value has been discussed before. The second

factor is the excitation due to the input signal, which can affect the ability of the estimator to accurately monitor the large number of states.

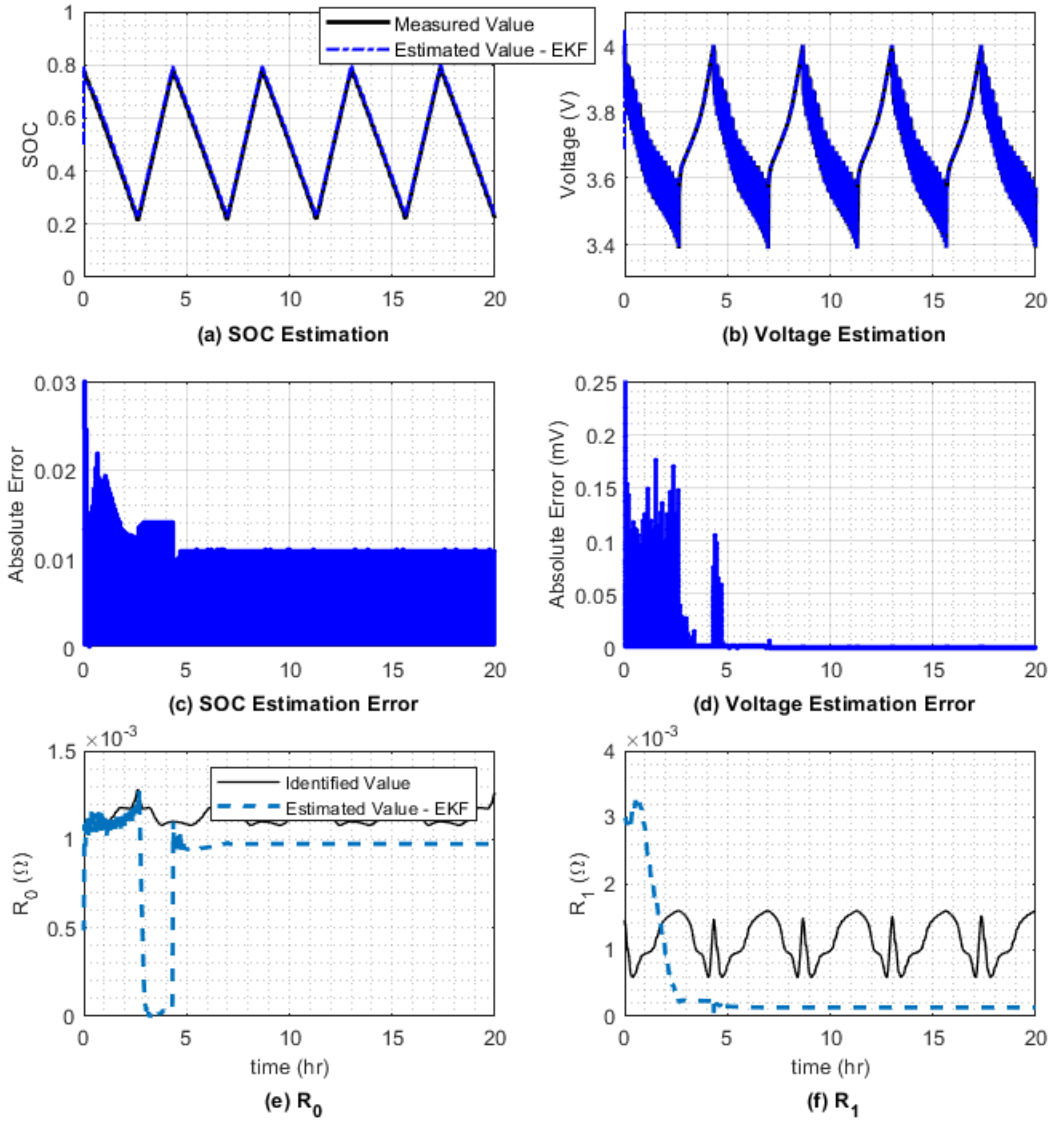

Figure 32. SOC and voltage estimation – Driving profile

3.2.2 Improved estimator algorithm

In the previous section, EKF was implemented for SOC and ECM parameter estimation. The performance of the estimator was evaluated and analyzed using different current profiles. In this section, the drawbacks are discussed in detail, and improvements are proposed to the existing method.

3.2.2.1 Adaptive Extended Kalman Filter (AEKF)

A drawback of the Kalman filter is the dependence of its performance on proper selection of the covariance, Q and *R*. A Kalman filter assumes that the covariance of both the process and the measurement noise is known. Thus, inappropriate initial noise information can lead to poor performance. Therefore, the covariance values can be estimated and changed adaptively using an adaptive EKF (AEKF). AEKF methods are classified into four general categories [10], [40], 1) Bayesian, 2) maximum likelihood, 3) correlation, and 4) covariance matching. The AEKF employing the covariance matching approach is proposed here.

The AEKF, using the filter's innovation sequence, allows the covariance, Q_k, and R_k to be estimated and updated iteratively using the error in estimation. In EKF, the error between the actual measurement, y_k and the predicted measurement $\hat{y}_k^-$ at any time step k can be written as:

$$e_{k,y} = y_k - \hat{y}_k^- = y_k - H_k\hat{x}_k^- = H_k\left(\hat{x}_k - \hat{x}_k^-\right) + v_k \qquad (54)$$

The error covariance is then,

$$C_v = E\left[e_{k,y}e_{k,y}^T\right] = H_k P_k^- H_k^T + R_k \qquad (55)$$

This covariance can be calculated accurately only if all the possible values of e are known. For simplification, an approximation $\hat{C}_v$ is defined as the statistical sample variance estimate of the actual C_v. This approximate $\hat{C}_v$ can be computed by averaging the sum of errors for a small window rather than utilizing the whole dataset, which reduces the computational load and makes the method practically applicable. In addition, continuously updating the estimation window to include the new observations further improves the reliability and robustness of calculation. This method is called the moving window approximation. For an estimation window of size m, $\hat{C}_v$ can be calculated as:

$$\hat{C}_v = \frac{1}{m}\sum_{i=i_0}^{k}\left(e_{k-i,y}\right)\left(e_{k-i,y}\right)^T \qquad (56)$$

, where $i_0 = k - m + 1$. Using Eq. (55) and (56), the measurement noise covariance R_k can be approximated as:

$$\hat{R}_k = \hat{C}_v - H_k P_k^- H_k^T \qquad (57)$$

The process noise w_k is defined as:

$$w_k = x_{k+1} - \hat{x}_{(k+1)}^- - x_k + \hat{x}_k \qquad (58)$$

Converting Eq. (58) in covariance form,

$$Q_k = P_{k+1} - P_k + R_{\hat{x}_k - \hat{x}_{k+1}} \qquad (59)$$

Again, using moving window approximation,

$$\hat{Q}_k = P_{k+1} - P_k + \frac{1}{m}\sum_{j=j_0}^{k}(\hat{x}_j - \hat{x}_j^-)(\hat{x}_j - \hat{x}_j^-)^T \qquad (60)$$

, where $j_0 = k - m + 1$. Substituting $\hat{x}_j - \hat{x}_j^- = K_k e_{k,y}$, $\hat{Q}_k$ can be approximated as:

$$\hat{Q}_k = K_k C_v K_k^T \qquad (61)$$

The only unknown now is the size of the moving window '*m'*. The size "weighs" the errors and must be selected such that it provides sufficient time steps for the filter to stabilize. The moving- window based covariance matching method to update *Q* is shown in Table 5.

Table 5. Algorithm 2 – Moving window-based covariance matching

$$\hat{C}_v = \frac{1}{m}\sum_{i=1}^{m}\left(\boldsymbol{e_{k-i,y}}\right)\left(\boldsymbol{e_{k-i,y}}\right)^T$$

$$\hat{Q}_k = K_k \hat{C}_v K_k^T$$

3.2.2.2 Variable model framework

The performance of an adaptive EKF for long term parameter estimation is dependent on the Identifiability of the system, which is affected by persistency of excitation of the input signal [59]–[62]. Identifiability refers to uniqueness of the model parameters, determined using the input–output data, whereas, persistency of excitation describes the frequency variations in a signal. The adaptive identification of a system requires persistently exciting inputs in order to ensure (exponential) convergence of the adaptive procedures [63], where a signal is called persistently exciting signal if it is frequency rich. The absence of this persistently exciting input can lead to errors caused by covariance windup, causing the estimator to become unstable. These errors are difficult to identify and correct as the accuracy of estimated output is not affected, while the estimated states and parameters deviate from the true value in the absence of adequate excitation. In addition, the parameters of the ECM being estimated are already prone to Observability and Identifiability issues [65].

All these issues can be resolved by implementing a variable model (VM) framework approach, where, the number of observer states are decided dependent on the input signal, i.e., certain estimator states are "shut down" (not estimated) if the system is not persistently excited. Thus, the persistency of excitation decides the order of the model being estimated, i.e., lower the order of persistency, more the number of estimator states that shut down. By reducing the number of states, the accuracy of the estimator can be maintained even with low excitation inputs, as summarized in Table 6.

Table 6. Algorithm 3 – Variable model framework

Step 1: Observe input signal
if $(\boldsymbol{u_k} - \boldsymbol{u_{k-1}}) = \mathbf{0}$
$\delta = \delta + 1$
else
$\delta = 0$
Step 2: Update number of states
if $\delta > \vartheta$
$n = 4$
else
$n = 8$
if $\boldsymbol{y_k}$ >=*Cut-off Voltage*
$n = 1$
end

The proposed framework works in one of three different modes; 1) High excitation mode, 2) Resting or Low excitation mode and 3) CV mode. The input signal is constantly monitored and the number of steps for which there is no change is calculated as δ. If δ exceeds a predefined period ϑ, the system is said to be in "Resting and Low excitation mode", otherwise, if the input signal is varying, the system is in "High excitation mode". Lastly, if the cut-off voltage is reached while the input current is not zero, the system is in "CV mode".

In "High excitation mode", all eight states in the state vector x are estimated and the estimator operates normally as described in the earlier section. In "Resting and Low excitation mode", the state vector is now reduced to four states, given as $\begin{bmatrix} SOC & V_{C_1} & V_{C_2} & R_0 \end{bmatrix}$. Since the mentioned states and parameters are observable and uniquely identifiable, they do not cause any stability issue even during low excitation conditions, while the parameters of the two *RC* circuits suffer from Observability or Identifiability issues [24]. Finally, for the "CV mode", the number of states is reduced to one, i.e., $[SOC]$. During the CV charging, the ECM parameters and the SOC-OCV curve changes rapidly which reduces the estimation accuracy, thus reducing the number of states is preferred.

The proposed VM framework ensures a stable estimation for extended periods without the need for more computationally expensive methods like UD factorization [66] or describing a forgetting factor to prevent covariance windup. The choice of time period $\mathcal{G}$ is based on the time constant τ, which describes the frequency of signal required to identify these parameters. Since the larger time constant, as identified using the offline method, is $\tau_2 = 20$ minutes, $\mathcal{G}$ is chosen as 40 minutes, which is twice the time constant and gives the estimator enough time to estimate all parameters and "shut down" subsequently, reducing a chance of covariance windup. The block diagram for the proposed VM-AEKF is depicted in Figure 33.

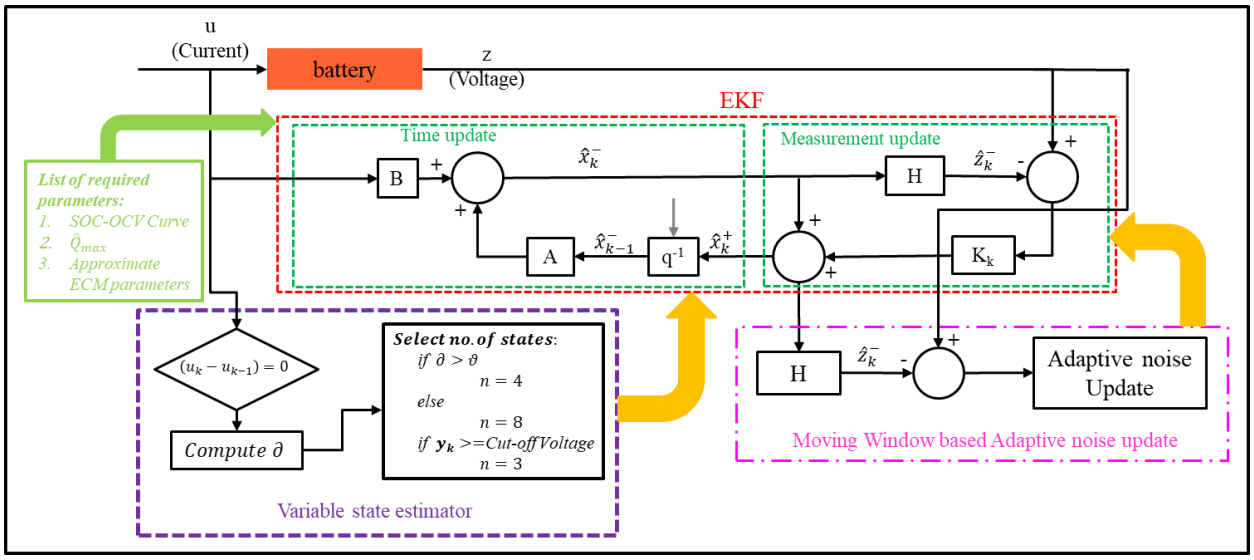

Figure 33. VM-AEKF framework

3.2.2.3 Validation and analysis

For the proposed VM-AEKF, all the initial values are the same as those for the traditional EKF except for noise covariance matrix *Q*, which is initialized as a zero matrix. The performance of the proposed estimator is evaluated using similar profiles as for the traditional EKF.

Comparison of single cycle results for the VM-AEKF and EKF is shown in Figure 34-Figure 35. The voltage estimation results are slightly higher for the VM-AEKF while it performs better for SOC estimation, with lower errors and faster convergence, compared to the EKF.

Improvement in parameter estimation results highlights the advantages of the VM-AEKF with quicker convergence of the estimated states and better tracking compared to the EKF.

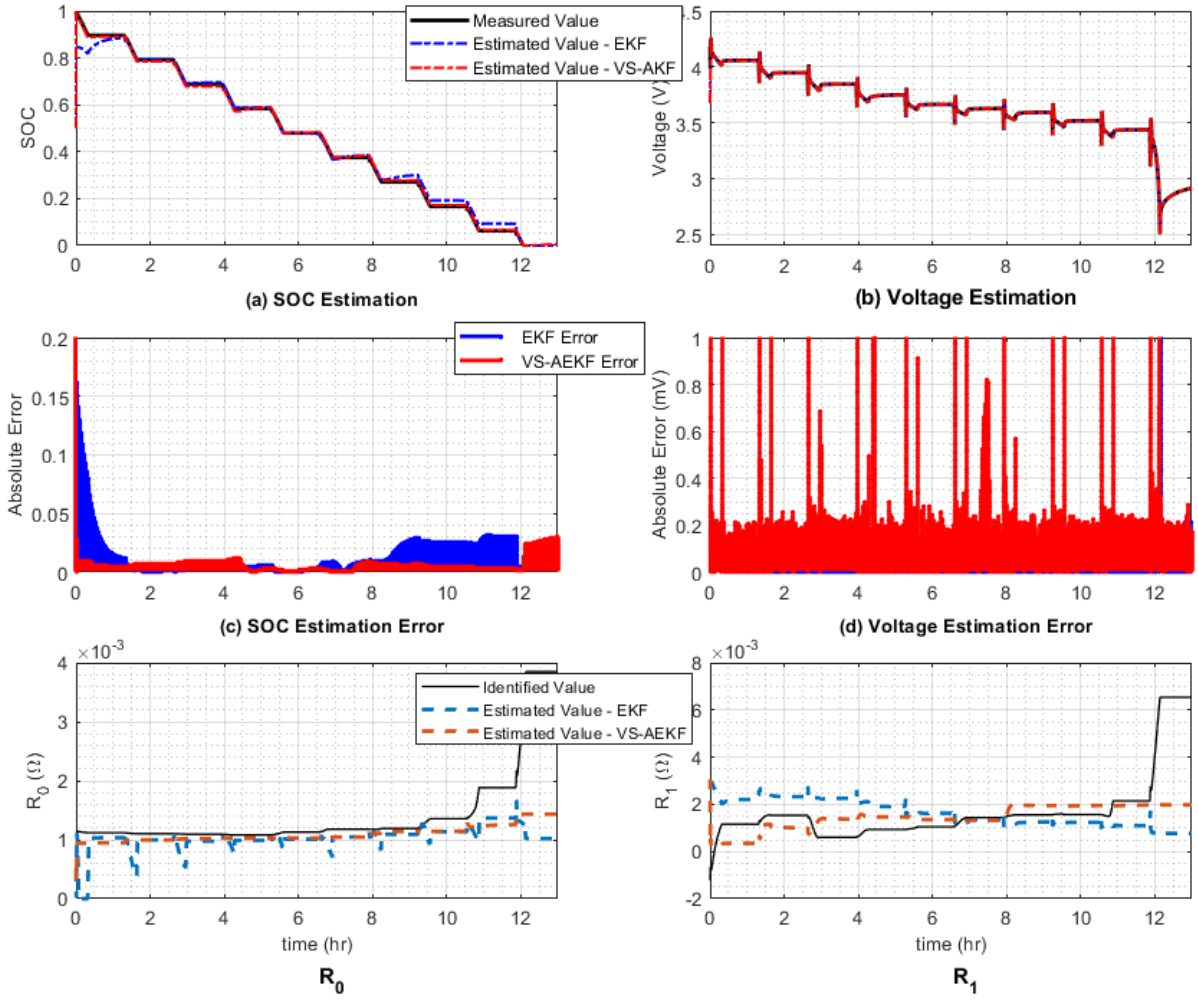

Figure 34. Comparison of estimation results using EKF and VM-AEKF for HPPC

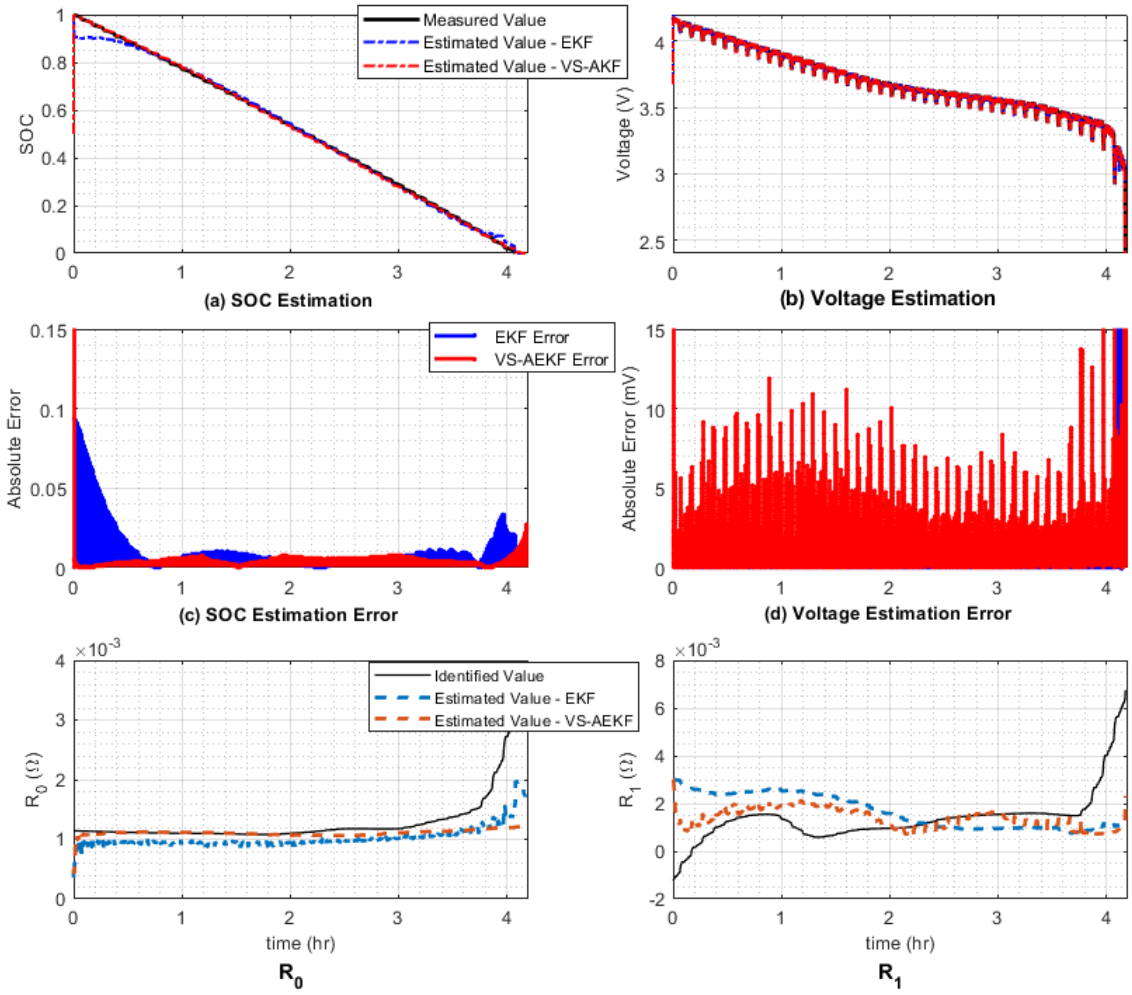

Figure 35. Comparison of estimation results using EKF and VM-AEKF for DST

On comparison of the proposed VM-AEKF and the traditional EKF, the advantage of the former is seen particularly at extended periods of low excitation input condition, as shown in Figure 36 for the CC-CV profile. Both the SOC and voltage estimation are improved along with better stability. Results for the driving cycle, shown in Figure 37, are similar for both estimators, which is expected due to the high excitation signal. Parameter estimation results benefit the most from the VM framework with more stable and consistent results and improved accuracy of estimation. The higher value of estimated R_1 *and* R_0 is due to the aging of the cell. The driving cycles were implemented after 10 CC-CC and CC-CV cycles, and as such the cell is aged by this time which causes an increase in resistance.

Thus, by implementing the VM framework, the errors due to low excitation signals are reduced and the estimation results overall are improved. The adaptive noise update also improves the stability of the estimator and removes the need of multiple trials for approximating a suitable *Q* value. Even though the voltage estimation error is higher than EKF, they are within acceptable limits with a max error of 24 mV excluding at very low SOC ranges, and the improvements to state estimation results are noticeable for the VM-AEKF. However, even though the VM-AEKF is able to reduce the error in ECM parameter estimation significantly, a persistently excited signal is required to accurately estimate and track these parameters.

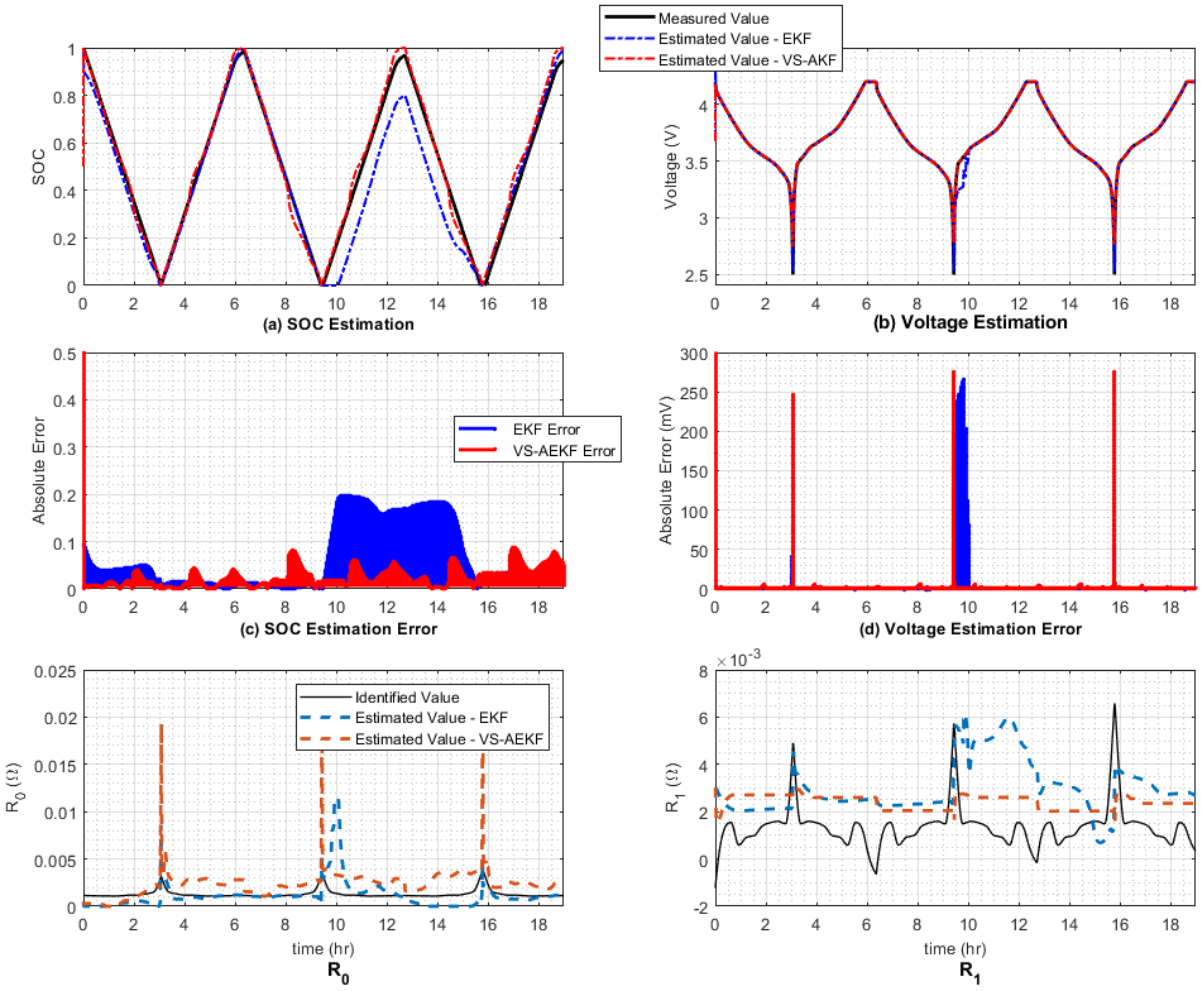

Figure 36. Comparison of estimation results using EKF and VM-AEKF for CC-CV cycle

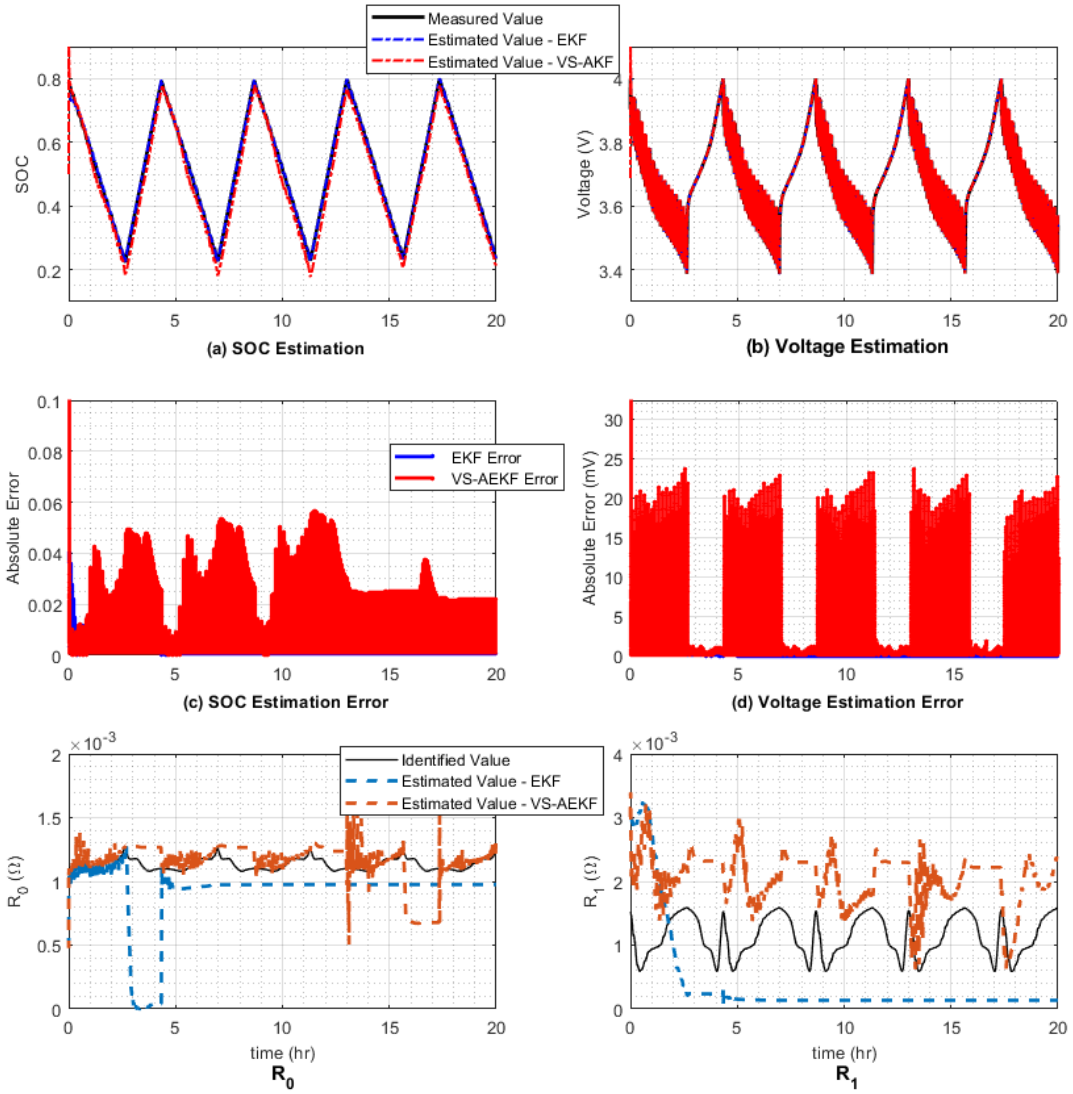

Figure 37. Comparison of estimation results using EKF and VM-AEKF for Driving cycle

3.3 Q_{max} estimation

$Q_{\max}$ is the maximum amount of charge that can be extracted from the anode of the battery in its actual aged state starting from a fully charged state [7]. Updating Eq. (25) as:

$$Q_{\max} = \frac{I_k T_s}{3600\left[SOC_k - SOC_{k+1}\right]} \qquad (62)$$

Thus, by monitoring the net change of charge in the system for a given SOC change, $Q_{\max}$ can be estimated in real-time. The accuracy depends on the integration of current and SOC estimation and can be improved by choosing a suitable sampling window. If the window is too

large, errors build up in the integrator, which leads to biased results. Conversely, if the window is too small, the magnitude of change in SOC is very small, which can cause resolution errors. In addition, if the input current is zero, there is no change in both parameters which further deteriorates the estimation due to accumulation of noises. Thus, the sampling window is set based on every 2% change in SOC $\left(\approx 1.2 \text{ Ah}\right)$ rather than time.

Further improvement to the accuracy of $Q_{\max}$ estimation is performed using an RLS filter with a forgetting factor that reduces the effects of noises by considering multiple samples while the forgetting factor λ controls the contribution of each sample to the covariance matrix.

In fact, $Q_{\max}$ in a cell varies very slowly and its estimation can be updated every 30 minutes which allows RLS sufficient time to reduce the noise errors. The estimation model for RLS is shown below:

$$SOC_k - SOC_{k+1} = \sum I \Delta t \frac{1}{3600 Q_{\max}} \qquad (63)$$

The algorithm for the proposed RLS is summarized in Table 7, where $SOC_k - SOC_{k-1}$ is the measurement vector y_{RLS}, estimated parameter $\hat{\theta}$ is $1/\hat{Q}_{\max}$ and $\sum I\Delta t/3600$ is the matrix φ_{RLS}.

Table 7. Algorithm 4 – Q_{max} RLS estimator

Step 1: Initialization –
Initialize $\hat{\theta}_0^+, P_{0,RLS}^+ \; and \; \lambda$
$for \; k = 1,2,3, \ldots\ldots$
Step 1: Integrate charge accumulated –
$Int\_I = Int\_I + {}^{(Idt)}/_{3600}$
Step 2: Estimate Q_{max} (RLS) –
$if \; Int\_I > 1.2$
$K_{k,RLS} = {}^{P_{k-1,RLS}\varphi_k}/_{\left(\lambda + \varphi_k^T P_{k-1,RLS}\varphi_k\right)}$
$\hat{\theta}_k = \hat{\theta}_{k-1} + K_{k,RLS}\left(y_{k,RLS} - \varphi_k \hat{\theta}_{k-1}\right)$
$P_{k,RLS} = {}^{\left(I - K_{k,RLS}\varphi_k^T\right)P_{k-1,RLS}}/_{\lambda}$
$\hat{Q}_{max} = \frac{1}{\hat{\theta}_k}, \; Int\_I = 0$
$if \; abs\left(\hat{Q}_{max} - \tilde{Q}_{max}\right) > 1 \; \& \; time > 30 \; minutes$
$\tilde{Q}_{max} = \hat{Q}_{max}$
end
end
end

3.4 Combined estimator framework

In the previous chapters, methods for ECM parameter and Q_{max} estimation are provided. The VM-AEKF method for SOC and ECM parameter estimation was validated using various current profiles while Q_{max} was considered as an input. A combined approach for estimating all cell parameters is proposed and then tested under different aging and temperature conditions using various testing schedules.

3.4.1 Design of estimator

The procedure for implementation of the VM-AEKF along with the RLS estimator is summarized in Table 8. A block diagram for the algorithms is depicted in Figure 38**,** where the VM-AEKF is first used to estimate SOC along with ECM parameters, which provides the measurement vector, given as the change in SOC, for the RLS. The RLS then updates $Q_{\max}$ that is one of the inputs for VM-AEKF.

Table 8. Summary of the procedure for Combined VM-AEKF RLS estimator

Step 1: Initialization –
Initialize $\hat{\boldsymbol{x}}_{\boldsymbol{0}}^{+}, P_0^{+}, R, \hat{\theta}_0^{+}, P_{0,RLS}^{+}$ *and* R_{RLS}
$\boldsymbol{for\ k = 1, 2, 3, \ldots\ldots, n}$
Step 2: Variable model framework (Algorithm 3)
Step 3: Time update (Prediction – Algorithm 1)
Step 4: Measurement update (Correction – Algorithm 1)
Step 5: Adaptive noise update (Covariance matching – Algorithm 2)
Step 6: Q_{max} RLS estimator (Algorithm 4)
end

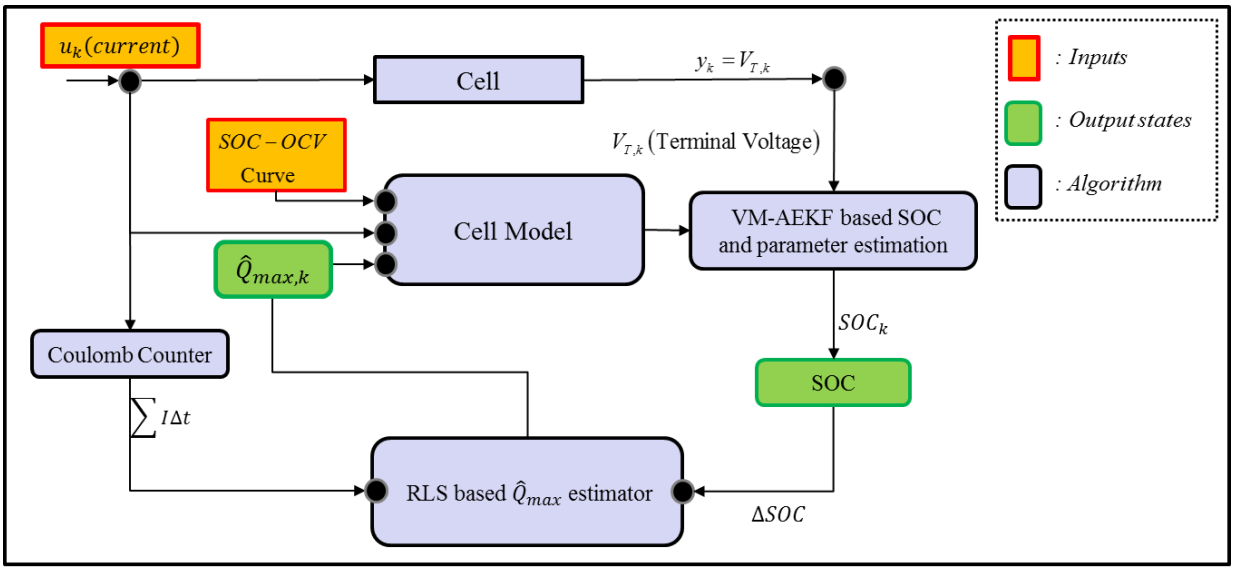

Figure 38. VM-AEKF with RLS filter.

The state and measurement equations for estimation of SOC and parameters is discussed in detail in the previous sections. The setup for the $Q_{\max}$ estimator, as explained in section 3.3, receives the current integration as an input using the Coulomb counter to define φ_{RLS} and the estimated SOC from the VM-AEKF for the measurement y_{RLS}.

The design for the VM-AEKF has been described in the previous chapter and the same initial values are implemented here for validation of the combined estimator algorithm. In addition the error covariance for the RLS is $\hat{P}_{0,RLS}^{+} = E\left[\left(\boldsymbol{\theta_0} - \hat{\boldsymbol{\theta}}_{\boldsymbol{0}}^{+}\right)\left(\boldsymbol{\theta_0} - \hat{\boldsymbol{\theta}}_{\boldsymbol{0}}^{+}\right)^{T}\right]$, where $\theta_0 = 1/Q_{\max}$ and

the forgetting factor is selected as $\lambda = 0.5$ after multiple trials. To test the self-correcting capability of the combined VM-AEKF and RLS estimator, initial capacity is assumed as $\hat{Q}_{\max,0} = 40$ Ah , which gives $\hat{\theta}_0^+ = 1/40$.

3.4.2 Validation and discussion

Performance of the proposed estimation method is validated using multiple offline and online testing profiles at different temperatures and aging conditions. The online testing schedule is devised to evaluate the performance of the estimator in real time, which includes both high excitation and low excitation inputs. The schedule starts with a static capacity test followed by ten 0.5 C CC discharge/charge cycles between 90% ~ 5% SOC, which represents the actual operating range, ten 0.5 C CC discharge and CC-CV charge cycles at the same SOC range, to test the algorithm for repeated CV profiles, and ten in-house driving discharging and CC-CV charging cycles, to replicate the actual driving characteristic. All these tests are performed at a constant temperature of 25^o C until the cell reaches end-of-life (EOL).

3.4.2.1 Evaluation for BOL at different temperatures

Estimation results for the CC-CV profile and the driving profile are plotted in Figure 39 and Figure 40, respectively. The results of the SOC estimation and associated errors for the cycles are plotted in Figure 39 (a), Figure 40 (a), Figure 39 (c) and Figure 40 (c) respectively. SOC estimation errors are relatively high and increase with time, particularly, the maximum errors are 25% for the CC-CV profile, and 6.5% for the driving profile. The high errors for the CC-CV profile is caused by the measured SOC value that decreases with every cycle. Ideally, the value of actual SOC should vary from 0 to 1, while the value of measured SOC reduces further below 1 with every cycle, which can be observed in Figure 39 (e). A few causes are errors accumulated by current integration, reduction in Q_{max} due to continuous cycling and difference in Q_{max} for charging and

discharging. Thus, the VM-AEKF is able to estimate SOC better than the measured SOC and is not affected by sensor noise or capacity variations.

In addition, the voltage estimation results and associated errors are shown in Figure 39 (b) and (d) and Figure 40 (b) and (d) for the respective current profiles. The maximum error for the CC-CV cycles is 55.33 mV at very low SOC (<0.01%) where the parameters varied rapidly, and the root mean square error (RMSE) is 1.08 mV. Low errors are observed for driving cycles with 0.85 mV RMSE and 14.97 mV maximum error, which can be attributed to high excitations produced by the driving cycles and the range of observation, i.e., the cell varies between 80% and 20% SOC and thus errors occurring at low SOC ranges are not present.

The results of Q_{max} estimation are shown in Figure 39 (e) and Figure 40 (e), which includes the true value along with measured value from the static capacity test, noisy measurements that describe the measurement vector y_{RLS} that was calculated using Eq. (63), and the estimated values from the VM-AEKF and RLS estimation. The estimator converges to the true value in less than 5 hours for both cases. The RLS estimation closely follows the noisy measurements due to the low value of $\lambda(=0.5)$. The lower value of λ reduces the contribution of values at previous sample points that makes the filter more sensitive to the fresh samples, which is necessary to keep $Q_{\max}$ updated, but also causes high fluctuations. The effects of these fluctuations were reduced by allowing a suitable window before the value is actually updated, represented by the update points in the figure. Thus, the estimator deviates at the beginning of the driving cycle but the delayed update approach allows the estimator to stabilize and converge to the accurate.

The benefits of high excitation inputs for estimation can be further observed in R_0 estimation from Figure 39 (f) and Figure 40 (f), where the driving cycle based results show much

better convergence and stability as compared to those from the CC-CV cycles. As mentioned before, persistently excited signal is required to accurately estimate and track these parameters.

The proposed RLS based estimator adequately tracks the Q_{max} while the VM-AEKF estimates the other states and parameters, even if incorrect initial values are provided, with results comparable to the traditionally used combination filter [39] or dual filter [16] approach. In addition, the proposed method does not add further states for estimation like in the case of a combination filter approach, which increases the computational effort and sensitivity towards the input excitation, and is simple to implement compared to the dual filter approach which requires complex matrix differentiation for parameter estimation.

The data from offline tests is used to evaluate the performance of the estimator under different temperature conditions. Like the previous case, incorrect initial value of $Q_{\max}$ $\left(\hat{Q}_{\max} = 40 \text{ Ah}\right)$ was applied and the HPPC profile was used. Estimations of Q_{max} and R_0 at different temperatures is shown in Figure 41. The SOC and voltage error statistics are provided in Table 9. Performance of the estimator is consistent with the previous cases where, the Q_{max} estimator corrects the initial errors and converges to the accurate value within 5 hours, while the R_0 estimation is consistent and is able to approximate the true value adequately. However, there is still high deviation in R_0 estimation caused by low excitation during the resting phase. In Table 9, the voltage estimation errors were higher at 10^o C and 45^o C, while the SOC estimation errors were higher at 15^o C and 25^o C. The high voltage errors are attributed to the large deviation of the SOC-OCV curve at these temperatures compared to the SOC-OCV curve at 25^o C, as shown in Figure 11**,** while the high SOC errors are caused by the larger deviation between the initial and the actual Q_{max} value, which is larger for 15^o C and 25^o C compared to those at 10^o C and 45^o C.

Consequently, the proposed estimator was able to accurately estimate the states and parameters of the cell under varying temperature conditions even though incorrect initial values were provided.

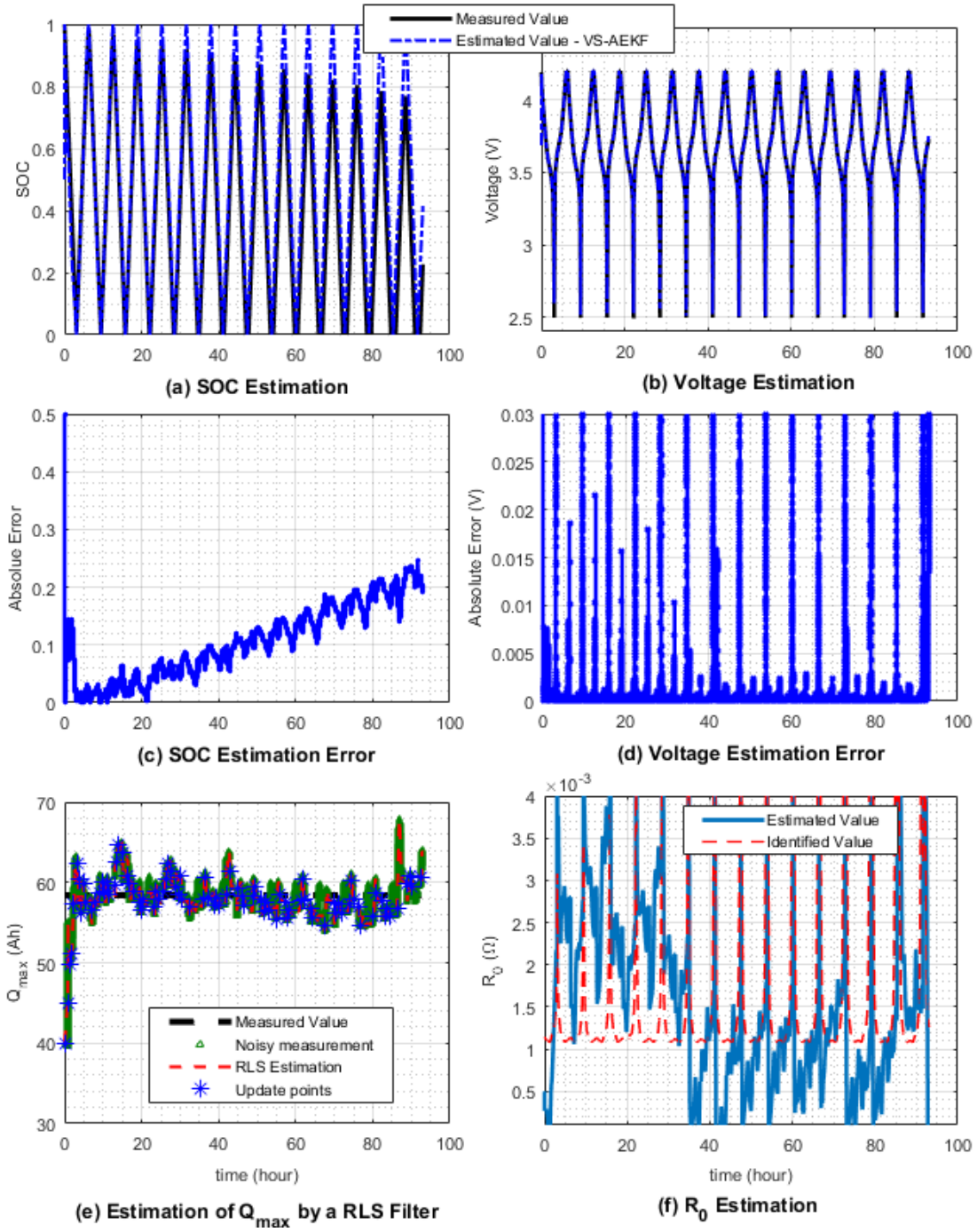

Figure 39. Estimation results using VM-AEKF and RLS estimator with incorrect Q_{max} value for CC-CV cycle.

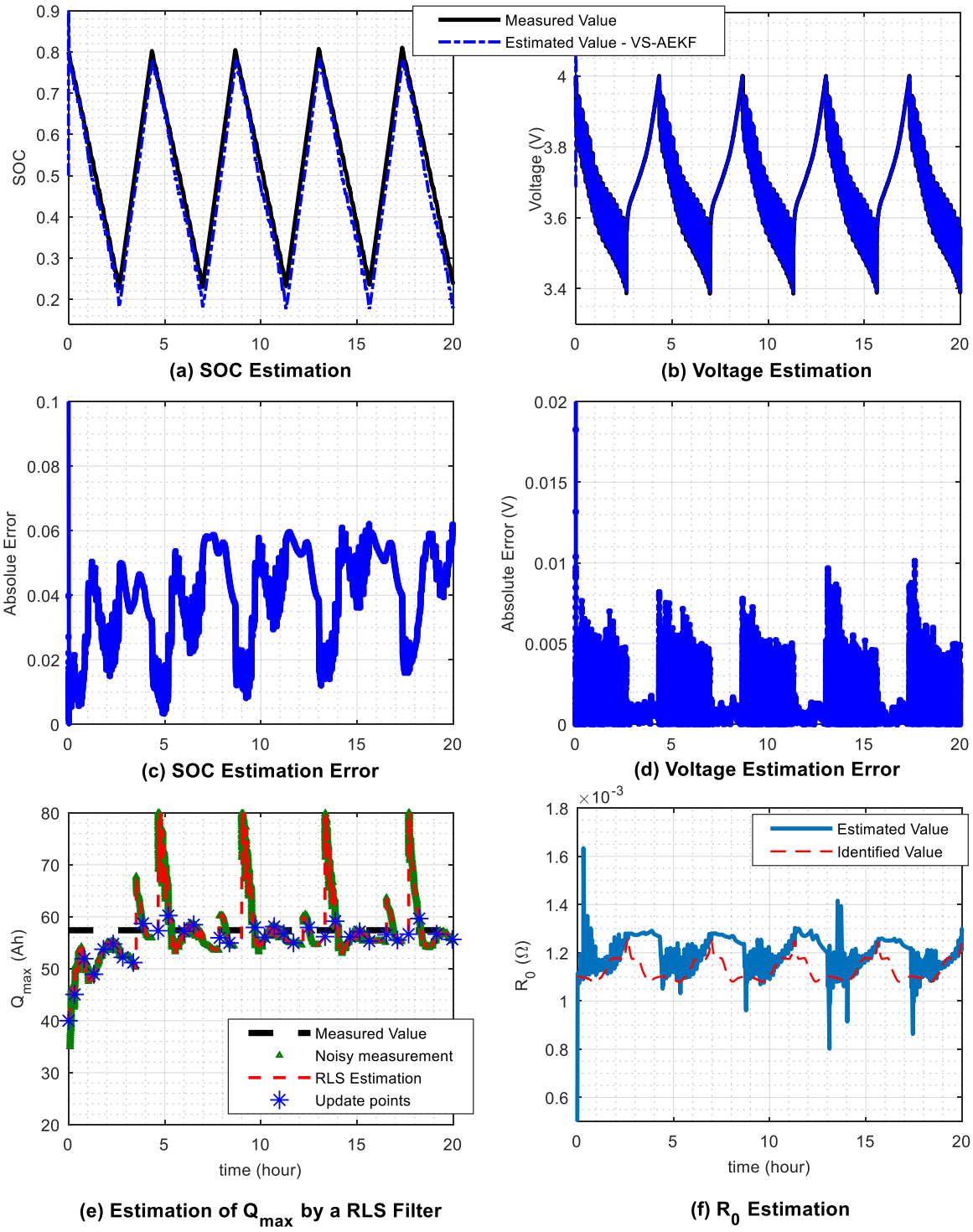

Figure 40. Estimation results using VM-AEKF and RLS estimator with incorrect Q_{max} value for Driving cycle

Table 9. Voltage and SOC estimation error at different temperatures

Temperature (^{0}C)	Voltage Error (mV)		SOC Error (%)	
	Max Error	RMSE	Max Error	RMSE
10	28.12	0.52	3.54	1.74
15	9.64	0.36	6.56	2.99
25	9.84	0.36	5.35	2.44
45	28.36	0.52	3.49	1.39

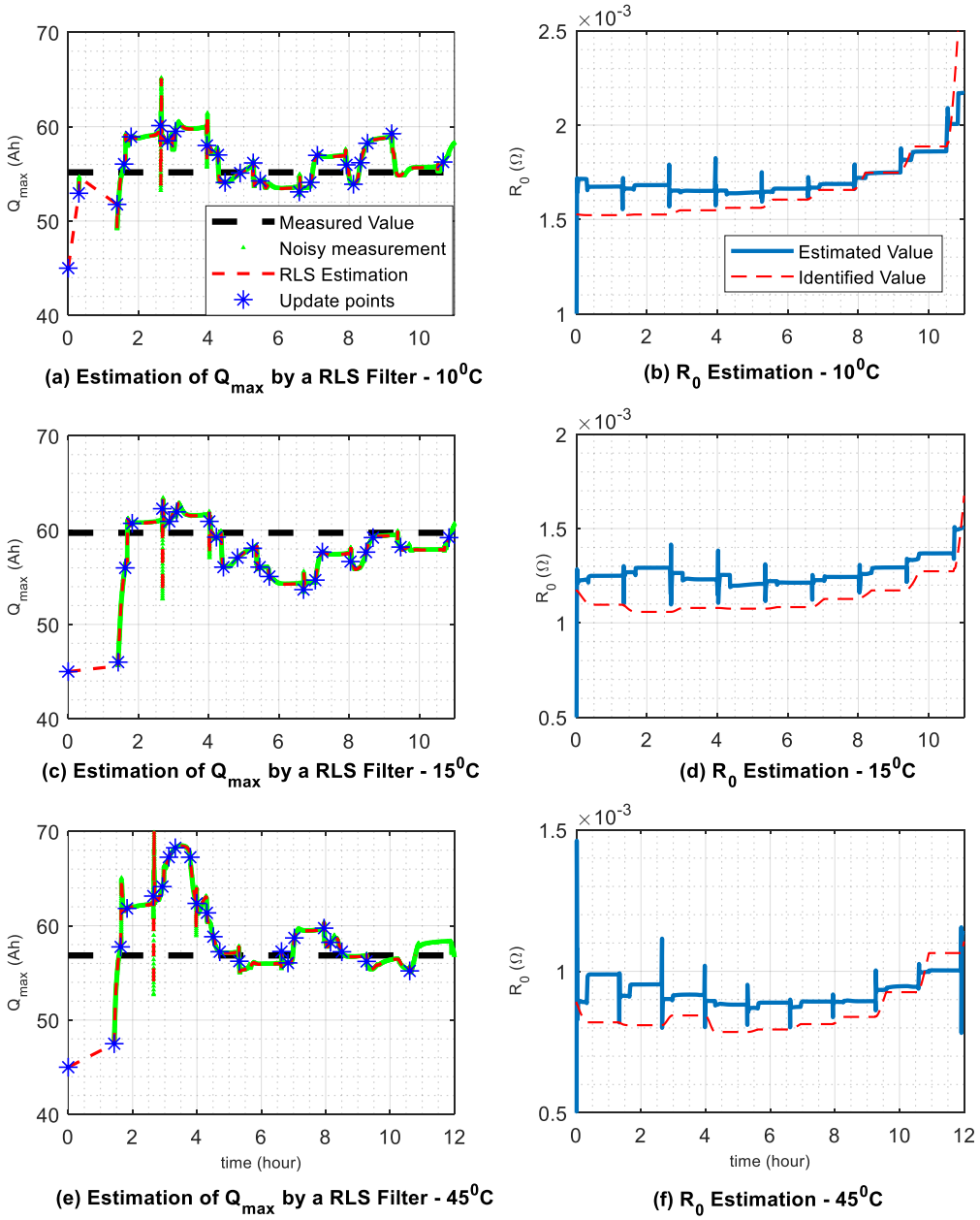

(a) Estimation of Q_{max} by a RLS Filter - 10^0C

(b) R_0 Estimation - 10^0C

(c) Estimation of Q_{max} by a RLS Filter - 15^0C

(d) R_0 Estimation - 15^0C

(e) Estimation of Q_{max} by a RLS Filter - 45^0C

(f) R_0 Estimation - 45^0C

Figure 41. Estimation results at different temperatures.

3.4.2.2 Evaluation for aging conditions

The performance of the proposed estimator is evaluated for the cycle life of the cell, where HPPC data and multiple cycling data are used. The initial conditions were the same as that for the second case. The voltage and SOC estimation error data for the offline test and online tests are provided in Table 10 and Table 11, respectively. The voltage estimation errors are lower for the online tests as the lower SOC ranges (< 5%) is ignored while the SOC estimation errors for both cells are comparable. Estimation results for the online test at the middle of life (40-45 cycle) are shown in Figure 42 and the results are consistent with the previous analysis, with low voltage estimation errors, fast Q_{max} convergence, accurate R_0 estimation and relatively higher SOC errors due to incorrect offline measurement. The estimated value of R_0 is more than the measured value, which is expected as R_0 increases with aging.

Table 10. Voltage and SOC estimation error for Cell 01 under aging using HPPC data

Cycle No.	Voltage Error (mV)		SOC Error (%)	
	Max Error	RMSE	Max Error	RMSE
0	55.33	1.08	5.36	2.27
30	43.67	0.80	5.38	2.28
60	39.03	0.61	5.46	2.35
90	29.07	0.57	6.98	2.76
120	46.43	0.84	6.84	2.89
150	44.32	0.70	6.87	2.96
180	44.51	0.87	13.41	2.97
210	44.98	0.86	7.13	3.09
240	44.14	0.82	7.20	3.08
270	42.36	0.95	7.20	3.06
300	44.70	0.74	7.39	3.06

Table 11. Voltage and SOC estimation error for Cell 02 under aging

Cycle No.	Voltage Error (mV)		SOC Error (%)	
	Max Error	RMSE	Max Error	RMSE
0-10 (CC and CC-CV)	14.97	0.85	6.72	2.39

10-20 (Driving and CC)	10.16	1.19	8.92	5.45
20-30 (CC-CC)	12.79	1.04	5.62	1.86
30-40 (CC and CC-CV)	22.53	1.14	8.73	2.19
40-50 (Driving and CC)	28.03	1.29	13.77	7.73
50-60 (CC-CC)	22.36	1.18	9.03	3.42
60-70 (CC and CC-CV)	18.88	0.99	8.21	2.11
70-80 (Driving and CC)	9.73	1.23	14.64	6.60

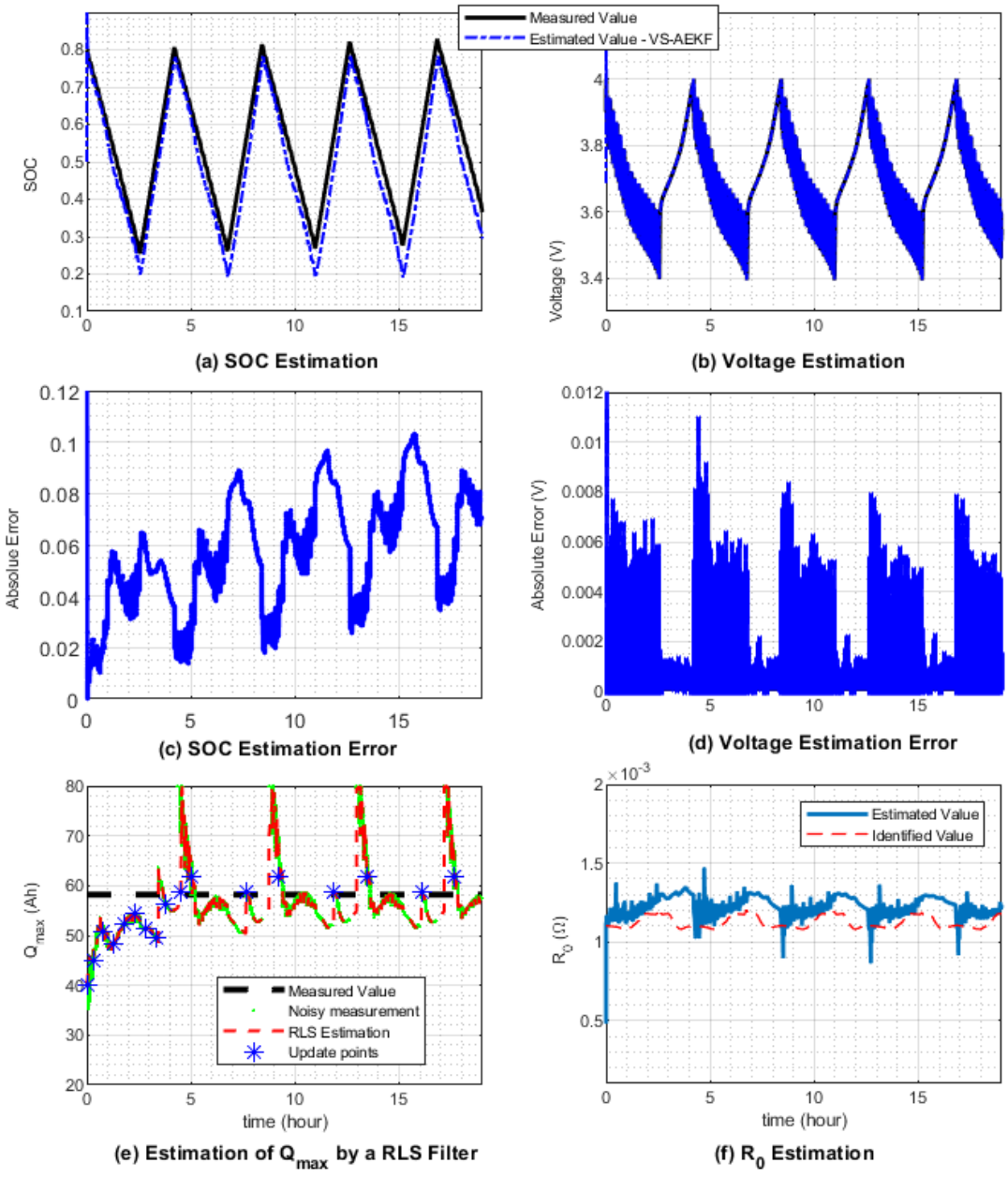

Figure 42. Estimation results using VM-AEKF and RLS estimator with incorrect Q_{max} value for cell 02 after aging (40-45 cycle).

3.5 SOH estimation

SOH is an important criterion to evaluate the long-term degradation of the cell and is defined as a ratio of the present condition of a cell compared with the conditions of a fresh battery. It represents the abilities of a battery to store energy, source and sink high currents, and retain charge over extended periods [7]. These abilities decrease over the battery lifetime due to aging. SOH is defined as 100% for a fresh cell at BOL and 0% at EOL when one of these two capacities decreases to a minimum value. The cell may still be used when the SOH is 0%, because it is merely an indicator that reflects the battery has already reached to its predefined criteria for replacement. The definitions for the different SOH, SOH_P and SOH_Q, are provided in chapter 1.

The Maximum Capacity of a cell gradually fades during its lifetime and is defined as capacity fade or SOH_Q. When the capacity is not enough for its normal use, the cell should be replaced. Estimation of Q_{max} is a very challenging task because it is not related to anything directly. A method for estimating Q_{max} has been described in this thesis. SOH_Q is defined as:

$$SOH_Q = \frac{Q_{\max,k}}{Q_{\max,BOL}} \times 100 \qquad (64)$$

The peak power capability describes the available power at any time instant and is defined as the maximum power a cell can provide. The peak power gradually fades during the cell lifetime and the power available describes the SOH_P of a cell as provided in Eq. (8), where $P_{\text{available}}$ and P_{nominal} are the instantaneous power available at time step k and the power available at BOL respectively. As output power is related to the internal resistance as $P = V^2 / R_{\text{int}}$, SOH_P can be represented with resistance instead of power terms as:

$$SOH_P\,(\%) = \frac{P_{\text{available}}}{P_{\text{nominal}}} \times 100 = \frac{R_{\text{nominal}}}{R_{\text{available}}} \times 100 \qquad (65)$$

The values of these cell parameters have been estimated in the previous section and the results are shown in Figure 43 (a) and (b) where the proposed estimator was able to adequately estimate these cell parameters. Based on Eq. (64) and (65), the results for SOH_P and SOH_Q are shown in Figure 43 (c) and (d) while the respective estimation errors are shown in Figure 43 (e) and (f). The RMSE are 3.95% and 0.42% for SOH_P and SOH_Q, while the peak errors are 6.74% and 0.88% respectively. The high errors in SOH_P are caused by the HPPC input used for parameter estimation that has low excitation input signals, which affects the accuracy of ECM parameter and in turn accuracy of SOH_P. In addition, the value of parameter R_0 is very small (<0.002) and minor errors in estimation are exaggerated due to the division of two small numbers in Eq. (65). These errors can be prevented by using R_0 as a direct indicator of SOH_p instead of using the description in Eq. (65).

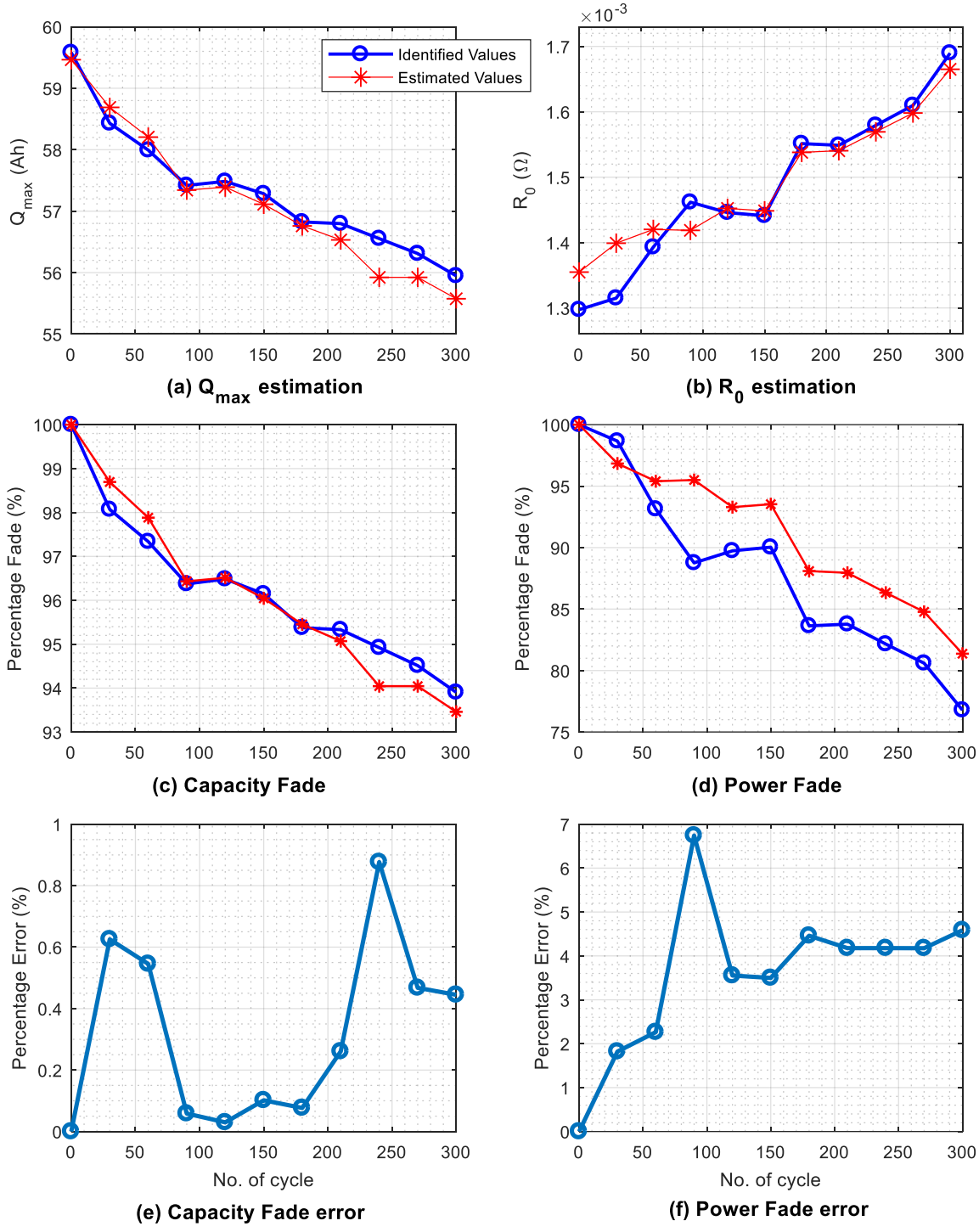

Figure 43. Estimation results for different aging conditions.

4. Conclusion and future work

In this thesis, a new approach that facilitates simultaneous estimation of SOC and SOH in real time is proposed and validated. The estimation of SOC and ECM parameters is performed by employing a VM-AEKF based on a second-order ECM, which assure a better accuracy and robustness even with incorrect initial values and noises at measurements. An RLS filter with a forgetting factor is used to estimate $Q_{\max}$ in a closed loop framework that facilitates self-correcting and tracking the $Q_{\max}$ of the cell over extended periods while compensating for effects by temperature and aging.

The performance of the proposed estimator is evaluated using multiple profiles, particularly low excitation profiles to examine the ability of the VM framework to reduce the errors in state estimation and ensure estimator stability. The RMSE of the estimated voltage is less than 1.3 mV for all aging and temperature conditions, while the peak error is less than 56 mV for low excitation profiles and less than 30 mV for high excitation profiles. In addition, the SOC estimation is capable of accommodating the effects of change in $Q_{\max}$, while cycling and filtering out the errors caused by noises present in current measurements. Finally, the estimated cell parameters are successfully used to estimate SOH_P and SOH_Q, which accuracy is 3.95% and 0.42% RMSE, respectively. The summary of contributions is as follows:

1. Literature review of the current methods for SOC and SOH estimation.
2. Analysis of the effects of aging and temperature on cell parameters. Method for offline estimation of the various cell parameters is briefly described and a brief analysis of the results is provided.
3. Analysis of first and second order ECMs using simulated and experimental data is performed. The second order ECM is preferred due to its better dynamic response.

4. Implementation and analysis of EKF for parameter and state estimation. The EKF is able to estimate the states for single cycle profiles but is not suitable for estimation over long term as shown in results for the multiple cycle, with particularly poor performance for low excitation profiles.
5. Improvements to traditional EKF by using "adaptive noise update" and a "variable model framework". The proposed VM-AEKF method is tested using single and multiple cycles at BOL and the results are compared with that of a traditional EKF. The improvements in state estimation results verify the benefits of the VM-AEKF, especially for inputs with low persistency of excitation.
6. Q_{max} is estimated and incorporated into the VM-AEKF in a closed loop framework. The combined estimator is validated for multiple cycles and for different aging and temperatures (10^0 C to 45^0 C) conditions.

In addition, a method to evaluate the SOH of the NMC/C cell is proposed considering both Power fade, SOH_P and Capacity fade, SOH_Q. Power fade requires the internal resistance R_0 while the capacity fade requires the maximum capacity Q_{max} as input. SOH of the cell is evaluated using offline data at 25^o C and the results are compared with offline identified values.

4.1 Future work

This research provides a comprehensive solution for long-term state estimation under dynamic operating conditions which is readily applicable for real-time applications. Future work includes:

1. Evaluation of proposed approach at low temperatures, i.e. subzero temperatures.
2. Improvements to the underlying estimator algorithms by implementing higher order estimators, like second order EKF and particle filter.

Reference

[1] "Types of Lithium-ion Batteries – Battery University." [Online]. Available: https://batteryuniversity.com/learn/article/types_of_lithium_ion. [Accessed: 20-Feb-2019].

[2] "Nickel-Rich Layered Lithium Transition-Metal Oxide for High-Energy Lithium-Ion Batteries - Liu - 2015 - Angewandte Chemie International Edition - Wiley Online Library." [Online]. Available: https://onlinelibrary.wiley.com/doi/epdf/10.1002/anie.201409262. [Accessed: 20-Feb-2019].

[3] T. R. Tanim, C. D. Rahn, and C.-Y. Wang, "State of charge estimation of a lithium ion cell based on a temperature dependent and electrolyte enhanced single particle model," *Energy*, vol. 80, pp. 731–739, Feb. 2015.

[4] A. Farmann, W. Waag, A. Marongiu, and D. U. Sauer, "Critical review of on-board capacity estimation techniques for lithium-ion batteries in electric and hybrid electric vehicles," *Journal of Power Sources*, vol. 281, pp. 114–130, May 2015.

[5] H. Chaoui, N. Golbon, I. Hmouz, R. Souissi, and S. Tahar, "Lyapunov-Based Adaptive State of Charge and State of Health Estimation for Lithium-Ion Batteries," *IEEE Transactions on Industrial Electronics*, vol. 62, no. 3, pp. 1610–1618, Mar. 2015.

[6] "Battery Test Manual For Electric Vehicles, Revision 3 (Technical Report) | OSTI.GOV." [Online]. Available: https://www.osti.gov/biblio/1186745. [Accessed: 20-Feb-2019].

[7] W. Waag, C. Fleischer, and D. U. Sauer, "Critical review of the methods for monitoring of lithium-ion batteries in electric and hybrid vehicles," *Journal of Power Sources*, vol. 258, pp. 321–339, Jul. 2014.

[8] Y. Zhang, C.-Y. Wang, and X. Tang, "Cycling degradation of an automotive LiFePO4 lithium-ion battery," *Journal of Power Sources*, vol. 196, no. 3, pp. 1513–1520, Feb. 2011.

[9] D. P. Abraham *et al.*, "Diagnosis of power fade mechanisms in high-power lithium-ion cells," *Journal of Power Sources*, vol. 119–121, pp. 511–516, Jun. 2003.

[10] R. Xiong, H. He, F. Sun, and K. Zhao, "Evaluation on State of Charge Estimation of Batteries With Adaptive Extended Kalman Filter by Experiment Approach," *IEEE Transactions on Vehicular Technology*, vol. 62, no. 1, pp. 108–117, Jan. 2013.

[11] M. U. Cuma and T. Koroglu, "A comprehensive review on estimation strategies used in hybrid and battery electric vehicles," *Renewable and Sustainable Energy Reviews*, vol. 42, pp. 517–531, Feb. 2015.

[12] R. Mingant *et al.*, "EIS Measurements for Determining the SoC and SoH of Li-Ion Batteries," *ECS Trans.*, vol. 33, no. 39, pp. 41–53, Apr. 2011.

[13] C. Fleischer, W. Waag, H.-M. Heyn, and D. U. Sauer, "On-line adaptive battery impedance parameter and state estimation considering physical principles in reduced order equivalent circuit battery models," *Journal of Power Sources*, vol. 260, pp. 276–291, Aug. 2014.

[14] A. Zenati, P. Desprez, and H. Razik, "Estimation of the SOC and the SOH of li-ion batteries, by combining impedance measurements with the fuzzy logic inference," in *IECON 2010 - 36th Annual Conference on IEEE Industrial Electronics Society*, 2010, pp. 1773–1778.

[15] D. Andre, C. Appel, T. Soczka-Guth, and D. U. Sauer, "Advanced mathematical methods of SOC and SOH estimation for lithium-ion batteries," *Journal of Power Sources*, vol. 224, pp. 20–27, Feb. 2013.

[16] C. Hu, B. D. Youn, and J. Chung, "A multiscale framework with extended Kalman filter for lithium-ion battery SOC and capacity estimation," *Applied Energy*, vol. 92, pp. 694–704, Apr. 2012.

[17] Xueyan Li and Song-Yul Choe, “State-of-charge (SOC) estimation based on a reduced order electrochemical thermal model and extended Kalman filter,” in *2013 American Control Conference*, Washington, DC, 2013, pp. 1100–1105.
[18] R. Ishizaki, L. Lin, and M. Fukui, “An Accurate SOC Estimation Method for Lithium-ion Batteries which Considers Thermal Variation,” *Electrochemistry*, vol. 83, no. 10, pp. 852–854, 2015.
[19] H. He, R. Xiong, and J. Fan, “Evaluation of Lithium-Ion Battery Equivalent Circuit Models for State of Charge Estimation by an Experimental Approach,” *Energies*, vol. 4, no. 4, pp. 582–598, Apr. 2011.
[20] G. Dong, X. Zhang, C. Zhang, and Z. Chen, “A method for state of energy estimation of lithium-ion batteries based on neural network model,” *Energy*, vol. 90, pp. 879–888, Oct. 2015.
[21] H. Rahimi-Eichi, F. Baronti, and M. Chow, “Online Adaptive Parameter Identification and State-of-Charge Coestimation for Lithium-Polymer Battery Cells,” *IEEE Transactions on Industrial Electronics*, vol. 61, no. 4, pp. 2053–2061, Apr. 2014.
[22] X. Tang, X. Mao, J. Lin, and B. Koch, “Li-ion battery parameter estimation for state of charge,” in *Proceedings of the 2011 American Control Conference*, 2011, pp. 941–946.
[23] B. Fridholm, T. Wik, and M. Nilsson, “Robust recursive impedance estimation for automotive lithium-ion batteries,” *Journal of Power Sources*, vol. 304, pp. 33–41, Feb. 2016.
[24] B. Xia, X. Zhao, R. de Callafon, H. Garnier, T. Nguyen, and C. Mi, “Accurate Lithium-ion battery parameter estimation with continuous-time system identification methods,” *Applied Energy*, vol. 179, pp. 426–436, Oct. 2016.
[25] G. L. Plett, “Sigma-point Kalman filtering for battery management systems of LiPB-based HEV battery packs,” *Journal of Power Sources*, vol. 161, no. 2, pp. 1369–1384, Oct. 2006.
[26] A. Baba *et al.*, “Simultaneous Estimation of the SOC and Parameters of Batteries for HEV/EV,” presented at the SAE 2016 World Congress and Exhibition, 2016, pp. 2016-01–1195.
[27] M. Berecibar, I. Gandiaga, I. Villarreal, N. Omar, J. Van Mierlo, and P. Van den Bossche, “Critical review of state of health estimation methods of Li-ion batteries for real applications,” *Renewable and Sustainable Energy Reviews*, vol. 56, pp. 572–587, Apr. 2016.
[28] L. Ungurean, G. Cârstoiu, M. V. Micea, and V. Groza, “Battery state of health estimation: a structured review of models, methods and commercial devices,” *International Journal of Energy Research*, vol. 41, no. 2, pp. 151–181, 2017.
[29] M. Galeotti, L. Cinà, C. Giammanco, S. Cordiner, and A. Di Carlo, “Performance analysis and SOH (state of health) evaluation of lithium polymer batteries through electrochemical impedance spectroscopy,” *Energy*, vol. 89, pp. 678–686, Sep. 2015.
[30] F. Sun, R. Xiong, H. He, W. Li, and J. E. E. Aussems, “Model-based dynamic multi-parameter method for peak power estimation of lithium–ion batteries,” *Applied Energy*, vol. 96, pp. 378–386, Aug. 2012.
[31] Z. Guo, X. Qiu, G. Hou, B. Y. Liaw, and C. Zhang, “State of health estimation for lithium ion batteries based on charging curves,” *Journal of Power Sources*, vol. 249, pp. 457–462, Mar. 2014.
[32] H. Lin, T. Liang, and S. Chen, “Estimation of Battery State of Health Using Probabilistic Neural Network,” *IEEE Transactions on Industrial Informatics*, vol. 9, no. 2, pp. 679–685, May 2013.

[33] P. Singh, R. Vinjamuri, X. Wang, and D. Reisner, "Fuzzy logic modeling of EIS measurements on lithium-ion batteries," *Electrochimica Acta*, vol. 51, no. 8–9, pp. 1673–1679, Jan. 2006.
[34] G. You, S. Park, and D. Oh, "Real-time state-of-health estimation for electric vehicle batteries: A data-driven approach," *Applied Energy*, vol. 176, pp. 92–103, Aug. 2016.
[35] G. L. Plett, "Extended Kalman filtering for battery management systems of LiPB-based HEV battery packs," *Journal of Power Sources*, vol. 134, no. 2, pp. 262–276, Aug. 2004.
[36] G. L. Plett, "Extended Kalman filtering for battery management systems of LiPB-based HEV battery packs," *Journal of Power Sources*, vol. 134, no. 2, pp. 277–292, Aug. 2004.
[37] Y. Zou, X. Hu, H. Ma, and S. E. Li, "Combined State of Charge and State of Health estimation over lithium-ion battery cell cycle lifespan for electric vehicles," *Journal of Power Sources*, vol. 273, pp. 793–803, Jan. 2015.
[38] A. E. Mejdoubi, A. Oukaour, H. Chaoui, H. Gualous, J. Sabor, and Y. Slamani, "State-of-Charge and State-of-Health Lithium-Ion Batteries' Diagnosis According to Surface Temperature Variation," *IEEE Transactions on Industrial Electronics*, vol. 63, no. 4, pp. 2391–2402, Apr. 2016.
[39] Y. Li, C. Wang, and J. Gong, "A combination Kalman filter approach for State of Charge estimation of lithium-ion battery considering model uncertainty," *Energy*, vol. 109, pp. 933–946, Aug. 2016.
[40] H. He, R. Xiong, X. Zhang, F. Sun, and J. Fan, "State-of-Charge Estimation of the Lithium-Ion Battery Using an Adaptive Extended Kalman Filter Based on an Improved Thevenin Model," *IEEE Transactions on Vehicular Technology*, vol. 60, no. 4, pp. 1461–1469, May 2011.
[41] Q. Wang, Y. Jiang, and Y. Lu, "State of Health Estimation for Lithium-ion Battery Based on D-UKF," *International Journal of Hybrid Information Technology*, vol. 8, no. 7, pp. 55–70, Jul. 2015.
[42] L. Lu, X. Han, J. Li, J. Hua, and M. Ouyang, "A review on the key issues for lithium-ion battery management in electric vehicles," *Journal of Power Sources*, vol. 226, pp. 272–288, Mar. 2013.
[43] C. Zhang, C. Zhang, and S. M. Sharkh, "Estimation of Real-Time Peak Power Capability of a Traction Battery Pack Used in an HEV," in *2010 Asia-Pacific Power and Energy Engineering Conference*, 2010, pp. 1–6.
[44] X. Hu, S. Li, and H. Peng, "A comparative study of equivalent circuit models for Li-ion batteries," *Journal of Power Sources*, vol. 198, pp. 359–367, Jan. 2012.
[45] J. Jaguemont, L. Boulon, and Y. Dubé, "A comprehensive review of lithium-ion batteries used in hybrid and electric vehicles at cold temperatures," *Applied Energy*, vol. 164, pp. 99–114, Feb. 2016.
[46] A. Fotouhi, D. J. Auger, K. Propp, S. Longo, and M. Wild, "A review on electric vehicle battery modelling: From Lithium-ion toward Lithium–Sulphur," *Renewable and Sustainable Energy Reviews*, vol. 56, pp. 1008–1021, Apr. 2016.
[47] J. Marcicki, M. Canova, A. T. Conlisk, and G. Rizzoni, "Design and parametrization analysis of a reduced-order electrochemical model of graphite/LiFePO4 cells for SOC/SOH estimation," *Journal of Power Sources*, vol. 237, pp. 310–324, Sep. 2013.
[48] S. E. Li, B. Wang, H. Peng, and X. Hu, "An electrochemistry-based impedance model for lithium-ion batteries," *Journal of Power Sources*, vol. 258, pp. 9–18, Jul. 2014.

[49] J. Cannarella and C. B. Arnold, “State of health and charge measurements in lithium-ion batteries using mechanical stress,” *Journal of Power Sources*, vol. 269, pp. 7–14, Dec. 2014.
[50] H.-G. Schweiger *et al.*, “Comparison of Several Methods for Determining the Internal Resistance of Lithium Ion Cells,” *Sensors*, vol. 10, no. 6, pp. 5604–5625, Jun. 2010.
[51] “Study on the correlation between state of charge and coulombic efficiency for commercial lithium ion batteries | Elsevier Enhanced Reader.” [Online]. Available: https://reader.elsevier.com/reader/sd/pii/S037877531500835 6?token=A5258512CF9CE07C450ECA4CC5BBE1142F792CCAC2F0F076D6A79C0DA77D08522F6434665E599894B2FF26D632684464. [Accessed: 25-Jun-2019].
[52] J. Gomez, R. Nelson, E. E. Kalu, M. H. Weatherspoon, and J. P. Zheng, “Equivalent circuit model parameters of a high-power Li-ion battery: Thermal and state of charge effects,” *Journal of Power Sources*, vol. 196, no. 10, pp. 4826–4831, May 2011.
[53] B. Pattipati, C. Sankavaram, and K. Pattipati, “System Identification and Estimation Framework for Pivotal Automotive Battery Management System Characteristics,” *IEEE Transactions on Systems, Man, and Cybernetics, Part C (Applications and Reviews)*, vol. 41, no. 6, pp. 869–884, Nov. 2011.
[54] A. Rahmoun and H. Biechl, “Parameters Identification of Equivalent Circuit Diagrams for Li-Ion Batteries,” p. 5.
[55] “A model-based adaptive state of charge estimator for a lithium-ion battery using an improved adaptive particle filter | Elsevier Enhanced Reader.” [Online]. Available: https://reader.elsevier.com/reader/sd/pii/S0306261916319171?token=E5AD67AE1CC36FCBD783B3CDAF5D3E0BEDF46DD0D0DEB9552447F14990E2710358272C82BD0C54864048CBFFFE42891E. [Accessed: 05-Jul-2019].
[56] “A new model for State-of-Charge (SOC) estimation for high-power Li-ion batteries | Elsevier Enhanced Reader.” [Online]. Available: https://reader.elsevier.com/reader/sd/pii/S0306261912006058?token=4B826A2B4D692EEC4D831E7F189BAE53FF1EAE8BB7044CD527627E548E22C2B8EDE200CB561B2EA3F33836FDEB95CE87. [Accessed: 05-Jul-2019].
[57] S. Akhlaghi, N. Zhou, and Z. Huang, “Adaptive adjustment of noise covariance in Kalman filter for dynamic state estimation,” in *2017 IEEE Power & Energy Society General Meeting*, Chicago, IL, 2017, pp. 1–5.
[58] B. D. O. Anderson, “Adaptive systems, lack of persistency of excitation and bursting phenomena,” *Automatica*, vol. 21, no. 3, pp. 247–258, May 1985.
[59] N. Shimkin and A. Feuer, “Persistency of excitation in continuous-time systems,” *Systems & Control Letters*, vol. 9, no. 3, pp. 225–233, Sep. 1987.
[60] J. C. Willems, P. Rapisarda, I. Markovsky, and B. L. M. De Moor, “A note on persistency of excitation,” *Systems & Control Letters*, vol. 54, no. 4, pp. 325–329, Apr. 2005.
[61] S. T. Glad and L. Ljung, “Model structure identifiability and persistence of excitation,” in *29th IEEE Conference on Decision and Control*, 1990, pp. 3236–3240 vol.6.
[62] S. M. M. Alavi, A. Mahdi, P. E. Jacob, S. J. Payne, and D. A. Howey, “Structural Identifiability Analysis of Fractional Order Models with Applications in Battery Systems,” *arXiv:1511.01402 [math]*, Nov. 2015.
[63] I. Mareels, “Sufficiency of excitation,” *Systems & Control Letters*, vol. 5, no. 3, pp. 159–163, Dec. 1984.
[64] B. D. O. ANDERSONt and C. R. Johnson, “Exponential Convergence of Adaptive Identification and Control Algorithms,” p. 13.

[65] R. Bellman and K. J. Åström, “On structural identifiability,” *Mathematical Biosciences*, vol. 7, no. 3, pp. 329–339, Apr. 1970.
[66] H. Guo, H. Chen, F. Xu, F. Wang, and G. Lu, “Implementation of EKF for Vehicle Velocities Estimation on FPGA,” *IEEE Transactions on Industrial Electronics*, vol. 60, no. 9, pp. 3823–3835, Sep. 2013.

Appendix 1: Testing profiles

1. Static capacity test: this test is used to measure the device capacity in ampere-hours at a C/3 constant current discharge rate corresponding to the rated capacity. Discharge begins following a default rest from a fully-charged state to max voltage (V_{max}) and is terminated on a manufacturer-specified discharge voltage limit (V_{min}), followed by a default rest at open-circuit voltage. The input current profile and output measured voltage are shown in Figure 44.

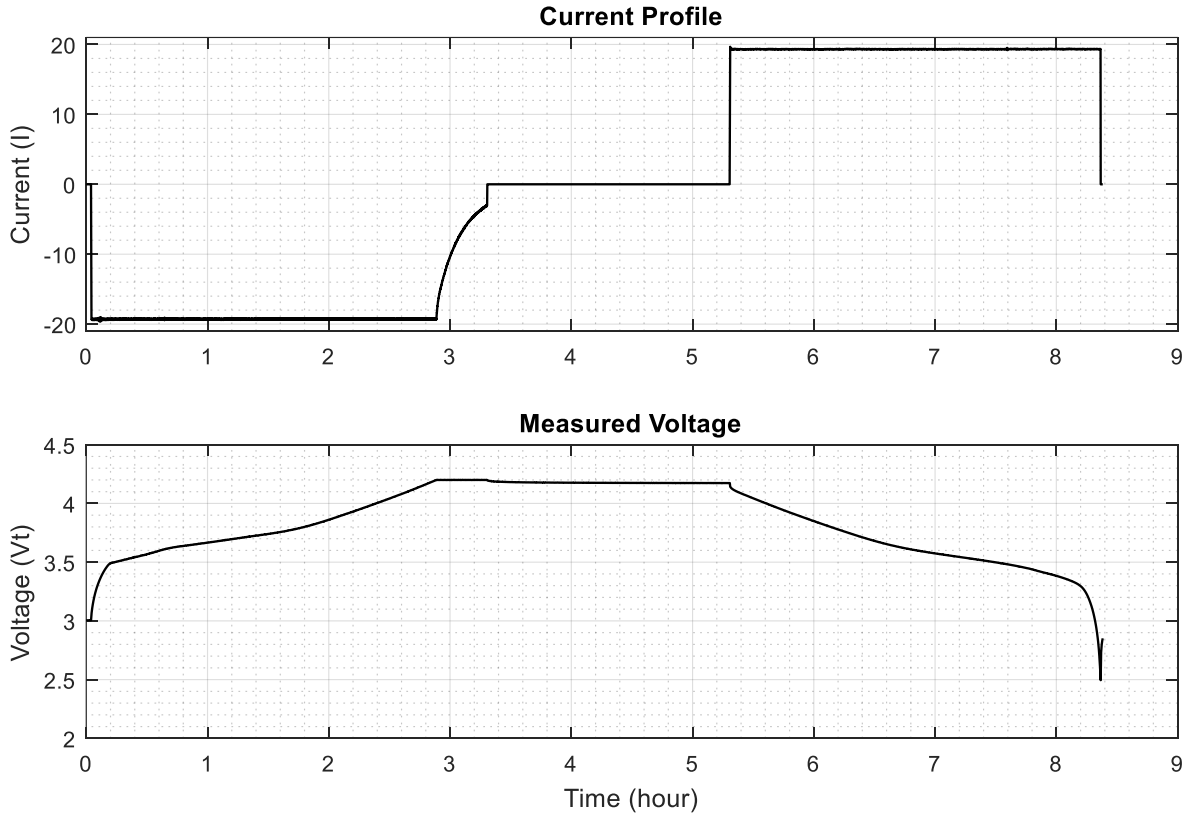

Figure 44. Static capacity test profile

2. HPPC test: The objective of this test is to determine the 30-second discharge-pulse and the 10-second regen-pulse power capabilities at each 10% decrement relative to the BOL operating capacity for the EV Targets (e.g., for a 2 Ah cell, power capabilities are assessed

at 0.2 Ah increments between V_{max} and V_{min}). The current profile with a magnified view of the pulse and the output voltage response is shown in Figure 45.

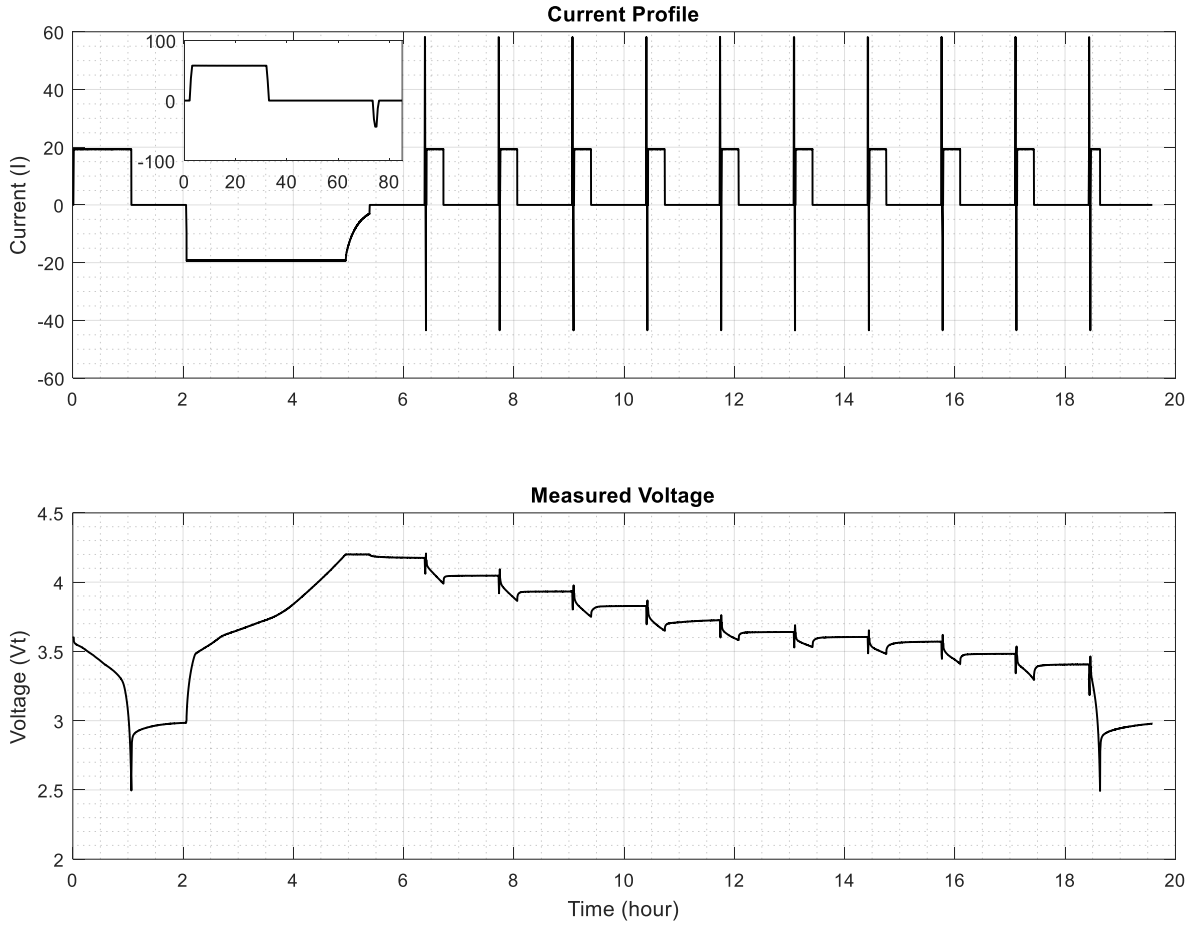

Figure 45. HPPC test

3. DST: The objective of this test profile is to demonstrate lifespan in a charge depleting mode when subjected to energy use levels and patterns appropriate to the targets. Each profile is a series of constant power discharge/charge steps with a total duration of 360 seconds. The DST profile is shown in Figure 46 where the cell was first charged to V_{max} using the same method as that for the static capacity test.

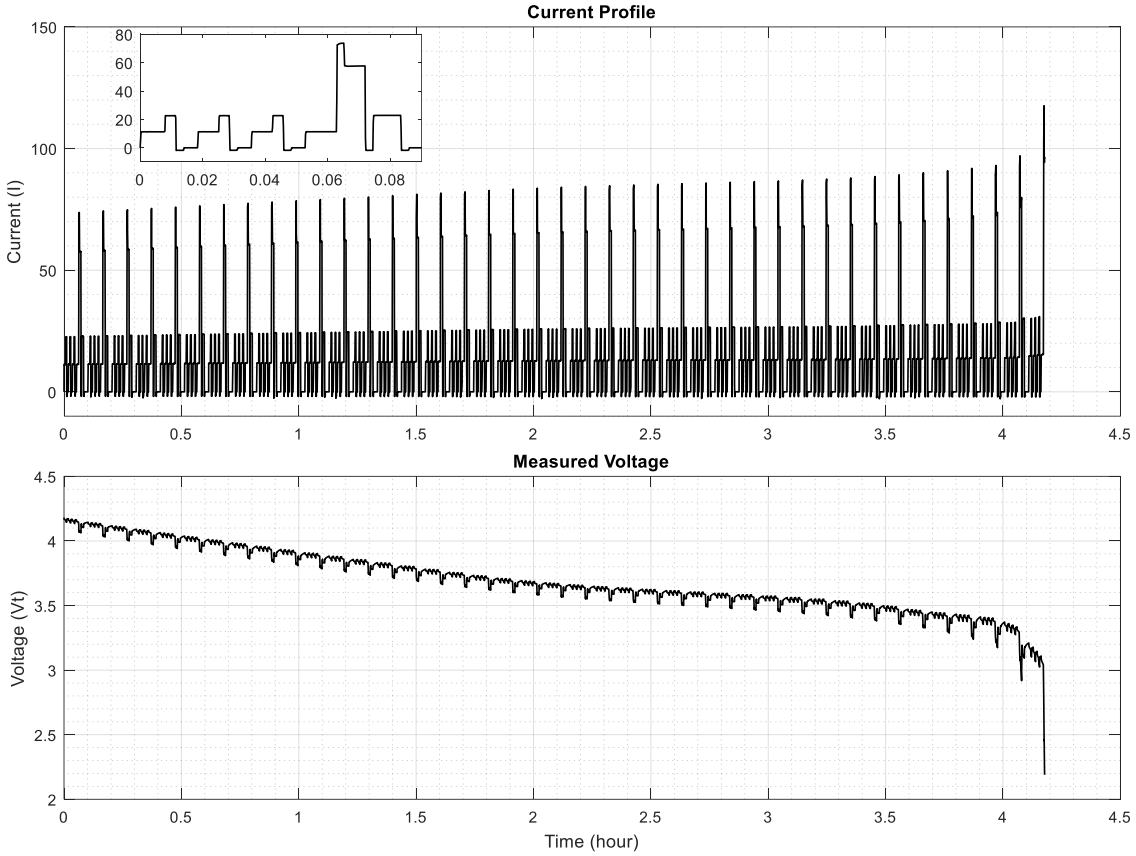

Figure 46. DST profile

4. Driving cycle: The driving cycle is specially designed to replicate the real-time conditions for the cell where it is operated in a charge sustaining mode and cycled between 0.8 and 0.2 SOC. The cell is charged to V_{max} before the test using the same method as for the static capacity test. It is then discharged using the driving profile multiple times and then charged using a CC profile between required SOC range. The voltage and current profiles for two driving cycles along with a single driving profile is shown in Figure 47.

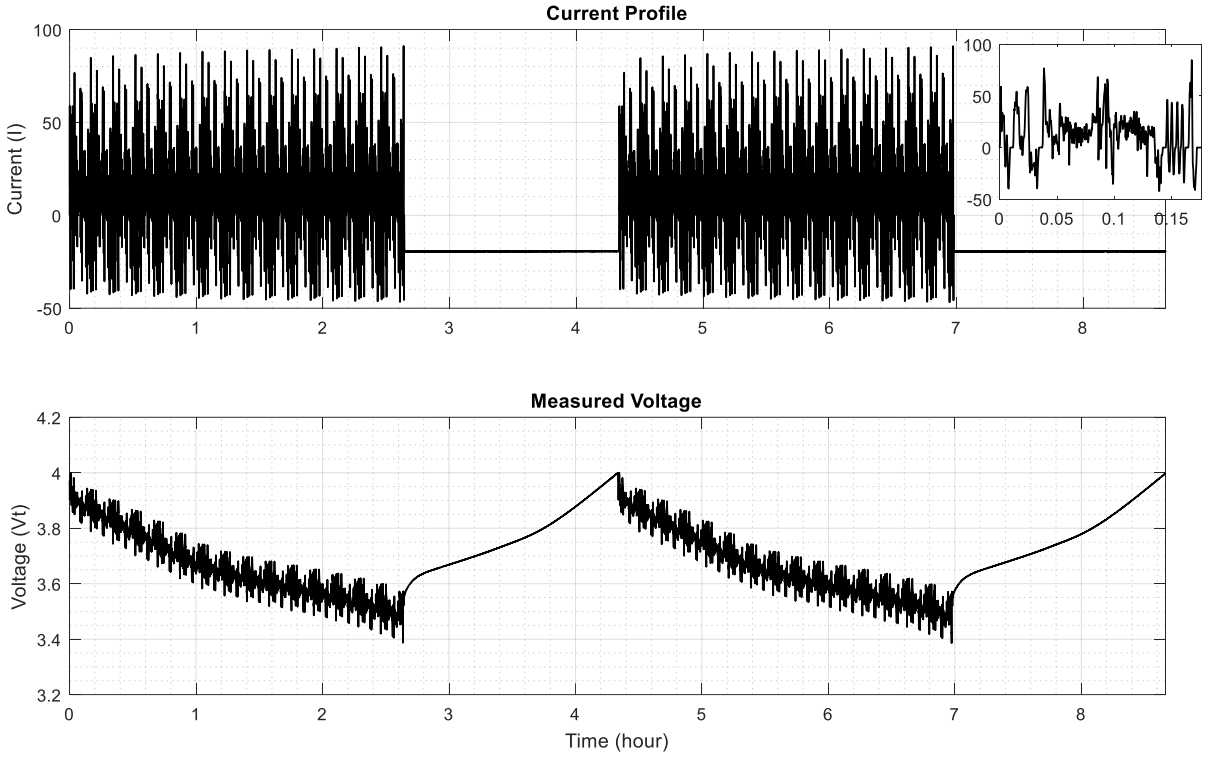

Figure 47. Driving Cycle

5. CC-CV cycle: The CC-CV cycles are implemented to age the cell. The cell is charged to V_{max} before the test using the same method as for the static capacity test. The cell is discharged to V_{min} using CC discharge followed by a CC charge profile till V_{max}. The voltage is then maintained constant (CV mode) by reducing the current until it reaches zero with a ten second rest between the charging and discharging phases. The voltage and current profiles for two CC-CV cycles along with a single driving profile is shown in Figure 48.

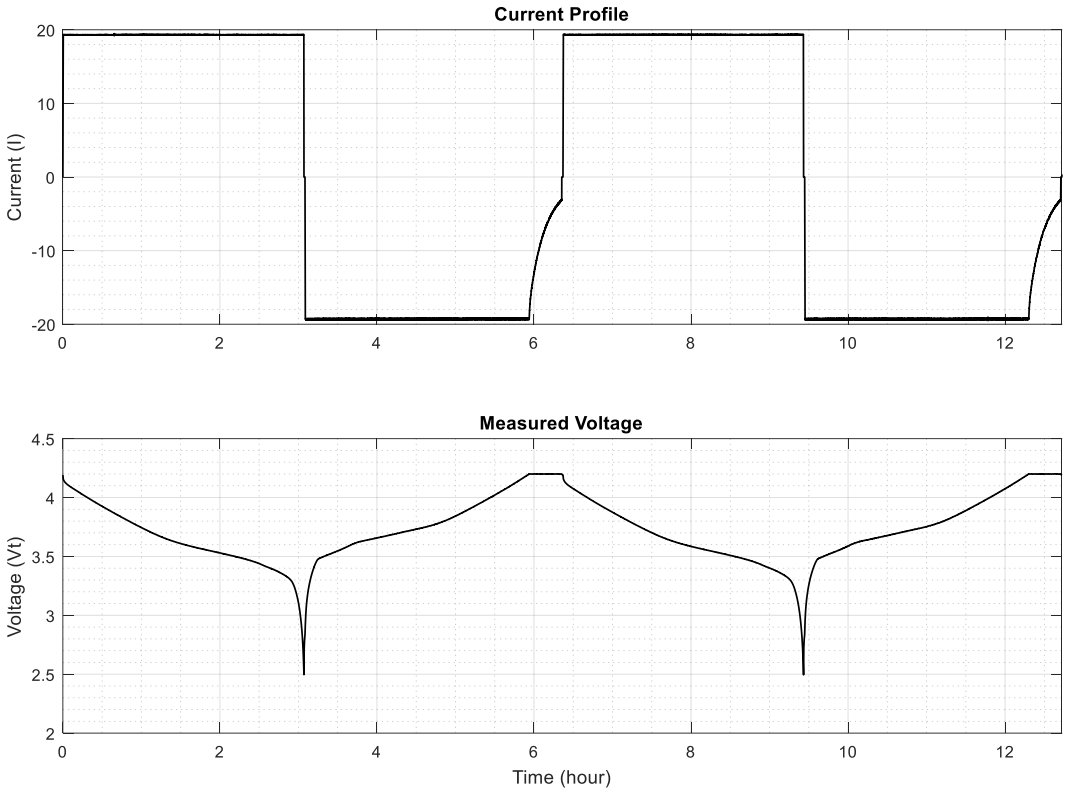

Figure 48. CC-CV cycle